Wright State University

CORE Scholar

2011

Fusion of Video and Multi-Waveform FMCW Radar for Traffic Surveillance

Nicholas C. Gale
Wright State University

Follow this and additional works at: https://corescholar.libraries.wright.edu/etd_all

Part of the Engineering Commons

Repository Citation

Gale, Nicholas C., "Fusion of Video and Multi-Waveform FMCW Radar for Traffic Surveillance" (2011).
Browse all Theses and Dissertations. 486.
https://corescholar.libraries.wright.edu/etd_all/486

FUSION OF VIDEO AND MULTI-WAVEFORM FMCW RADAR FOR TRAFFIC
SURVEILLANCE

A dissertation submitted in partial fulfillment

of the requirements for the degree of

Doctor of Philosophy

by

NICHOLAS C. GALE

B.S., Wright State University, 2007

M.S., Wright State University, 2008

Engineering Ph.D. Program

Wright State University

2011

WRIGHT STATE UNIVERSITY
SCHOOL OF GRADUATE STUDIES

September 9, 2011

I HEREBY RECOMMEND THAT THE DISSERTATION PREPARED UNDER MY SU-
PERVISION BY Nicholas C. Gale ENTITLED Fusion of Video and Multi-Waveform
FMCW Radar for Traffic Surveillance BE ACCEPTED IN PARTIAL FULFILLMENT
OF THE REQUIREMENTS FOR THE DEGREE OF Doctor of Philosophy.

_____
Lang Hong, Ph.D.
Dissertation Director

_____
Ramana Grandhi, Ph.D.
Director, Ph.D. in Engineering Program

_____
Andrew Hsu, Ph.D.
Dean, Graduate School

Committee on Final Examination

_____
Lang Hong, Ph.D.

_____
Kefu Xue, Ph.D.

_____
Zhiqiang (John) Wu, Ph.D.

_____
Arthur Goshtasby, Ph.D.

_____
Michael Temple, Ph.D.

ABSTRACT

Gale, Nicholas. Ph.D., Engineering Ph.D. Program, Wright State University, 2011. *Fusion of Video and Multi-Waveform FMCW Radar for Traffic Surveillance.*

Modern frequency modulated continuous wave (FMCW) radar technology provides the ability to modify the system transmission frequency as a function of time, which in turn provides the ability to generate multiple output waveforms from a single radar unit. Current low-power multi-waveform FMCW radar techniques lack the ability to reliably associate measurements from the various waveform sections in the presence of multiple targets and multiple false detections within the field-of-view. Two approaches are developed here to address this problem.

The first approach takes advantage of the relationships between the waveform segments to generate a weighting function for candidate combinations of measurements from the waveform sections. This weighting function is then used to choose the best candidate combinations to form polar-coordinate measurements. Simulations show that this approach provides a ten to twenty percent increase in the probability of correct association over the current approach while reducing the number of false alarms in generated in the process, but still fails to form a measurement if a detection form a waveform section is missing.

The second approach models the multi-waveform FMCW radar as a set of independent sensors and uses distributed data fusion to fuse estimates from those individual sensors within a tracking structure. Tracking in this approach is performed directly with the raw frequency and angle measurements from the waveform segments. This removes the need for data association between the measurements from the individual waveform segments.

A distributed data fusion model is used again to modify the radar tracking systems to include a video sensor to provide additional angular and identification information into the system. The combination of the radar and vision sensors, as an end result, provides an enhanced roadside tracking system.

Contents

List of Figures

List of Tables

ACKNOWLEDGEMENTS

I would like to first thank my advisor Prof. Lang Hong, for without his support throughout these years from an undergrad through grad school, this dissertation would not have been possible. Next, my colleagues Arunesh Roy, Wu Yang, Andrew Kondrath, and Mark Arlinghaus for their support throughout this process and whose advice and input has been greatly appreciated.

Next I would like to acknowledge the staff in the electrical engineering office for their help and guidance over these years and Alysoun Taylor-Hall for her help navigating through the doctoral program.

A special thanks to my family and friends for being there when I needed them and to provide the much needed breaks along the way. I would not have made it this far without them.

Last I would like extend my deepest gratitude to my parents, Christopher and Kathleen, who have helped shape the person I have become and my wife, Stephanie, for her unwaivering support and encouragement through all of this. Their love and support kept me going.

Chapter 1

Preliminaries

1.1 Introduction

The ability to identify and track targets of interest in an environment is an important task and has many military and civilian applications. From surveillance and security to traffic monitoring and control, the ability to detect these objects of interest and monitor their state can provide valuable information to a user. To provide that information, sensors are generally deployed to take measurements in the region of interest. In many cases these sensors provide very specialized measurements, which means that a single type of sensor might not be able to provide all the needed information about the targets of interest or the scene. In these cases where a single sensor cannot provide all the desired information, multiple sensors with varying modalities can be deployed in tandem and their measurements fused to enrich the overall information.

Electro-optical imaging sensors, like standard video cameras, are able to provide a great deal of information about the spatial separation of objects within the field of view of the sensor through the projection of the three dimensional world onto the two dimensional image plane. With the improvements in production processes and the ability to create smaller and smaller sensor arrays, the accuracy and reliability of these imaging systems

has improved drastically in the recent years. Unfortunately, due to the projective geometry of these systems, they can only provide angular information without the use of multiple cameras (stereo-vision, multiple view geometry), moving cameras, or assumptions about the objects in the scene.

Frequency modulated continuous wave (FMCW) radar, with an adequate frequency modulation scheme, can provide highly accurate range and range rate measurements of electromagnetic (EM) reflectors within the beam width of the radar. These radar utilize a continuous wave of EM energy which means that they require less power to operate over traditional pulsed systems, and because of the signal mixing at the receiver of the system the signals are in the intermittent frequency (IF) band, which is easier to handle with current low-cost digital signals processing technologies. With current manufacturing capabilities, the characteristics mentioned above, and the use of patch array based antennae, the ability to create small energy efficient systems has become a reality. However, one problem with this type of radar is the coupled range and range-rate relationship in linear frequency modulated regions of the radar. Another problem is reduced angle accuracy in the case of phase-difference based angle-of-arrival measurements.

Target detection and tracking for both radar and vision systems are both highly published areas in the signals community, but little effort has been documented about combining the benefits of both systems into a single system. This dissertation discusses the implementation of a target tracking system that uses the rich spatial information from a video sensor and the range, range-rate, and angle information from the FMCW radar system to provide enhanced target state estimation.

1.2   Problem Formation

In general, posted speed limits provide a limit to which safe travel can be performed on most roadways. With the number of vehicles on the road increasing annually, it becomes

increasingly more difficult for law enforcement officials to monitor and enforce said speed limits effectively. Due to this limitation, systems are emerging that attempt to automate these processes. If these automated systems are implemented correctly they can provide valuable traffic information in target areas and might possibly be used to reduce serious incidents on the road.

The goals of this system are to be able to estimate the position and velocity of vehicles on the road and to associate those estimates with video for visual identification, validation, and improved state estimation. The multiple waveform FMCW radar provides polar or pseudo polar measurements for multiple targets in the scene. The video camera, on the other hand, provides additional angular information for targets within the scene for association.

In order to provide these state estimates for the vehicles on the road a few assumptions are made about the scenario.

System Tracking Scenario Assumptions:

- Vehicles travel at approximately a constant velocity within the tracking period.

- Vehicle velocity is bound by physical and structural limitations.

- Vehicles motion is smooth within the tracking period.

- Vehicles are constrained to a road plane.

- Vehicles are modeled as point targets in the FMCW radar.

- Road is straight and flat within the region-of-interest.

- In one waveform period, measurements from each waveform segment measure the same state.

- Vehicles remain visible during tracking period.

Since the desired tracking window is fairly short, generally less than a ten second period and within two hundred meters, these assumptions are reasonable. Over that short range many rural and urban highways are relatively straight and flat and vehicles are generally traveling at constant speeds. The obvious exceptions to this are traffic jams, accidents, rapid breaking, and lane merging. For major highways inter-vehicle occlusion can be a major issue, but there will be many instances where this is not a problem. For the purposes of this document, these scenarios are ignored and can be addressed in future research. A diagram of the proposed framework can be seen in Figure 1.1.
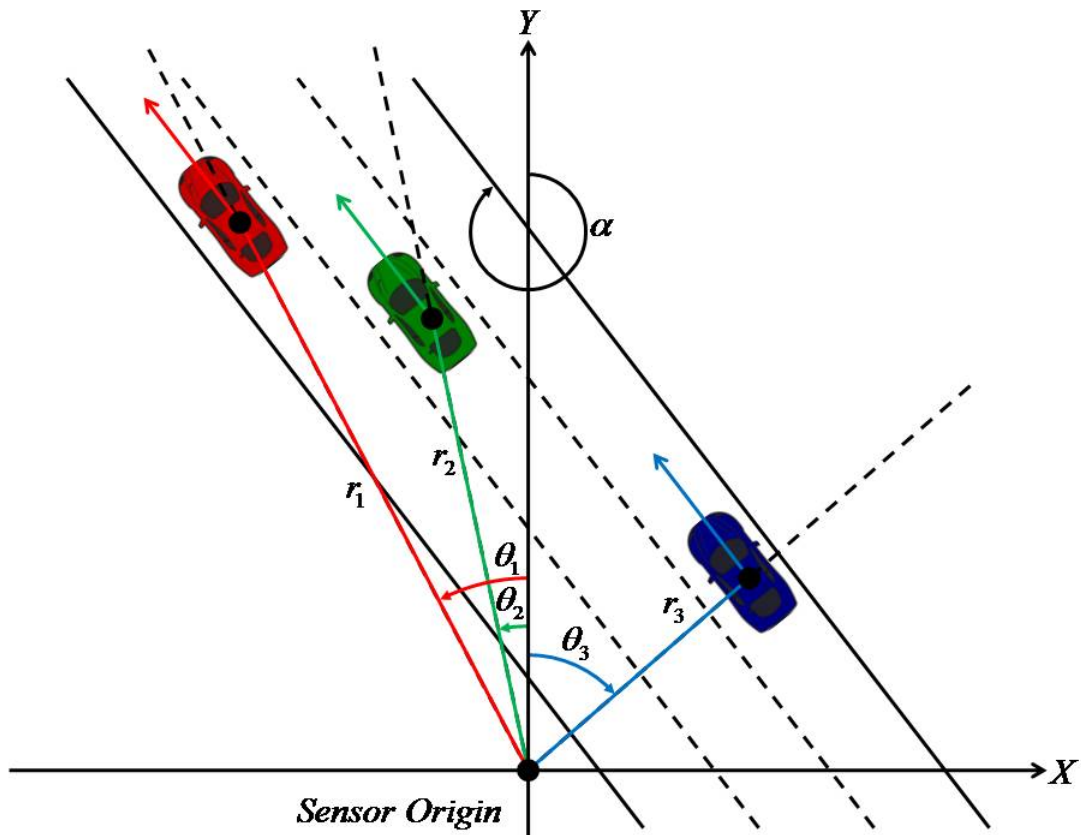
Figure 1.1: Proposed tracking scenario.

In this scenario there are multiple lanes of traffic traveling in a similar direction. Vehicles are moving on the the x-y plane with constant velocity away from the sensor. The camera and the radar are assumed to both be aligned with the y-axis with the angle between the y-axis and the road edge (α) being fairly small ($[-20°, 20°]$) which will provide a long

4

enough tracking period.

1.3   Research Methodology

The overall top level research approach is graphically depicted in Figure 1.2 which depicts
the system development.
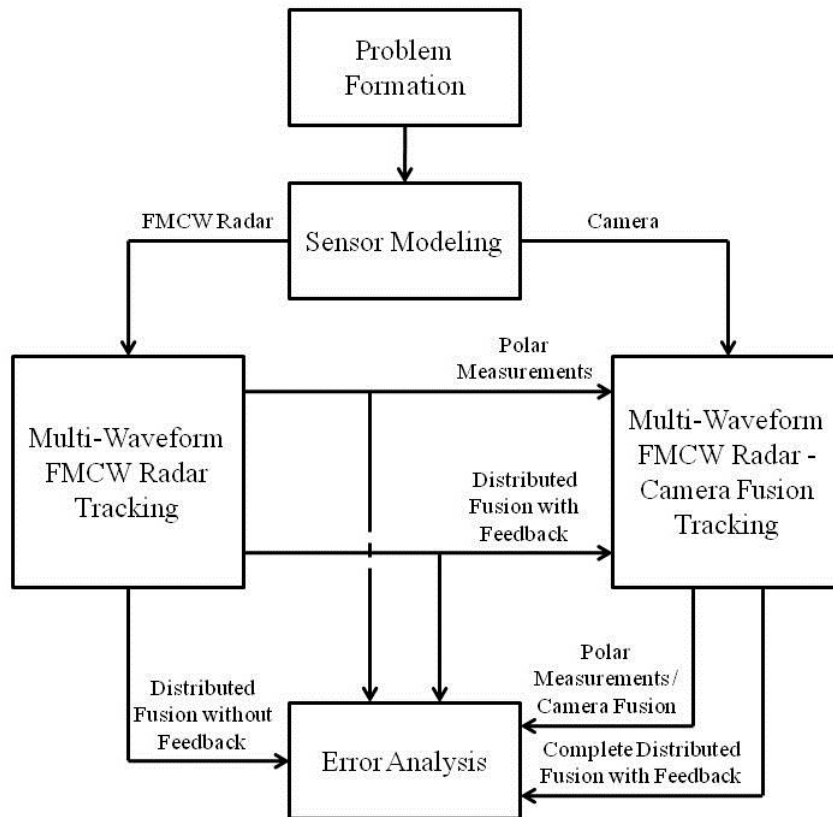
Figure 1.2: Research methodology.

   With the tracking problem defined, sensors were chosen which could provide an ef-
fective means of providing information of the scene. Radar sensors have a long tradition
in vehicle systems in the form of safety features, because they have proven to be a reli-
able means of generating measurements in many adverse scenarios. Cameras, on the other
hand, provide a great means to identify and classify objects and provide angular informa-
tion. Combined these sensors can provide a vast amount of information about the scene.

Measuring moving objects within the field-of-view of a simple linear FMCW radar traditionally suffer from problem that measurements are a coupled measure of range and range-rate. This issue can be resolved over time with some moving object constraints and a tracking filter, but the convergence time is longer than desired in most roadside tracking systems. To compensate for this problem, multiple waveform types can be used in succession to provide more information on the moving objects. The problem using multiple waveform types becomes one of data association between the waveforms. One approach is to choose sets of detections from each waveform which can be used to to generate polar coordinate measurements. The other approach would be to treat the individual waveforms as separate sensors and fuse the results to form a better estimate than what would have been generated from one waveform alone. This process can be performed through distributed fusion with and without feedback.

Since vision sensors provide additional information on the angle of the of objects and fast algorithms are already available for moving object detection and tracking, they can easily be integrated into the fusion framework. To do so distributed fusion can one again be applied to fuse measurements from the camera and the radar framework.

Simulations provide a means of testing the systems against pure ground truth which can provide best case error analysis, as well as, system consistency. These simulations can also provide a means of testing systems against worst case scenarios to help identify possible faults in the system. Real data can also be used to test the system performance, but ground truth data (at least for roadside systems) is generally hard to obtain for most ground truth data must be collected using additional sensors which may or may not have accuracy better than the actual system accuracy.

1.4 Overview

This chapter covers a brief background on the the reasoning behind the sensor fusion approach as well as the breakdown of the document as a whole. The proposed system is defined and the reasoning for the research interest is explored. Finally, the research approach is defined with the structure of the contributions.

Chapter two contains a historical perspective on the traffic monitoring and surveillance problem and the background information on the sensors and state estimation used in the tracking system. The radar signal model used within the defined system is explored along with the common signal processing algorithms used to generate measurements from this data. In addition to developing the radar model, the multiple waveform pulse design used in the system is defined. A model for the camera side of the system is also defined and the methods for generating measurements are also covered briefly. State estimation and data association principles used throughout the document are then covered.

Chapter three covers the methods developed for the system to handle the issues that arise when multiple measurements are generated in each section of the multiple waveform FMCW model. A method for combining the information from the individual waveform sections using a weighting function is first covered. Then a framework for treating the individual waveform sections as isolated sensors is developed. This multiple sensor approach is then coupled with distributed data fusion approaches to generate state estimates. The distributed data fusion approaches are developed with or without feedback.

Chapter four covers the methods for combining the information from the radar tracker with the information from the video system. In this chapter, two specific methods are proposed which utilize a distributed data fusion approach. The first method augments the traditional range, range-rate, and angle radar tracker by adding a the camera as a second sensor which only provides angular information. The second fusion scheme covered is the augmented distributed data fusion with feedback radar tracker which includes adding the camera measurements into a forth sensor input channel into the state fusion scheme.

Chapter five provides some experimental validation for the measurement grouping algorithm that is discussed in chapter three. This chapter also discusses the use of the polar measurements derived by that algorithm for road modeling and system validation.

Chapter six looks at the results from the system. Simulated data is used to determine the theoretical system performance for the tracking systems with and without the video information through the use of Monte Carlo simulations. Speed, position, and angle errors are measured using a real data set in order to further validate the system architectures.

Chapter seven provides the conclusions from the research. Reflections on the system are provided along with the contributions provided by this document.

Chapter 2

Background

In this section of the document, the historical approaches for traffic surveillance are covered with specific attention to radar and vision based systems. The sensors used to tackle this problem as well as the essential algorithms used to obtain useful information from those sensors is also covered in this section.

2.1 Historical Perspective

Tracking ground targets is not a new topic in the tracking field. A nice overview of the historical methods for tracking ground targets can be seen in [1]. Although this paper discusses many of the algorithms for ground target tracking, it does not cover the sensor measurement generation nor does it cover many of data association problems that can occur when forming measurements into these tracking systems.

Traditional methods which focus on roadside speed detection are discussed in [2]. These methods include down and across the road Doppler radar systems which tend to only isolate the strongest or fastest targets. Although the speed estimates are accurate, multiple targets cannot be identified because there is no positioning information to help differentiate those multiple vehicles. Line of sight lasers were also discussed which can accurately pinpoint a single vehicle, but require manual aiming which is not beneficial for

automated traffic systems.

Currently more advanced radar systems have been developed to tackle the problem of only being able to detect a single target. Many of the sensors used in these systems are capable of directly measuring range, range-rate, and angle through the use of a pulsed Doppler unit. The general framework for tracking with these polar coordinate measurements with specific application to vehicle detection can be seen in [3, 4]. These papers cover some of the implementation issues one might encounter when using such measurements when tracking vehicles. In [5, 6] some methods are developed which deal with data association issues that arise in the polar coordinate measurements for multiple vehicle tracking. These papers cover the data association issues once a set of polar coordinate measurements is available, but do not provide any means of generating those measurements if the radar system is unable to provide those measurements directly.

Another body of research has been dedicated to video only based traffic monitoring and classification. In [7] general vision based techniques are discussed which cover video based traffic monitoring and on board vehicle guidance. An overview of similar video based techniques applied for urban traffic scenarios is covered in [8]. These systems, however, are directed for very specific applications not tailored for high accuracy roadside tracking. Many of these systems discussed also require a more bird's eye view of the scene, which is not always achievable for an easily deployable traffic system.

To move away from the limitation of single targets and improve system accuracy, systems were developed to combine the positioning benefits of an FMCW radar and a video sensor. The combination of radar and vision systems is not unique. Applications such as automatic cruise control (ACC), automated lane change (ALC), and obstacle avoidance have been explored in [9, 10, 11, 12]. Many of these systems have a limit on the number or possible detections and focus on vehicle-to-vehicle detections. These papers also use radar sensors that are able to directly measure range, angle, and speed for each detection using either advanced signal processing techniques or advanced hardware. In [13, 14] a method

was developed to combine Doppler radar and video signals for accurate multiple vehicle tracking, but required birds-eye view which might not be achievable in all environments. A second camera was added in [15] in order to better associate the radar and camera measurements with point contour matching through stereo vision. Although the performance was improved in data association the system required calibration between the two cameras and focused on the information of single threat vehicle for collision detection.

2.2   FMCW Radar Model

Frequency modulated continuous wave (FMCW) radar is not a new topic and there are several great sources on FMCW radar [16, 17] as well as some great sources of information for general radar system design [18, 19, 20]. An overview of the complete single transmitter/dual quadrature receiver FMCW radar model can be seen in Figure 2.1. The radar used in the system has a voltage controlled oscillator (VCO) with a single transmitter with two quadrature mixing receivers.

Frequency modulated continuous wave radar illuminate a region-of-interest with electromagnetic energy which has a frequency that is time dependent (2.1) from the transmitting antenna.

$$s_T(t) = cos\left(2\pi f_T(t)t\right) \tag{2.1}$$

This energy reflects off of objects within the region-of-interest and returns to the receiver. If the objects are stationary, the returned signal (2.2) is just a scaled (ρ) and time delayed (2.3) version of the transmitted signal.

$$s_R(t) = \rho s_T(t - \tau) = \rho cos\left(2\pi\left[f_T(t - \tau)t - f_T(t - \tau)\tau\right]\right) \tag{2.2}$$
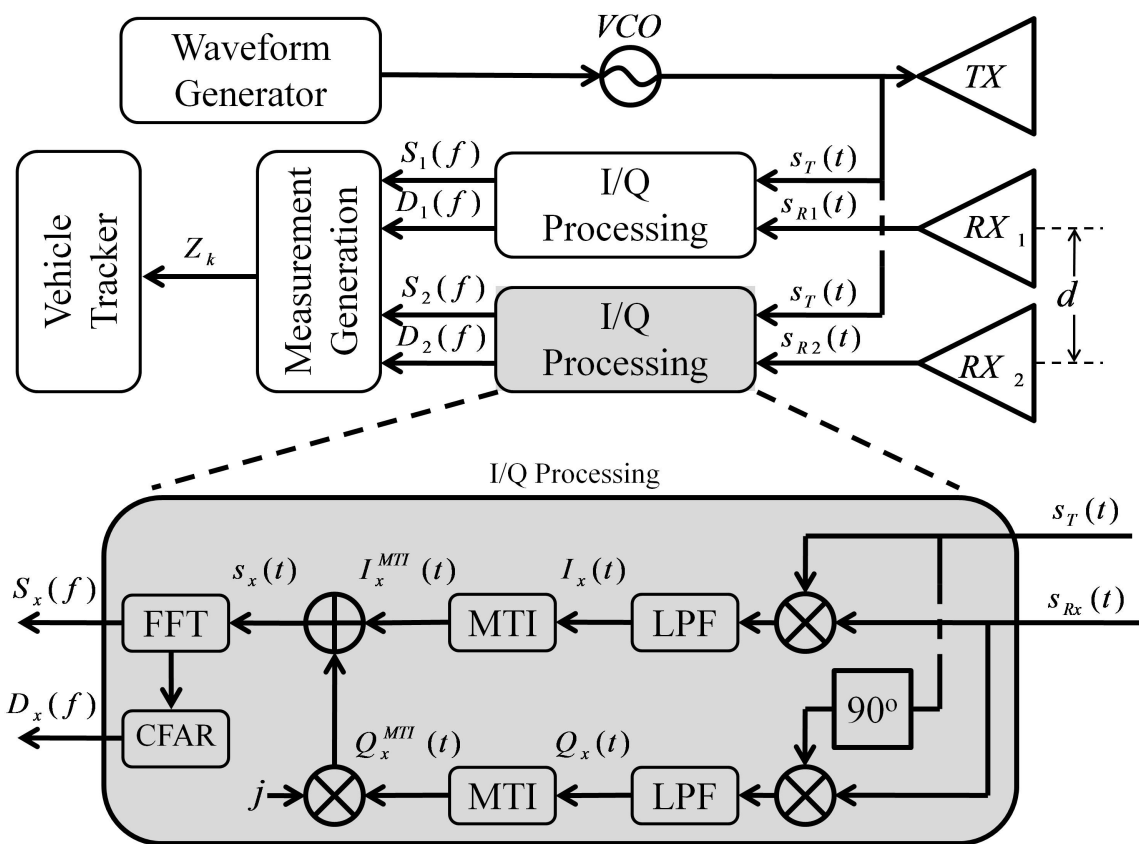
Figure 2.1: Radar signal flow model.

$$\tau = \frac{2r_k}{c_o} \tag{2.3}$$

where r_k is the range to that object and c_o is the speed of light in a vacuum. If, on the other hand, an object is moving, the returned signal (2.4) is not only scaled and time delayed, it is also frequency shifted by the Doppler effect (2.5).

$$s_R(t) = \rho cos\left(2\pi\left[(f_T(t-\tau) + f^{Dopp})t - (f_T(t-\tau) + f^{Dopp})\tau\right]\right) \tag{2.4}$$

$$f^{Dopp} = -\frac{2f_c}{c_o}\dot{r}_k \tag{2.5}$$

where $\dot{r}_k$ is the projection of the object velocity onto the range and f_c is the carrier frequency of the waveform. These received signals are then mixed with the transmitted signal using a quadrature mixer and then low pass filtered to remove the high frequency component of the mixing process. The frequencies of these outputs are dependent on the frequency modulation scheme chosen. For the purposes of this document, three classes of of frequency modulation are employed in the construction of an output waveform. A diagram of this waveform can be seen in Figure 2.2.

These three waveform sections can be classified as follows: a pure Doppler region capable of providing higher accuracy range-rate information along with angle, a region with linearly increasing frequency modulation which provides a coupled measure of range and range-rate along with angle, and finally, a region with linearly decreasing frequency modulation which provides an additional coupled measure of range and range-rate along with angle. As the above figure shows, there are regions in the IF received waveform that does not contain useful information dubbed 'BAD' in the figure. In many short range applications, the timing parameters can be chosen in such a way that these 'BAD' regions can fall within a single sample and has little effect on the overall frequency information in each section.
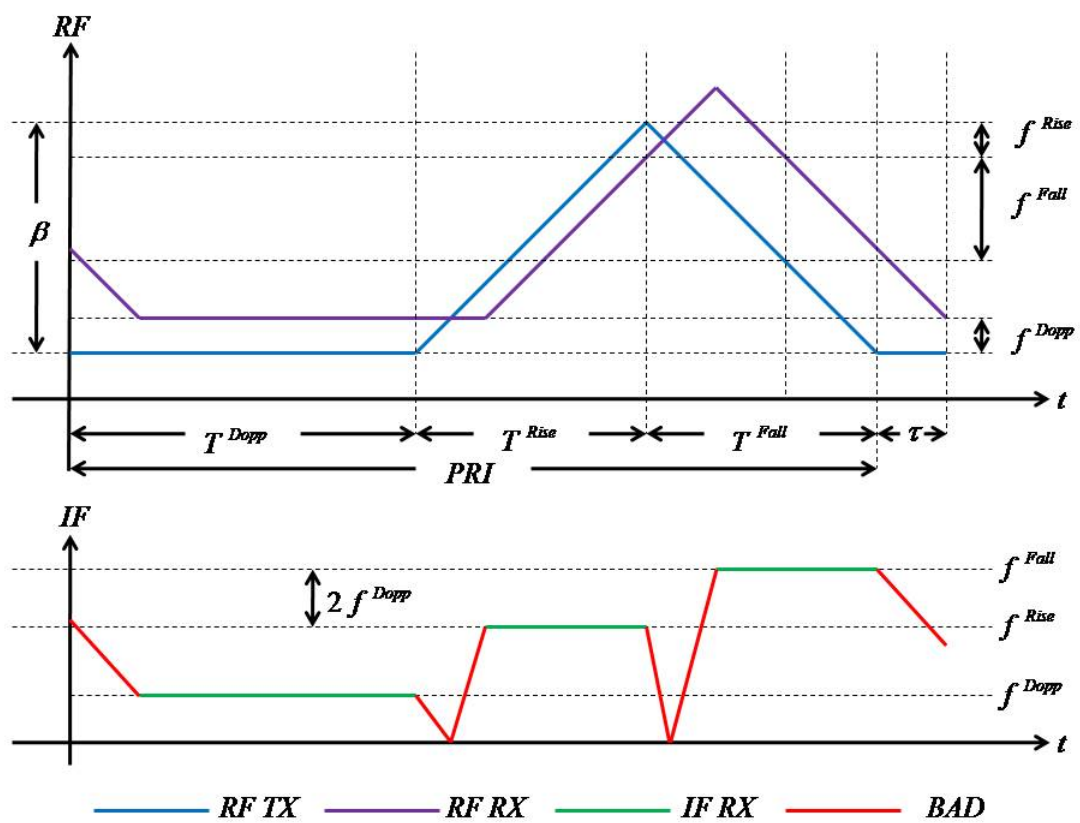
Figure 2.2: Frequency diagrams for transmitted and received waveforms.

Ideally, there will only be single return from each target with significant radar cross section which means that the returned signals within each section can be approximated by a sum of cosine functions for each waveform section. This can be seen in equations (2.6 - 2.8).

$$s^{Dopp}(t) \approx \sum_{i=1}^{N} \eta_i cos(2\pi f_{k,i}^{Dopp} t) \tag{2.6}$$

$$f_{k,i}^{Dopp} = -\frac{2f_c}{c_o}\dot{r}_{k,i}$$

$$s^{Rise}(t) \approx \sum_{i=1}^{N} \eta_i cos(2\pi f_{k,i}^{Rise} t) \tag{2.7}$$

$$f_{k,i}^{Rise} = \frac{2\beta}{c_o T_{Rise}} r_{k,i} - \frac{2f_c}{c_o}\dot{r}_{k,i}$$

$$s^{Fall}(t) \approx \sum_{i=1}^{N} \eta_i cos(2\pi f_{k,i}^{Fall} t) \tag{2.8}$$

$$f_{k,i}^{Fall} = \frac{2\beta}{c_o T_{Fall}} r_{k,i} + \frac{2f_c}{c_o}\dot{r}_{k,i}$$

where i is the ith object out of N and $\dot{r}_{k,i}$ and $r_{k,i}$ are the range and range-rate to target i at time scan k. The Doppler region of the signal only provides information on moving objects within the scene, but the linear frequency modulation segments provide frequencies for both moving and stationary objects. Since the purpose of the system is to track moving vehicles and due to system noise, these returned signals from each section of the waveform must be processed in order to generate measurements.

2.3 FMCW Radar Measurement Generation

Due to the nature of the returned signals, there are two steps that must be performed in order to form measurements from the from the data. The first step is to reduce the influ-

ence of stationary targets through filtering, while the second step is to automatically detect frequencies of interest from the filtered signal. These processes can be achieved through moving target indication (MTI) and constant false alarm rate (CFAR) detection.

2.3.1 Moving Target Indication

In order to separate the moving targets from the stationary objects in the background, moving target indication methods are employed. Two easily implemented methods for performing this are single and double delay line cancelers which are described in [21]. In both methods the cancelers attempt to model the stationary behavior of the signal from pulse to pulse and remove that stationary signal from the current time period. For the single delay line canceler, it is assumed that from pulsing period to period, the returns from stationary objects will be constant, which means that the signal from the last time period can be subtracted from the current time period and the resulting signal will contain only the moving targets. This process can be seen in equation (2.9).

$$s^{MTI}(t) = s(t) - s(t - PRI) \tag{2.9}$$

In the case of the double delay line canceler, a second order model is used to model the stationary target returns (2.10). Stationary behavior is modeled using the last two time periods and the current time period.

$$s^{MTI}(t) = s(t - 2PRI) - 2s(t - PRI) + s(t) \tag{2.10}$$

These techniques cannot be applied to the defined multi-waveform FMCW radar due to the fact that the Doppler region is already providing information on the moving objects within the scene. In many cases, applying the cancelers to the Doppler region of the signal would remove the signal energy from signals that are actually useful to the tracking system. To apply these techniques to the multi-waveform FMCW system a mask is applied to the

data so that only the region with the up-chirp and down-chirp are being subtracted from the current time signal.

An example of the moving target indication can be seen in Figure 2.3. In this figure, the Fourier transform is taken for the up-chirp region of the waveform at each time period generating a short time Fourier spectrogram [22] for an approaching vehicle before and after the single delay line canceler was applied.

What this figure shows is that the MTI approach for linear FMCW radar is an effective means of removing the energy from the stationary objects in the scene without noticeably effecting the energy from the moving target within the scene. For this specific application, a single delay line canceler was sufficient to reduce the response from the stationary objects which are not of interest to the system. Once the influence of stationary objects is reduced in the linear FMCW regions of the signal, an automatic detection strategy must can be applied.

2.3.2 Constant False Alarm Rate Detection

Once the effects from stationary targets are reduced, measurements must be generated from the moving target data. Since the important information about the targets is located in the frequency domain, the Fourier transform is applied to each section of the overall waveform for each time period. For the case defined here using three waveform sections, this process provides three separate complex Fourier transforms for each period k (2.11-2.13).

$$S_k^{Dopp}(f) = \mathcal{F}\left\{s_k^{Dopp}(t)\right\} \tag{2.11}$$

$$S_k^{Rise}(f) = \mathcal{F}\left\{s_k^{Rise}(t)\right\} \tag{2.12}$$

$$S_k^{Fall}(f) = \mathcal{F}\left\{s_k^{Fall}(t)\right\} \tag{2.13}$$
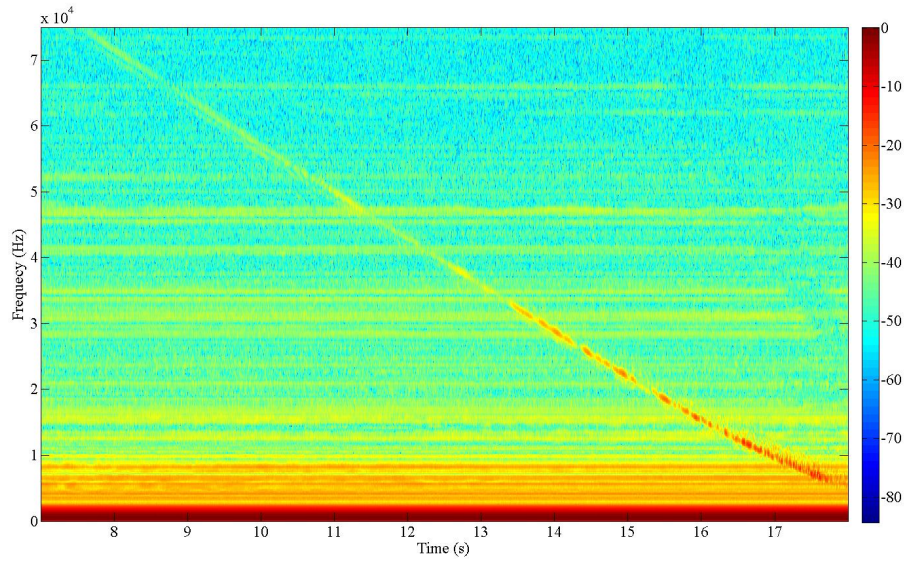
(a) Spectrogram Before MTI (dB)
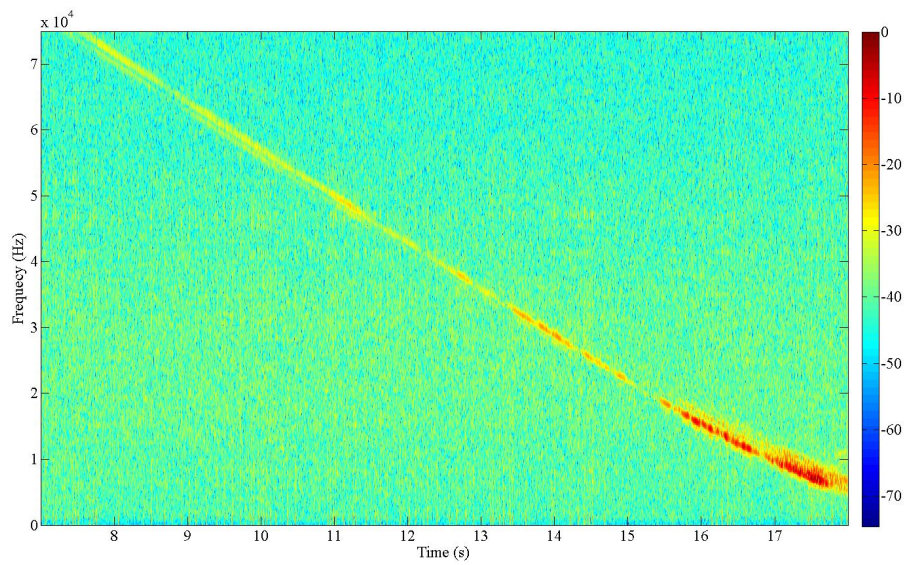
(b) Spectrogram After MTI (dB)

Figure 2.3: Example of moving target indication processing.

With the signal now in the frequency domain, frequencies of interest must be detected and separated from the noise. To do so signals with significant power with respect to some criteria must be detected. This process can be most conveniently done through the analysis of the spectral power (2.14).

$$D_i = |S_k^x(f_i)|^2 \qquad (2.14)$$

where D_i is the power of the signal of waveform x with respect to discrete frequency f_i. The simplest method for detection would be to apply a fixed threshold to the magnitude spectrum and use values above that threshold as detections, but due to complex radar cross section models for vehicles and other moving targets the signal power can fluctuate from scan to scan rendering a fixed threshold obsolete. To help improve detection performance over a fixed threshold, constant false alarm rate (CFAR) detection can be applied. There are three standard types of CFAR detectors which can be easily implemented to improve detection reliability. These methods are cell averaging (CACFAR), greatest-of (GOCFAR), and smallest-of (SOCFAR) which all try to statistically model the noise around a given frequency bin i.

In the case of CACFAR as seen in Figure 2.4a the average signal power is measured from the n bins to either side of the frequency bin in question. This mean is then used as part of the detection criteria which can be seen in (2.15).

$$D_i = \begin{cases} Detection & if D_i > C(P_{FA}, K)E(D|n) \\ NoDetection & Otherwise \end{cases} \qquad (2.15)$$

where $C(P_{FA}, K)$ is a detection statistic based on the probability of false alarms (P_{FA}) the number of cells being used to form the mean ($K = 2n$) and the noise model for the data. This detection statistic can be found in [23] which also provides an additional reference to these types of statistical detectors.

The GOCFAR and SOCFAR detection strategies are similar to that of the CACFAR

algorithm, with one major difference. These approaches look at the mean of the power of the bins on either side of the frequency bin in question and determine a threshold based on either the greatest of the two means (in the case of GOCFAR) or the smallest of the two means (in the case of SOCFAR). The outline of these algorithms can be seen in 2.4b. The GOCFAR and SOCFAR algorithms attempt to improve the detection performance in cases where noise might be higher to one side of a bin in question over another.
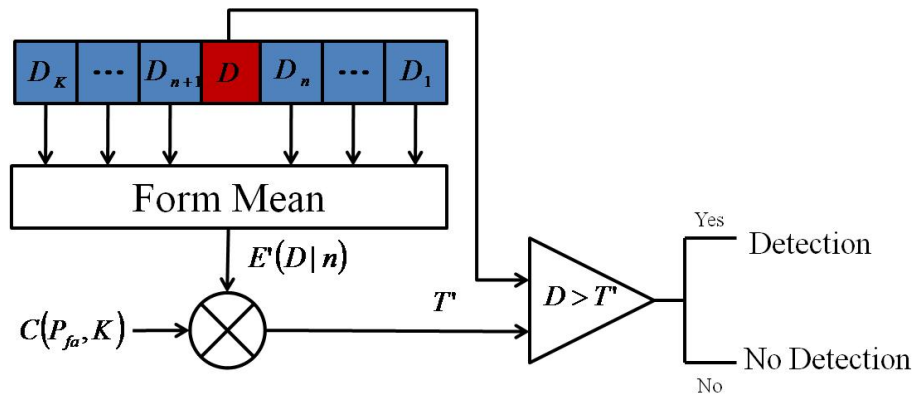
(a) CACFAR
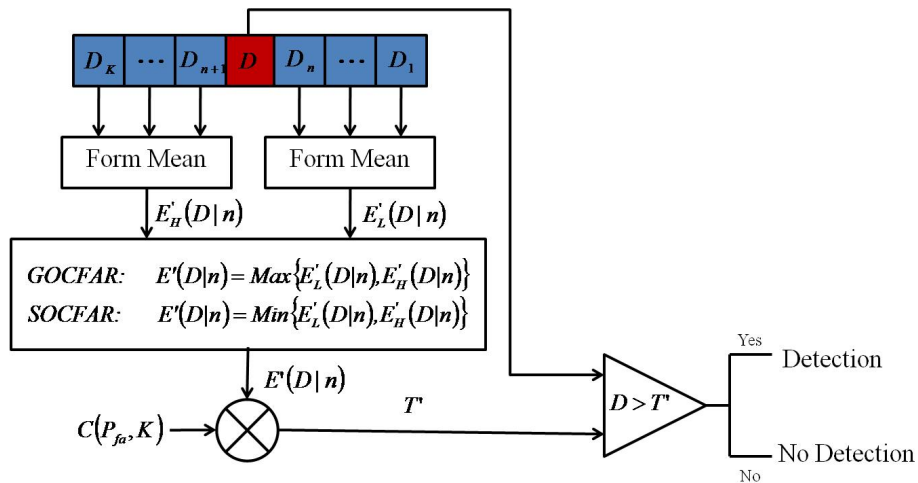
(b) GOCFAR/SOCFAR

Figure 2.4: CFAR detection strategies.

An example of the performance of these three methods with respect to an approaching target and using a linearly increasing frequency modulation can be seen in Figure 2.5.

In Figure 2.5a the power spectra for an approaching target from the up-chirp region after MTI processing with respect to time can be seen. The detections from the CACFAR,
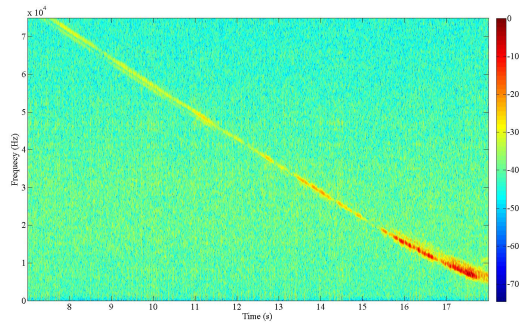
(a) Target Spectrogram (dB)
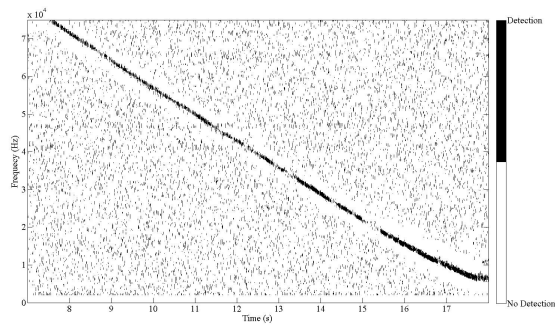
(b) CACFAR Detections
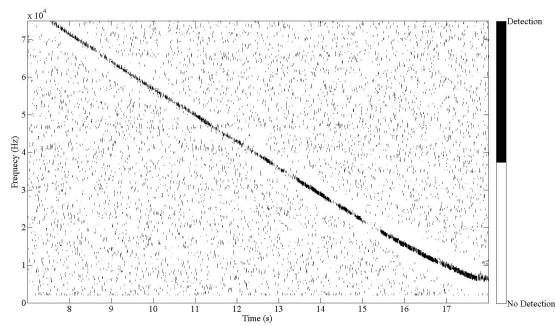
(c) GOCFAR Detections
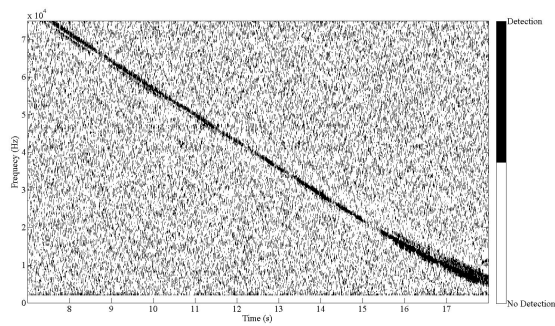
(d) SOCFAR Detections

Figure 2.5: CFAR detection comparison.

GOCFAR, and SOCFAR can be seen in Figures 2.5b-2.5d respectively. These figures show that the SOCFAR algorithm has the most total detections, as well as, the most false alarms of the three methods. The GOCFAR and CACFAR algorithms had a similar number of detections with the SOCFAR showing only a slight improvement.

At a given period k all of the actual frequencies that correspond to the detections are considered as frequency measurements for that period. These same detection approaches can be applied to each of the waveform sections independently to form the frequency measurement sets for that period

2.3.3 Angle Measurements

Due to the dual receiver design of the radar being used, the device is also able to generate angle of arrival information about the targets within the scene. Because the targets are far enough away from the sensor, it can be assumed that the returning wavefront can be approximated by a plane. A diagram of the returning wavefront can be seen in Figure 2.6.
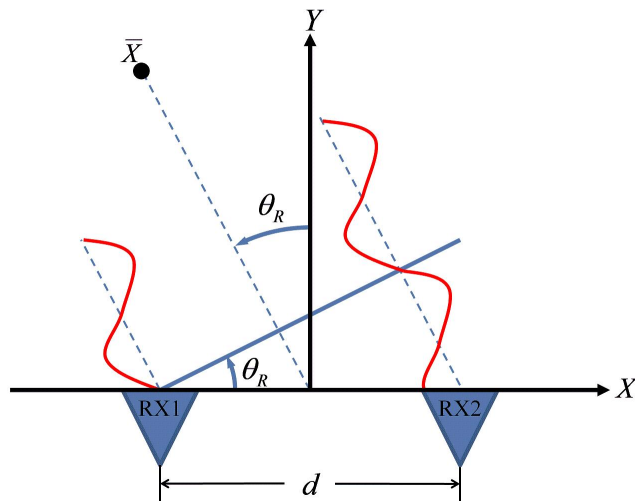
Figure 2.6: Plane wave approximation for angle of arrival determination.

Since the carrier frequency (f_c) is known for the system, the phase difference between the returns becomes a function of the carrier frequency wavelength (λ) and the distance

22

between the antennae (d) which can be measured directly (2.16).

$$sin(\theta_R) = \frac{\Delta\phi\lambda}{2\pi d} \tag{2.16}$$

Because the phase characteristics carry through to the IF signals, the phase difference between the received signals from the two antennae at a given frequency f_i can be used to determine an angle of arrival ($\theta_R(f_i)$) at that frequency (2.17).

$$\theta_R(f_i) = asin\left\{\frac{(\angle S^x_{k,1}(f_i) - \angle S^x_{k,2}(f_i))\lambda}{2\pi d}\right\} \tag{2.17}$$

Now using the above formulation, at every instance where there is a detection from the CFAR algorithm a joint frequency and angle measurement can be generated. These joint measurements are those that will later be used by the tracking frameworks.

2.4 Camera Model

Cameras have the ability to provide higher accuracy angular information through the projection of the three dimensional world onto a two dimensional plane. For the sake of completeness, a good collection of resources for the camera modeling can be found in [24] [25] [26]. Figure 2.7 portrays the geometry of a three dimensional point being mapped onto the image plane using the frontal pinhole model.

Points in the three-dimensional world coordinate system are projected onto the image plane using a projective transform (2.18).

$$\overline{x} = P\overline{X} \tag{2.18}$$

$$\overline{x} = \begin{bmatrix} x_i & y_i & 1 \end{bmatrix}^T$$
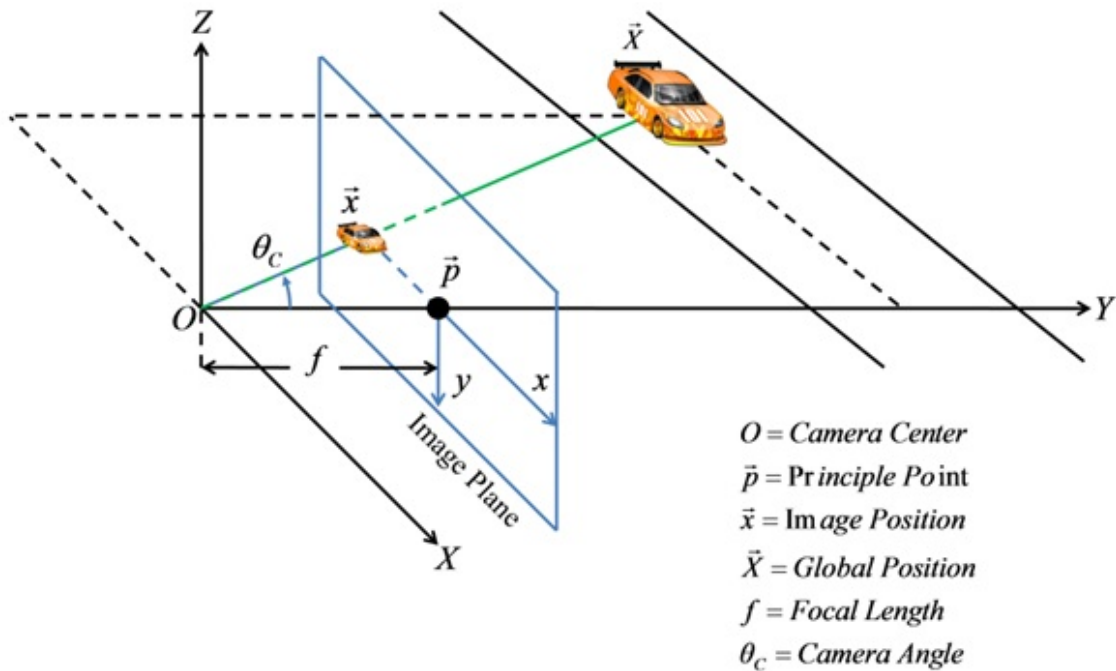
Figure 2.7: Frontal pinhole camera model.

$$\overline{X} = \begin{bmatrix} X_w & Y_w & Z_w & 1 \end{bmatrix}^T$$

This projective transform matrix (2.19) can be decomposed into a world coordinate to local coordinate transform consisting of a rotation matrix (R), a translation matrix (t) and a camera intrinsic matrix (K).

$$P = K\,[R|t] \tag{2.19}$$

The intrinsic matrix (2.20) can be found through calibration prior to processing using a method defined in [27]. An implementation of the camera calibration algorithm is freely available in an open source software package [28].

$$K = \begin{bmatrix} f_x & s & p_x \\ 0 & f_y & p_y \\ 0 & 0 & 1 \end{bmatrix} \tag{2.20}$$

Since the targets are constrained to the x-y plane and the camera and world coordinate frames are assumed to share the same origin, the translation is negligible and the rotation matrix is a simple ninety degree rotation around the x-axis (2.21).

$$[R|t] = \begin{bmatrix} 1 & 0 & 0 & 0 \\ 0 & 0 & -1 & 0 \\ 0 & 1 & 0 & 0 \end{bmatrix} \tag{2.21}$$

Additionally, the x-y plane constraint assumes the target altitude in the world coordinate frame is also negligible for a roadside system (2.22).

$$\overline{X} = \begin{bmatrix} X_w & Y_w & 0 & 1 \end{bmatrix}^T \tag{2.22}$$

This arrangement leads to a unique coordinate transform (2.23) which simplifies the mapping from the world coordinates to image plane coordinates.

$$\overline{x} = \begin{bmatrix} \frac{f_x X_w}{Y_w} + p_x \\ p_y \\ 1 \end{bmatrix} \tag{2.23}$$

Because of the above formulation, the elevation angle is ignored (for it should be zero) leaving only the azimuth angle (θ^{Cam}) which is a function of the cameras calibration information and the x-pixel coordinate of a target (2.24).

$$\theta^{Cam} = Tan^{-1}\left(\frac{X_w}{Y_w}\right) = Tan^{-1}\left(\frac{x_i - p_x}{f_x}\right) \tag{2.24}$$

Angles can be determined for every pixel on the image plane so it is important to find

the areas of interest due to the vast number of pixels on the sensor.

2.5 Camera Measurement Generation

Much like the radar sensor, it is important to separate the moving objects from the stationary background in the video sequence. This process can be achieved through the use of background modeling and foreground isolation. A survey of the various methods of moving object detection with regards to video can be seen in [29, 30, 31] while implementations of a few of these methods are provided in the OpenCV software. A general guide to the use of this software can be found in [32].

In general, these methods attempt to model the background with some a model function or distribution that which can be used to compare new images against. Some sort of weighting metric function ($f(I(\overline{x}), BG(\overline{x}))$) is used in these approaches to measure how much given pixel in a given frame ($I(\overline{x})$) deviates the model ($BG(\overline{x})$). Pixels that deviate from the model by more than a predetermined threshold are determined to be foreground pixels. These foreground pixels can then be represented by a foreground binary mask (2.25).

$$FG(\overline{x}) = \left\{ \begin{array}{ll} 1 & if f(I(\overline{x}), BG(\overline{x})) > Thresh \\ 0 & else \end{array} \right\} \tag{2.25}$$

Once a foreground mask has been generated, these foreground pixels can be grouped together using connected components analysis or proximity matching to form blobs. Assuming that the vehicles are not being occluded in some way and because vehicles are not disjoint, it can be assumed that foreground pixels that are close enough together on the image plane are from the same vehicle. Once these blobs have been formed, the centroids (μB_j) for these blobs can be determined, which in an ideal case represents the center mass of the vehicle. This process can be done by finding the mean of all the x and y locations of

the pixels in the individual blob (2.26).

$$\mu B_j = \frac{\sum_{n=1}^{N} \overline{x}_j(n)}{N} \qquad (2.26)$$

In this case μB_j is the centroid of blob B_j and $\overline{x}_j(n)$ is the nth pixel of blob B_j. These centroids can then be converted to angle measurements in a similar process as equation 2.24 where x_i is replaced with the x pixel of the blob centroid. These angle measurements from the blob centroids can now be fed into a tracking system as measurements.

A sample background model along with the foreground detections and the associated blob centroids for a multiple target scenario can be seen in Figure 2.8.

Although these blobs may change in size as targets travel through the scene, the centroid of the blob should stay within the center mass of the vehicle on the image plane. If the foreground and background modeling is functioning as desired and it meets this criteria, these are accurate measurements of the target angle.

2.6 State Estimation

In 1960 R.E. Kalman introduced in [33] a recursive optimal estimator which provided a solution to the discrete data filtering problem. As computing resources became cheaper and more powerful, this technique has been applied to many problems. One such problem has been the target state estimation problem. There are several texts which provide the foundations for the use of Kalman filtering algorithms with respect to target tracking specifically [34, 35, 36, 37, 38]. General algorithms for implementing the these filters can be found in [39].

2.6.1 Linear Kalman Filtering

When a physical system can be approximated by a linear Gaussian model the traditional linear Kalman filter can be applied to provide an optimal state estimation. In this scenario

(a) Blob Centroids with Bounding Ellipses

(b) Background Model

(c) Foreground Mask

Figure 2.8: Example blob analysis.

the system (2.27) and measurement dynamics (2.28) are modeled with a linear systems.

$$x_k = F_k x_{k-1} + w_{k-1} \qquad w_{k-1} \sim \mathcal{N}(0, Q_{k-1}) \qquad (2.27)$$

$$z_k = H_k x_k + v_k \qquad v_k \sim \mathcal{N}(0, R_k) \qquad (2.28)$$

where w_{k-1} and v_k are zero mean Gaussian distributed random vectors with covariance matrices Q_{k-1} and R_k respectively. Using these stochastic models for the system the a

state can be estimated through a projection and update process. In the projection process, an estimate of the state (2.29) and state covariance (2.30) is generated based on the system model.

$$\hat{x}_{k+1|k} = F_k \hat{x}_{k|k} \tag{2.29}$$

$$P_{k+1|k} = F_k P_{k|k} F_k^T + Q_k \tag{2.30}$$

As the measurement comes in the state (2.31) and state covariance (2.32) can be generated with respect to that measurement z_k.

$$\hat{x}_{k+1|k+1} = \hat{x}_{k+1|k} + K_{k+1}(z_{k+1} - H_{k+1}\hat{x}_{k+1|k}) \tag{2.31}$$

$$P_{k+1|k+1} = P_{k+1|k} - K_{k+1}H_{k+1}P_{k+1|k} \tag{2.32}$$

$$K_{k+1} = P_{k+1|k}H_{k+1}^T S_{k+1}^{-1}$$

$$S_{k+1} = H_{k+1}P_{k+1|k}H_{k+1}^T + R_{k+1}$$

This process can be iterated until measurements stop arriving for the system. This process, however, only works when the system and measurement models are linear. Unfortunately, many of these sensors (especially radar sensors) provide measurements in polar coordinates where the systems are tracked in the Cartesian space which means that the sensors provide a non-linear mapping to the system space.

2.6.2 Extended Kalman Filtering

Cases where either the system dynamic model or the measurement model are non-linear a sub-optimal extended Kalman filter can be applied if the process noise and measurement noise is still considered Gaussian. This modifies the system (2.33) and measurement (2.34) models.

$$x_k = f(x_{k-1}) + w_{k-1} \qquad w_{k-1} \sim \mathcal{N}(0, Q_{k-1}) \tag{2.33}$$

$$z_k = h(x_k) + v_k \qquad v_k \sim \mathcal{N}(0, R_k) \tag{2.34}$$

Since the filter update equations require linear representations of the state and measurement models, these matrices are approximated by the Jacobian of the non-linear system model 2.35 and the non-linear measurement model (2.36).

$$F_k \approx J_x = \frac{\partial f(\hat{x}_{k-1|k-1})}{\partial \hat{x}_{k-1|k-1}} \tag{2.35}$$

$$H_k \approx J_z = \frac{\partial h(\hat{x}_{k|k-1})}{\partial \hat{x}_{k|k-1}} \tag{2.36}$$

Because the system model and measurement model matrices are approximated this process becomes suboptimal, but can still provide reliable results.

Both the linear Kalman filter and extended Kalman filter are predicated on the idea that there is only a single measurement at each time instant. Unfortunately, in many cases a sensor can provide multiple measurements, this problem is extremely prevalent in radar systems. The issue now becomes one of choosing the appropriate measurement(s) to update the system state.

2.6.3 Nearest Neighbor Data Association

One common method for data association is to update the system state with the measurement with the smallest normalized innovation error within a validation gate. In this approach the predicted measurement $\hat{z}_k$ is assumed to have a Gaussian distribution with variance S_k. This process provides a normalized distance equation (2.37) with respect to the ith potential measurement, $z_k(i)$, at time k out of the m_k measurements available.

$$d^2(z_k(i), S_k^{-1}) = [z_k(i) - \hat{z}_k]^T S_k^{-1} [z_k(i) - \hat{z}_k] \tag{2.37}$$

To be considered a prospective measurement the normalized distance must be less than a threshold γ. The threshold γ is chosen based on the a predetermined gating probability P_G which has a relationship that can be seen in equation (2.38).

$$P\left[d^2(z_k(i), S_k^{-1}) \leq \gamma \right] = P_G \tag{2.38}$$

This equation can be solved numerically or it can be determined in advance by using a look up table. The problem with this approach is that there is a small possibility for a wrong association which could in turn cause the track to diverge.

2.6.4 Probabilistic Data Association

To reduce the possibility of a wrong association in the nearest neighbor association approach the probabilistic data association (PDA) method was developed to use a weighted sum of all of the measurements that fall within the validation gate. An overview of the approach is covered by Bar-Shalom in [40].

In this approach, each of the m_k measurements that fall within the validation gate are given weights (2.39).

$$\beta_i(k) = \begin{cases} \dfrac{\mathcal{L}_i(k)}{1-P_D P_G + \sum_{j=1}^{m(k)} \mathcal{L}_i(k)} & i = 1, ..., m(k) \\[4mm] \dfrac{1-P_D P_G}{1-P_D P_G + \sum_{j=1}^{m(k)} \mathcal{L}_i(k)} & i = 0) \end{cases} \tag{2.39}$$

$$\mathcal{L}_i(k) = \frac{\mathcal{N}\left[z_i(k); \hat{z}_k, S_k\right] P_D}{\lambda}$$

where β_0 is the weight for the case where none of the measurements originate from the target being tracked and λ is a scaling parameter that defines the clutter density for the system. With these weights th state estimate can be updated using the weighted sum of the innovations (2.40).

$$\hat{x}_{k+1|k+1} = \hat{x}_{k+1|k} + K_{k+1}\nu_k \tag{2.40}$$

$$\nu_k = \sum_{i=1}^{m_k} \beta_k(i)[z_k(i) - \hat{z}_k]$$

These weights can again be used update the state estimate covariance (2.41).

$$P_{k+1|k+1} = \beta_0 P_{k+1|k} + (1-\beta_0)P^c_{k+1|k+1} + \tilde{P}_{k+1} \tag{2.41}$$

$$P^c_{k+1|k+1} = P_{k+1|k} K_{k+1} S_{k+1} K^T_{k+1}$$

$$\tilde{P}_{k+1} = K_{k+1} \left[\sum_{i=1}^{m(k)} \beta_i(k)[z_k(i) - \hat{z}_k][z_k(i) - \hat{z}_k]^T - \nu_k \nu_k^T \right] K^T_{k+1}$$

Through the use of this weighted sum approach, there is less of a chance of track divergence over the nearest neighbor approach. The PDA approach has also been shown to have increased performance when there is a chance of missing detections. Like many other real world applications like long range tracking radar and air traffic control radar, this approach

seems like an ideal fit for roadside vehicle tracking due to the possibility of both multiple

measurements as well as missed detections.

Chapter 3

Multi-Waveform FMCW Radar

Tracking

For the purposes of this document a three part waveform is developed which contains a period with a constant transmission frequency, a section with a linearly increasing transmission frequency, and a section with a linearly decreasing transmission frequency. The region with constant frequency acts as a more traditional Doppler radar which provides a measure of Doppler frequency and angle perturbed by additive white Gaussian noise (3.1) for targets with a large enough radar cross section within the sensor's field-of-view.

$$z_k^{dopp} = \begin{bmatrix} f_k^{Dopp} \\ \theta_k^{Dopp} \end{bmatrix} + v_k^{Dopp} \tag{3.1}$$

$$v_k^{Dopp} = \mathcal{N}\left(0, R_k^{Dopp}\right)$$

$$R_k^{Dopp} = \begin{bmatrix} \sigma_{f^{Dopp}}^2 & 0 \\ 0 & \sigma_{\theta^{Dopp}}^2 \end{bmatrix}$$

As shown in equation (2.6), this region of the signal is able to provide an accurate

measure of range-rate but lacks any information on the range to the targets. This lack of range produces the need for additional waveforms.

To help account for this lack of ranging from the Doppler section of the signal, the radar produces a region with a linearly increasing transmission frequency, also referred to as an up-chirp. After processing this region, the sensor provides an another measure of frequency and angle which is also effected by additive white Gaussian noise (3.2).

$$z_k^{Rise} = \begin{bmatrix} f_k^{Rise} \\ \theta_k^{Rise} \end{bmatrix} + v_k^{Rise} \tag{3.2}$$

$$v_k^{Rise} \sim \mathcal{N}\left(0, R_k^{Rise}\right)$$

$$R_k^{Rise} = \begin{bmatrix} \sigma_{f^{Rise}}^2 & 0 \\ 0 & \sigma_{\theta^{Rise}}^2 \end{bmatrix}$$

As seen in (2.7), the frequency information from this region will contain coupled information on the target's range and range-rate along with the angle. In order to build in some redundancy and later help with measurement formation and tracking, a region with linearly decreasing transmission frequency, or a down-chirp, finishes off the waveform chain by providing another measure of frequency and angle which is also effected by additive white Gaussian noise (3.3).

$$z_k^{Fall} = \begin{bmatrix} f_k^{Fall} \\ \theta_k^{Fall} \end{bmatrix} + v_k^{Fall} \tag{3.3}$$

$$v_k^{Fall} \sim \mathcal{N}\left(0, R_k^{Fall}\right)$$

$$R_k^{Fall} = \begin{bmatrix} \sigma_{fFall}^2 & 0 \\ 0 & \sigma_{\theta Fall}^2 \end{bmatrix}$$

The frequency of this second region with a linear frequency modulation is also a coupled function of range and range rate as seen in (2.8), but in the case of moving objects differs from that of the up-chirp region.

Assuming the up-chirp and down-chirp regions share the same bandwidth and period, and there is only a single measurement from each of the waveform sections, the decoupling of the frequency measurements into a range, range-rate, and angle measurement becomes trivial (3.4).

$$z_k^{Meas} = \begin{bmatrix} r_k \\ \dot{r}_k \\ \theta_k \end{bmatrix} = \begin{bmatrix} \frac{c_o T^{Rise}}{4\beta} \left(f_k^{Rise} + f_k^{Fall} \right) \\ \frac{c_o}{2 f_c} f_k^{Dopp} \\ \frac{\theta_k^{Dopp} + \theta_k^{Rise} + \theta_k^{Fall}}{3} \end{bmatrix} \tag{3.4}$$

Unfortunately, due to the possibility of multiple targets within the field-of-view and the high probability of false detections from the radar data the situation where there is only a single measurement from each sensor is a rare case. For most cases each waveform generates a set of detections. At a given time instant k, these sets of measurements are defined in equations (3.5-3.7).

$$Z_k^{Dopp} = \begin{bmatrix} z_k^{Dopp}(1) & z_k^{Dopp}(2) & \cdots & z_k^{Dopp}(m_k^{Dopp}) \end{bmatrix}$$

$$= \begin{bmatrix} f_k^{Dopp}(1) & f_k^{Dopp}(2) & \cdots & f_k^{Dopp}(m_k^{Dopp}) \\ \theta_k^{Dopp}(1) & \theta_k^{Dopp}(2) & \cdots & \theta_k^{Dopp}(m_k^{Dopp}) \end{bmatrix} \tag{3.5}$$

$$Z_k^{Rise} = \begin{bmatrix} z_k^{Rise}(1) & z_k^{Rise}(2) & \cdots & z_k^{Rise}(m_k^{Rise}) \end{bmatrix}$$

$$= \begin{bmatrix} f_k^{Rise}(1) & f_k^{Rise}(2) & \dots & f_k^{Rise}(m_k^{Rise}) \\ \theta_k^{Rise}(1) & \theta_k^{Rise}(2) & \dots & \theta_k^{Rise}(m_k^{Rise}) \end{bmatrix} \tag{3.6}$$

$$Z_k^{Fall} = \begin{bmatrix} z_k^{Fall}(1) & z_k^{Fall}(2) & \dots & z_k^{Fall}(m_k^{Fall}) \end{bmatrix}$$

$$= \begin{bmatrix} f_k^{Fall}(1) & f_k^{Fall}(2) & \dots & f_k^{Fall}(m_k^{Fall}) \\ \theta_k^{Fall}(1) & \theta_k^{Fall}(2) & \dots & \theta_k^{Fall}(m_k^{Fall}) \end{bmatrix} \tag{3.7}$$

For these sets of measurements, m_k^{Dopp}, m_k^{Rise}, and m_k^{Fall} are the number of measurements formed from the Doppler, up-chirp, and down-chirp waveforms respectively. In order to compensate for this high probability of multiple measurements from each waveform section, two tracking methods are developed. The first method exploits the relationships between the measurements from each waveform section to group those measurements and then form traditional range, range-rate, and angle measurements to feed into the tracking framework. In the second approach, each waveform is treated as a separate sensor and the frequency and angle measurements are used directly within the tracking structure.

3.1 Tracking with Range, Range-Rate, and Angle

The first method for tracking with the multi-waveform FMCW radar is to combine the measurements from each of the waveforms to generate a set of traditional range, range-rate, and angle measurements which can be used in a more traditional extended Kalman filter framework. A diagram of the tracking framework can be seen in Figure 3.1.

Since the objects within the field-of-view are assumed to have a constant velocity and are constrained to a road surface a standard four state constant velocity model can be used to model vehicles [35]. This provides state estimate and state covariance estimate prediction models seen in (3.8) and (3.9) respectively.
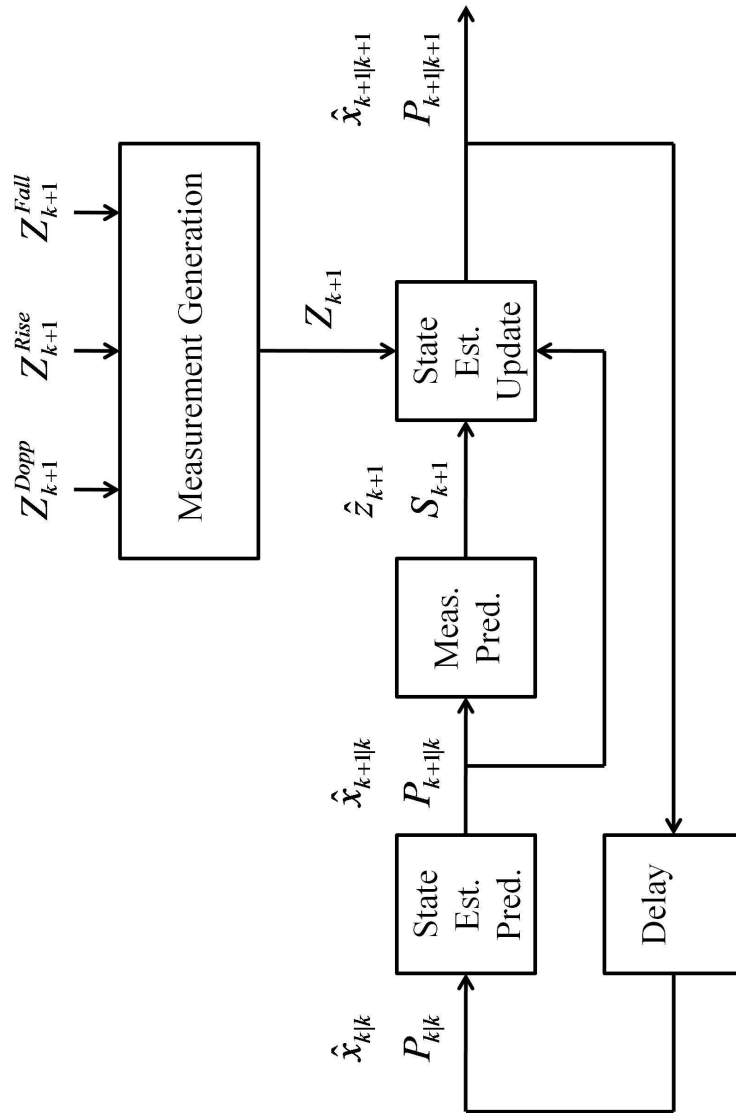
Figure 3.1: Tracking system model using polar coordinate measurements.

$$\hat{x}_{k+1|k} = F_k \hat{x}_{k|k} \tag{3.8}$$

$$P_{k+1|k} = F_k P_{k|k} F_k^T + Q_k \tag{3.9}$$

$$F_k = \begin{bmatrix} 1 & PRI & 0 & 0 \\ 0 & 1 & 0 & 0 \\ 0 & 0 & 1 & PRI \\ 0 & 0 & 0 & 1 \end{bmatrix}$$

$$Q_k = \begin{bmatrix} \frac{PRI^4}{4} & \frac{PRI^3}{2} & 0 & 0 \\ \frac{PRI^3}{2} & PRI^2 & 0 & 0 \\ 0 & 0 & \frac{PRI^4}{4} & \frac{PRI^3}{2} \\ 0 & 0 & \frac{PRI^3}{2} & PRI^2 \end{bmatrix} \sigma_a^2$$

In the above model, PRI is the time period for one full set of waveform sections to complete and σ_a^2 is the random acceleration variance that is modeled as noise in the system dynamic model.

Once state and state covariance estimate predictions are generated a predicted measurement (3.10) and innovation covariance (3.11)can be generated.

$$\hat{z}_{k+1} = h\left(\hat{x}_{k+1|k}\right) = \begin{bmatrix} \sqrt{x_{k+1|k}^2 + y_{k+1|k}^2} \\ \frac{x_{k+1|k}\dot{x}_{k+1|k} + y_{k+1|k}\dot{x}_{k+1|k}}{\sqrt{x_{k+1|k}^2 + y_{k+1|k}^2}} \\ Tan^{-1}\left(\frac{x_{k+1|k}}{y_{k+1|k}}\right) \end{bmatrix} \tag{3.10}$$

$$S_{k+1} = H_{k+1} P_{k+1|k} H_{k+1}^T + R_{k+1} \tag{3.11}$$

$$H_{k+1} \approx \frac{\partial h\left(\hat{x}_{k+1|k}\right)}{\partial \hat{x}_{k+1|k}}$$

Next, measurements must be formed in order to update the state and state covariance estimates. Since the sets of measurements from the individual waveforms are in terms of frequency and angle they must be first combined to form range, range-rate, and angle measurements. Some research has been performed on using multiple linear frequency modulations in succession to help decouple range and range-rate from the frequency measurements using range/range-rate intersection plots [41][42] or a combination of linear frequency modulation and phase shift keying (FSK) [43]. Range/range-rate intersection plots provide a decent method for decoupling range and range-rate measurements but suffer when there are a large number of false detections complicating the detection of the intersections. The combination FSK and linear frequency modulation method provides another good means of decoupling the range and range-rate with a fewer number of waveforms, but is very susceptible to radar phase noise. In [44] a voting based method was introduced to form measurements from a Doppler/up-chirp/down-chirp mixed waveform. This paper provided a better means of measurement discrimination utilizing the relationships between the overall waveform sections, but lacked a weighting metric to determine the quality of the match and did not utilize any angle information.

Assuming that the bandwidth and the pulsing period of the up-chirp and down-chirp sections are equal, for a given target the frequency measurements of that target at time instant k has a fixed relationship (3.12).

$$f_k^{Rise} - f_k^{Fall} = 2f_k^{Dopp} \tag{3.12}$$

If the overall waveform period is short enough to assume that the measurements of each waveform section originates from the same target state, the angle measurements from each waveform section should be equivalent (3.13).

$$\theta_k^{Rise} = \theta_k^{Fall} = \theta_k^{Dopp} \tag{3.13}$$

Using these relationships, a distance vector can be defined which represents the disparity between the sets of measurement combinations from each section of the overall waveform (3.14).

$$d_k(i,j,n) = G \begin{bmatrix} z_k^{Dopp}(i) \\ z_k^{Rise}(j) \\ z_k^{Fall}(n) \end{bmatrix} = G \begin{bmatrix} f_k^{Dopp}(i) \\ \theta_k^{Dopp}(i) \\ f_k^{Rise}(j) \\ \theta_k^{Rise}(j) \\ f_k^{Fall}(n) \\ \theta_k^{Fall}(n) \end{bmatrix} \tag{3.14}$$

$$G = \begin{bmatrix} 1 & 0 & -1 & 0 & -2 & 0 \\ 0 & 1 & 0 & -1 & 0 & 0 \\ 0 & 1 & 0 & 0 & 0 & -1 \\ 0 & 0 & 0 & 1 & 0 & -1 \end{bmatrix}$$

With the measurement model defined in equations (3.1-3.3) and the relationships defined in equations (3.12) and (3.13), the distance metric should be zero mean for combinations of measurements which are correct (3.15).

$$\mu_k = E\left[d_k(i,j,n)\right] = \begin{bmatrix} 0 & 0 & 0 & 0 \end{bmatrix}^T \tag{3.15}$$

Based on the same measurement noise models for the frequency measurements and the relationships for sums of Gaussian random variables, the variance for distance metric can also be determined (3.16).

$$\Sigma_k = VAR\left[d_k(i,j,n)\right] = \begin{bmatrix} \sigma^2_{d_k(i,j,n)}(1) & 0 & 0 & 0 \\ 0 & \sigma^2_{d_k(i,j,n)}(2) & 0 & 0 \\ 0 & 0 & \sigma^2_{d_k(i,j,n)}(3) & 0 \\ 0 & 0 & 0 & \sigma^2_{d_k(i,j,n)}(4) \end{bmatrix}$$

$$\tag{3.16}$$

$$\sigma^2_{d_k(i,j,n)}(1) = \sigma^2_{fRise} + \sigma^2_{fFall} + 4\sigma^2_{fDopp}$$

$$\sigma^2_{d_k(i,j,n)}(2) = \sigma^2_{\theta Dopp} + \sigma^2_{\theta Rise}$$

$$\sigma^2_{d_k(i,j,n)}(3) = \sigma^2_{\theta Dopp} + \sigma^2_{\theta Fall}$$

$$\sigma^2_{d_k(i,j,n)}(4) = \sigma^2_{\theta Rise} + \sigma^2_{\theta Fall}$$

Since there is a good possibility for multiple targets to be within the sensors field-of-view which can each generate multiple measurements, the measurement relationship vector can be used to both gate and weight possible combinations of measurements for consideration.

Using the metric defined in (3.14), the normalized distance for each combination of measurements from the individual waveforms can be determined (3.17).

$$d_k^2(i,j,n) = \left[d_k(i,j,n)\right]^T \left(\Sigma_k\right)^{-1} \left[d_k(i,j,n)\right] \tag{3.17}$$

To be considered a candidate combination, this normalized distance must be less than a found within a validation region $(V_k(\gamma))$ defined in equation (3.18).

$$V_k(\gamma) = P\left\{\mu_k : [\mu_k - d_k(i,j,n)]^T \Sigma_k^{-1} [\mu_k - d_k(i,j,n)] \leq \gamma\right\} \qquad (3.18)$$

Using the above equation, the probability of gating (P_G) can be determined by the probability that the distance metric falls within that validation gate (3.19).

$$P_G \triangleq P\left\{d_k(i,j,n) \in V_k(\gamma)\right\} \qquad (3.19)$$

Using the distance metric and the gating threshold, a measurement combination weighting matrix can be defined, which gives a weight based on the Gaussian distribution function to each possible combination (3.20).

$$W_k(i,j,n) = \left[\begin{array}{cc} exp(-\frac{1}{2}d_k^2(i,j,n)) & if \quad d_k^2(i,j,n) \leq \gamma \\ 0 & else \end{array}\right] \qquad (3.20)$$

Assuming that each measurement in a waveform section can only be used in the formation of one range/range-rate/angle measurement the maximum number of range/range-rate/angle measurements is the minimum number of measurements from any of the waveform sections (3.21).

$$m_k^{MAX} = min\left\{m_k^{Dopp}, m_k^{Rise}, m_k^{Fall}\right\} \qquad (3.21)$$

With the weighting matrix established and the number of measurements bounded, a search for the best combinations of measurements from the waveform sections can be determined. The first step in the process is to find the maximum value in the weighting matrix which will occur at $W(I,J,N)$. Since this weight originated from $z_k^{Dopp}(I)$, $z_k^{Rise}(J)$, and $z_k^{Fall}(N)$ those measurements from the original waveform segments can be used to form a polar measurement (3.22).

$$z_k^{Polar}(1) = \begin{bmatrix} r_k(1) \\ \dot{r}_k(1) \\ \theta_k(1) \end{bmatrix} = \begin{bmatrix} \frac{c_o T}{4\beta}(f_k^{Rise}(J) + f_k^{Rise}(N)) \\ \frac{c_o}{2f_c} f_k^{Dopp}(I) \\ \frac{\theta_k^{Dopp}(I) + \theta_k^{Dopp}(J) + \theta_k^{Fall}(N)}{3} \end{bmatrix} \qquad (3.22)$$

Based on the Gaussian distribution of the of the measurements the variance for this polar measurement can be derived using the rules for summing Gaussian random variables (3.23).

$$R^{Polar} = \begin{bmatrix} (\frac{c_o T}{2\beta})^2(\sigma_{fRise}^2 + \sigma_{fFall}^2) & 0 & 0 \\ 0 & (\frac{c_o}{2f_c})^2\sigma_{fDopp}^2 & 0 \\ 0 & 0 & \frac{1}{9}(\sigma_{\theta Dopp}^2 + \sigma_{\theta Rise}^2 + \sigma_{\theta Fall}^2) \end{bmatrix} \qquad (3.23)$$

Since it is assumed that each frequency and angle measurement can only be used to form one polar measurement the weighting matrix can be zeroed out along the planes corresponding to those measurements (3.24-3.26).

$$W(I, j, n) = 0 \qquad j = 1, ..., m_k^{Rise} \qquad n = 1, ..., m_k^{Fall} \qquad (3.24)$$

$$W(i, J, n) = 0 \qquad i = 1, ..., m_k^{Dopp} \qquad n = 1, ..., m_k^{Fall} \qquad (3.25)$$

$$W(i, j, N) = 0 \qquad i = 1, ..., m_k^{Dopp} \qquad j = 1, ..., m_k^{Rise} \qquad (3.26)$$

This process can then be iterated until the maximum number of possible measurements is reached or the maximum weight left in the weighting matrix equals zero, which signifies there are no more possible matches.

Once this process in complete, a set of polar measurements is available. This set of polar measurements along with the nearest neighbor or probabilistic data association method can

be used to update the target state. This entire process is repeated in order to track targets of interest.

One major complication arises with generating measurements with this method. The problem is that if there is a missed detection for a target in any one of the three waveforms, the algorithm fails to generate a range, range-rate, bearing measurement for that target even if there were detections from the other two sensors. With this in mind another approach for tracking is developed.

3.2   Tracking with Raw Frequency and Angle

Since the polar measurement formation algorithm fails if there is a missed detection on a target, another tracking algorithm was created. Instead of trying to generate polar measurements by combining the information from the waveform sections of the multi-waveform model, each waveform can be modeled as a separate sensor entirely. State estimates can be formed from each of the separate waveform segments and their results can be fused to form a single state estimate for the target of interest. There are several sources for sensor fusion techniques [45, 46] which provide the fusion fundamentals. Some specific applications to the use of distributed fusion with uncertain networks can be seen in [47] while some information about distributed filtering using set models can be found in [48]. The fusion model that best fits this radar system is the distributed data fusion model which can be performed with or without global state feedback. These two models are covered below.

3.2.1   Distributed Fusion without Global Feedback

The diagram of the overall system model for the distributed data fusion without global feedback radar tracking model can be found in Figure 3.2.

In this method, each waveform segment maintains its own track and the results from the individual tracks are fused to improve the overall state estimate of the target. To begin,
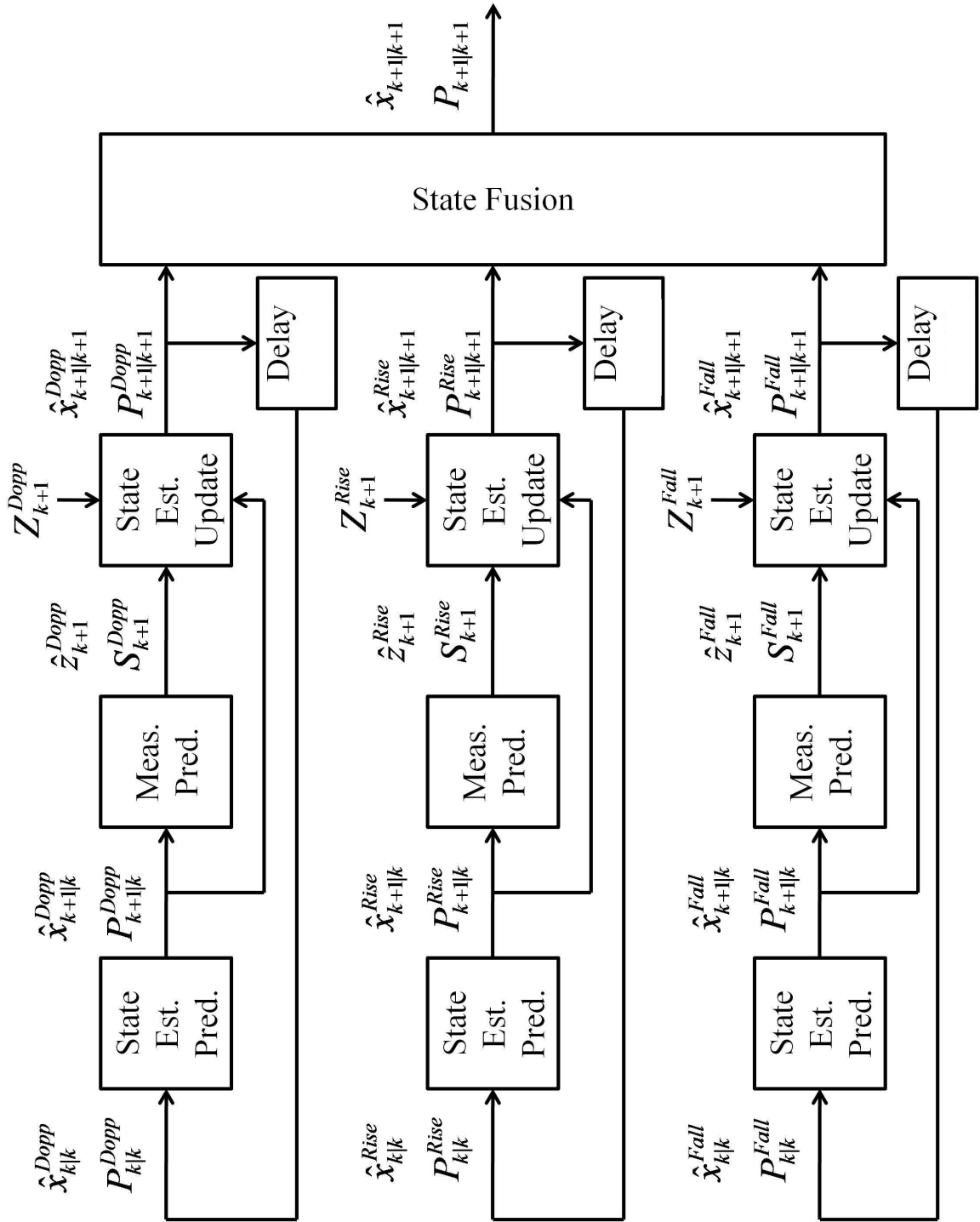
45

Figure 3.2: Tracking system model using distributed data fusion without global feedback.

each of the waveform segments is initialized with the same initial state (3.27) and state
covariance (3.28).

$$\hat{x}_{0|0}^{Dopp} = \hat{x}_{0|0}^{Rise} = \hat{x}_{0|0}^{Fall} = \hat{x}_{0|0} \tag{3.27}$$

$$P_{0|0}^{Dopp} = P_{0|0}^{Rise} = P_{0|0}^{Fall} = P_{0|0} \tag{3.28}$$

After initialization, the process begins by generating state estimate and state estimate
covariance predictions for each of the waveform segments waveform segments (3.29-3.34).

$$\hat{x}_{k+1|k}^{Dopp} = F_k \hat{x}_{k+1|k}^{Dopp} \tag{3.29}$$

$$P_{k+1|k}^{Dopp} = F_k P_{k|k}^{Dopp} F_k^T + Q_k \tag{3.30}$$

$$\hat{x}_{k+1|k}^{Rise} = F_k \hat{x}_{k+1|k}^{Rise} \tag{3.31}$$

$$P_{k+1|k}^{Rise} = F_k P_{k|k}^{Rise} F_k^T + Q_k \tag{3.32}$$

$$\hat{x}_{k+1|k}^{Fall} = F_k \hat{x}_{k+1|k}^{Fall} \tag{3.33}$$

$$P_{k+1|k}^{Fall} = F_k P_{k|k}^{Fall} F_k^T + Q_k \tag{3.34}$$

Using these state estimate predictions, a set of measurement predictions can be for-
mulated for each of the waveform segments. For the Doppler region, the measurement
prediction and innovation covariance is formulated using (3.35-3.38).

$$\hat{z}_{k+1}^{Dopp} = h^{Dopp}(\hat{x}_{k+1|k}^{Dopp}) \tag{3.35}$$

$$h^{Dopp}(\hat{x}_{k+1|k}^{Dopp}) = \begin{bmatrix} \hat{f}_{k+1}^{Dopp} \\ \hat{\theta}_{k+1}^{Dopp} \end{bmatrix} = \begin{bmatrix} -\frac{2f_c}{c_o} \frac{x_{k+1}^{Dopp} \dot{x}_{k+1}^{Dopp} + y_{k+1}^{Dopp} \dot{y}_{k+1}^{Dopp}}{\sqrt{(x_{k+1}^{Dopp})^2 + (y_{k+1}^{Dopp})^2}} \\ Tan^{-1}(\frac{x_{k+1}^{Dopp}}{y_{k+1}^{Dopp}}) \end{bmatrix} \tag{3.36}$$

$$S_{k+1}^{Dopp} = H_{k+1}^{Dopp} P_{k+1|k}^{Dopp} (H_{k+1}^{Dopp})^T + R_{k+1}^{Dopp} \tag{3.37}$$

$$H_{k+1}^{Dopp} \approx \frac{\partial h^{Dopp}(\hat{x}_{k+1|k}^{Dopp})}{\partial \hat{x}_{k+1|k}^{Dopp}} \tag{3.38}$$

While the up-chirp section of the signal has measurement and innovation covariance estimates that are generated using (3.39-3.42).

$$\hat{z}_{k+1}^{Rise} = h^{Rise}(\hat{x}_{k+1|k}^{Rise}) \tag{3.39}$$

$$h^{Rise}(\hat{x}_{k+1|k}^{Rise}) = \begin{bmatrix} \hat{f}_{k+1}^{Rise} \\ \hat{\theta}_{k+1}^{Rise} \end{bmatrix} = \begin{bmatrix} \frac{2\beta}{c_o T^{Rise}} \sqrt{(x_{k+1}^{Rise})^2 + (y_{k+1}^{Rise})^2} - \frac{2f_c}{c_o} \frac{x_{k+1}^{Rise} \dot{x}_{k+1}^{Rise} + y_{k+1}^{Rise} \dot{y}_{k+1}^{Rise}}{\sqrt{(x_{k+1}^{Rise})^2 + (y_{k+1}^{Rise})^2}} \\ Tan^{-1}(\frac{x_{k+1}^{Rise}}{y_{k+1}^{Rise}}) \end{bmatrix} \tag{3.40}$$

$$S_{k+1}^{Rise} = H_{k+1}^{Rise} P_{k+1|k}^{Rise} (H_{k+1}^{Rise})^T + R_{k+1}^{Rise} \tag{3.41}$$

$$H_{k+1}^{Rise} \approx \frac{\partial h^{Rise}(\hat{x}_{k+1|k}^{Rise})}{\partial \hat{x}_{k+1|k}^{Rise}} \tag{3.42}$$

Finally, the down-chirp section of the signal has measurement and innovation covariance estimates which are generated using (3.43-3.46).

$$\hat{z}_{k+1}^{Fall} = h^{Fall}(\hat{x}_{k+1|k}^{Fall}) \tag{3.43}$$

$$h^{Fall}(\hat{x}_{k+1|k}^{Fall}) = \begin{bmatrix} \hat{f}_{k+1}^{Fall} \\ \hat{\theta}_{k+1}^{Fall} \end{bmatrix} = \begin{bmatrix} \frac{2\beta}{c_o T^{Fall}}\sqrt{(x_{k+1}^{Fall})^2 + (y_{k+1}^{Fall})^2} + \frac{2f_c}{c_o}\frac{x_{k+1}^{Fall}\dot{x}_{k+1}^{Fall} + y_{k+1}^{Fall}\dot{y}_{k+1}^{Fall}}{\sqrt{(x_{k+1}^{Fall})^2 + (y_{k+1}^{Fall})^2}} \\ Tan^{-1}(\frac{x_{k+1}^{Fall}}{y_{k+1}^{Fall}}) \end{bmatrix} \tag{3.44}$$

$$S_{k+1}^{Fall} = H_{k+1}^{Fall} P_{k+1|k}^{Fall}(H_{k+1}^{Fall})^T + R_{k+1}^{Fall} \tag{3.45}$$

$$H_{k+1}^{Fall} \approx \frac{\partial h^{Fall}(\hat{x}_{k+1|k}^{Fall})}{\partial \hat{x}_{k+1|k}^{Fall}} \tag{3.46}$$

Now, using these measurement predictions and using either the PDA or NN data association the states and state covariance estimates are updated using the frequency and angle measurements directly from each waveform segment. These updates can then be fused at a global level (3.47-3.48).

$$P_{k+1|k+1}^{-1} = P_{k+1|k}^{-1} + \left((P_{k+1|k+1}^{Dopp})^{-1} - (P_{k+1|k}^{Dopp})^{-1}\right)$$
$$+ \left((P_{k+1|k+1}^{Rise})^{-1} - (P_{k+1|k}^{Rise})^{-1}\right) \tag{3.47}$$
$$+ \left((P_{k+1|k+1}^{Fall})^{-1} - (P_{k+1|k}^{Fall})^{-1}\right)$$

$$P_{k+1|k+1}^{-1}\hat{x}_{k+1|k+1} = (P_{k+1|k})^{-1}\hat{x}_{k+1|k} + \left((P_{k+1|k+1}^{Dopp})^{-1}\hat{x}_{k+1|k+1}^{Dopp} - (P_{k+1|k}^{Dopp})^{-1}\hat{x}_{k+1|k}^{Dopp}\right)$$
$$+ \left((P_{k+1|k+1}^{Rise})^{-1}\hat{x}_{k+1|k+1}^{Rise} - (P_{k+1|k}^{Rise})^{-1}\hat{x}_{k+1|k}^{Rise}\right)$$
$$+ \left((P_{k+1|k+1}^{Fall})^{-1}\hat{x}_{k+1|k+1}^{Fall} - (P_{k+1|k}^{Fall})^{-1}\hat{x}_{k+1|k}^{Fall}\right) \tag{3.48}$$

In the above update equations, $\hat{x}_{k+1|k}$ and $P_{k+1|k}$ are the predicted state and state covariance estimates at the global level which can be seen in equations (3.49-3.50).

$$\hat{x}_{k+1|k} = F_k \hat{x}_{k|k} \tag{3.49}$$

$$P_{k+1|k} = F_k P_{k|k} F_k^T + Q_k \tag{3.50}$$

The process can then be performed iteratively during the tracking period to provide state estimates on targets. This system is the equivalent to three sensors individually tracking targets with a single direction data path which feeds a central processor with the results from the tracking. Without this data path back to the sensor it is possible for one of the trackers to begin diverging. As one of the tracks begins to diverge, the overall accuracy will be reduced. Even though the there is a possibility for a single track to diverge the algorithm should be more robust due to the multiple state fusion.

3.2.2 Distributed Fusion with global feedback

The next logical progression would be to include a return path for data so that the global state estimates can feed into the individual waveform section trackers to improve the over-all robustness of the tracking system. Similar to the distributed fusion without feedback approach, each of the waveform segments are treated as a separate sensors. Each of these separate sensor models are used to track targets and their updates are fused. This approach is outlined in Figure 3.3.

The system is initialized with a single initial state estimate ($\hat{x}_{0|0}$) and state covariance estimate ($P_{0|0}$). After initialization, priori global state and state covariance estimate updates are used to generate a global state and state covariance prediction for the next time step (3.51-3.52).
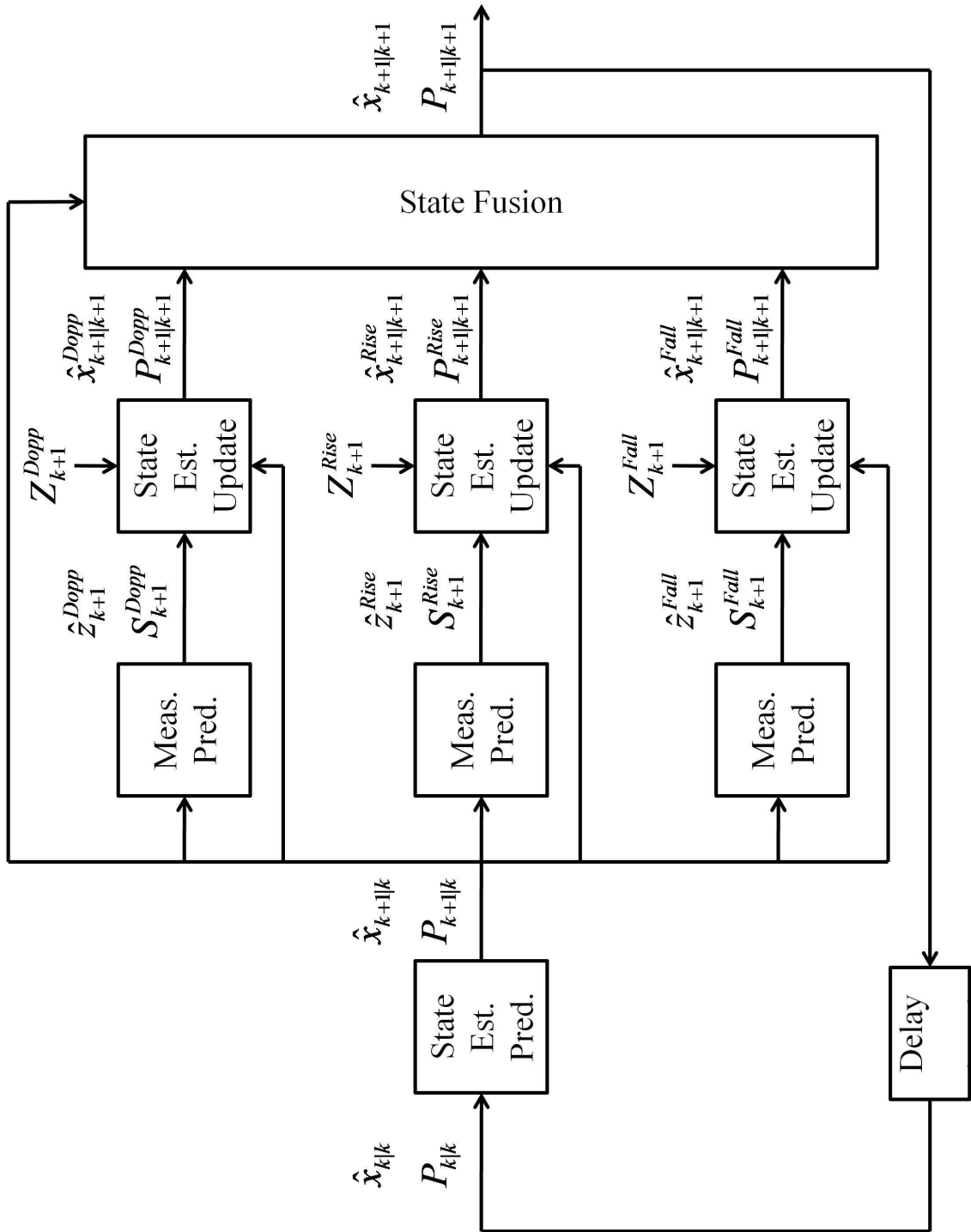
$$\hat{x}_{k+1|k} = F_k \hat{x}_{k|k} \tag{3.51}$$

Figure 3.3: Tracking system model using distributed data fusion with global feedback.

$$P_{k+1|k} = F_k P_{k|k} F_k^T + Q_k \tag{3.52}$$

This global state and state covariance prediction is then used to generate measurement predictions for each of the individual waveform segments along with their associated innovation covariance. In the case of the Doppler section the measurement prediction and the innovation covariance can be derived using (3.53-3.56)

$$\hat{z}_{k+1}^{Dopp} = h^{Dopp}(\hat{x}_{k+1|k}) \tag{3.53}$$

$$h^{Dopp}(\hat{x}_{k+1|k}) = \begin{bmatrix} \hat{f}_{k+1}^{Dopp} \\ \hat{\theta}_{k+1}^{Dopp} \end{bmatrix} = \begin{bmatrix} -\frac{2f_c}{c_o} \frac{x_{k+1}\dot{x}_{k+1}+y_{k+1}\dot{y}_{k+1}}{\sqrt{(x_{k+1})^2+(y_{k+1})^2}} \\ Tan^{-1}(\frac{x_{k+1}}{y_{k+1}}) \end{bmatrix} \tag{3.54}$$

$$S_{k+1}^{Dopp} = H_{k+1}^{Dopp} P_{k+1|k} (H_{k+1}^{Dopp})^T + R_{k+1}^{Dopp} \tag{3.55}$$

$$H_{k+1}^{Dopp} \approx \frac{\partial h^{Dopp}(\hat{x}_{k+1|k})}{\partial \hat{x}_{k+1|k}} \tag{3.56}$$

While the up-chirp section of the signal has measurement and innovation covariance estimates that are generated using (3.57-3.60).

$$\hat{z}_{k+1}^{Rise} = h^{Rise}(\hat{x}_{k+1|k}) \tag{3.57}$$

$$h^{Rise}(\hat{x}_{k+1|k}) = \begin{bmatrix} \hat{f}_{k+1}^{Rise} \\ \hat{\theta}_{k+1}^{Rise} \end{bmatrix} = \begin{bmatrix} \frac{2\beta}{c_o T^{Rise}} \sqrt{(x_{k+1})^2 + (y_{k+1})^2} - \frac{2f_c}{c_o} \frac{x_{k+1}\dot{x}_{k+1}+y_{k+1}\dot{y}_{k+1}}{\sqrt{(x_{k+1})^2+(y_{k+1})^2}} \\ Tan^{-1}(\frac{x_{k+1}^{Rise}}{y_{k+1}^{Rise}}) \end{bmatrix} \tag{3.58}$$

$$S_{k+1}^{Rise} = H_{k+1}^{Rise} P_{k+1|k} (H_{k+1}^{Rise})^T + R_{k+1}^{Rise} \tag{3.59}$$

$$H_{k+1}^{Rise} \approx \frac{\partial h^{Rise}(\hat{x}_{k+1|k})}{\partial \hat{x}_{k+1|k}} \tag{3.60}$$

Finally, the down-chirp section of the signal has measurement and innovation covariance estimates which are generated using (3.61-3.64).

$$\hat{z}_{k+1}^{Fall} = h^{Fall}(\hat{x}_{k+1|k}) \tag{3.61}$$

$$h^{Fall}(\hat{x}_{k+1|k}) = \begin{bmatrix} \hat{f}_{k+1}^{Fall} \\ \hat{\theta}_{k+1}^{Fall} \end{bmatrix} = \begin{bmatrix} \frac{2\beta}{c_o T^{Fall}} \sqrt{(x_{k+1})^2 + (y_{k+1})^2} + \frac{2f_c}{c_o} \frac{x_{k+1}\dot{x}_{k+1} + y_{k+1}\dot{y}_{k+1}}{\sqrt{(x_{k+1})^2 + (y_{k+1})^2}} \\ Tan^{-1}(\frac{x_{k+1}^{Fall}}{y_{k+1}^{Fall}}) \end{bmatrix} \tag{3.62}$$

$$S_{k+1}^{Fall} = H_{k+1}^{Fall} P_{k+1|k} (H_{k+1}^{Fall})^T + R_{k+1}^{Fall} \tag{3.63}$$

$$H_{k+1}^{Fall} \approx \frac{\partial h^{Fall}(\hat{x}_{k+1|k})}{\partial \hat{x}_{k+1|k}} \tag{3.64}$$

Once again using either the nearest neighbor or probabilistic data association methods, state estimate updates and state covariance estimate updates can be generated for each of the waveform sections using the direct frequency and angle measurements from the respective segments. These state estimate and state covariance estimate updates can then be fused to form the global state estimate and state covariance estimate update (3.66-3.65).

$$P_{k+1|k+1}^{-1} = (P_{k+1|k+1}^{Dopp})^{-1} + (P_{k+1|k+1}^{Rise})^{-1} + (P_{k+1|k+1}^{Fall})^{-1} - 2(P_{k+1|k})^{-1} \tag{3.65}$$

$$P_{k+1|k+1}^{-1}\hat{x}_{k+1|k+1} = (P_{k+1|k+1}^{Dopp})^{-1}\hat{x}_{k+1|k+1}^{Dopp} + (P_{k+1|k+1}^{Rise})^{-1}\hat{x}_{k+1|k+1}^{Rise}$$
$$+(P_{k+1|k+1}^{Fall})^{-1}\hat{x}_{k+1|k+1}^{Fall} - 2(P_{k+1|k})^{-1}\hat{x}_{k+1|k} \tag{3.66}$$

The global state estimate and state covariance estimate updates are then fed back into the system and the process repeats iteratively.

This fusion with global feedback approach has several benefits over the other two proposed methods. First, the fusion with global feedback approach does not suffer from the problem caused by missing measurements due to missed association when trying to combine the measurements from the various waveform sections. It does this by using the frequency and angle measurements directly. The second benefit to the fusion with global feedback approach is that it is more robust over the fusion without feedback approach due to the fact that the the global estimate is fed back into the system. If one of the the sections starts to diverge at a given step, the information from the global estimate fed back into the system can help move the estimates back on track.

Chapter 4

Radar-Vision Fusion

4.1 Fusion Considerations

Although the radar tracking system alone might be able to provide a sufficient state estimate for many applications, traffic surveillance systems generally require some sort of visual queue for vehicle identification. Since the vision system is required for identification, the rich angular information can be exploited to further improve the state estimate. This process can be done again through a distributed fusion scheme. Since the camera can only provide angle information on the vehicles within the scene and an angle only tracker cannot be used by itself to track in the Cartesian space, the distributed fusion without feedback will not provide a useful result. Because of this fact the only choice left for the distributed models is distributed fusion with global feedback.

Another point of interest when attempting to combine the information from the radar and vision system is that the data for these systems arrive at different measurement rates. For many applications the video rate is much lower than the radar due to the high bandwidth nature of the video data. To account for the different sensor update rates in the tracking framework the radar only tracker can be run continuously, while the fusion scheme can be applied only when a new set of camera measurements is available.

4.2 Standard Polar Measurement And Camera Fusion

In this first fusion scheme a polar measurement radar is being fused with camera measurements at time $k + 1$. The outline for the procedure can be seen in Figure 4.1.

First the state and state covariance estimates are predicted globally as seen in equations (4.1-4.2).

$$\hat{x}_{k+1|k} = F_k \hat{x}_{k+1|k} \tag{4.1}$$

$$P_{k+1|k} = F_k P_{k+1|k} F_k^T + Q_k \tag{4.2}$$

After this prediction stage, the radar can provide a state and state covariance update $(\hat{x}_{k+1|k+1}^{Radar}, P_{k+1|k+1}^{Radar})$ as described in Chapter 3.1.

The camera can also be used to generate a state estimate and state covariance update. To begin, the predicted global state and state covariance estimates are used to generate a measurement prediction (4.3) and innovation covariance estimate (4.5).

$$\hat{z}_{k+1}^{Camera} = h^{Camera}(\hat{x}_{k+1|k}) \tag{4.3}$$

$$h^{Camera}(\hat{x}_{k+1|k}) = Tan^{-1}(\frac{x_{k+1}}{y_{k+1}}) \tag{4.4}$$

$$S_{k+1}^{Camera} = H_{k+1}^{Camera} P_{k+1|k} (H_{k+1}^{Camera})^T + R_{k+1}^{Camera} \tag{4.5}$$

$$H_{k+1}^{Camera} \approx \frac{\partial h^{Camera}(\hat{x}_{k+1|k})}{\partial \hat{x}_{k+1|k}} \tag{4.6}$$

With these measures, just like with the radar, the camera also provides a state estimate and state estimate update $(\hat{x}_{k+1|k+1}^{Camera}, P_{k+1|k+1}^{Camera})$ through the use of either the the nearest
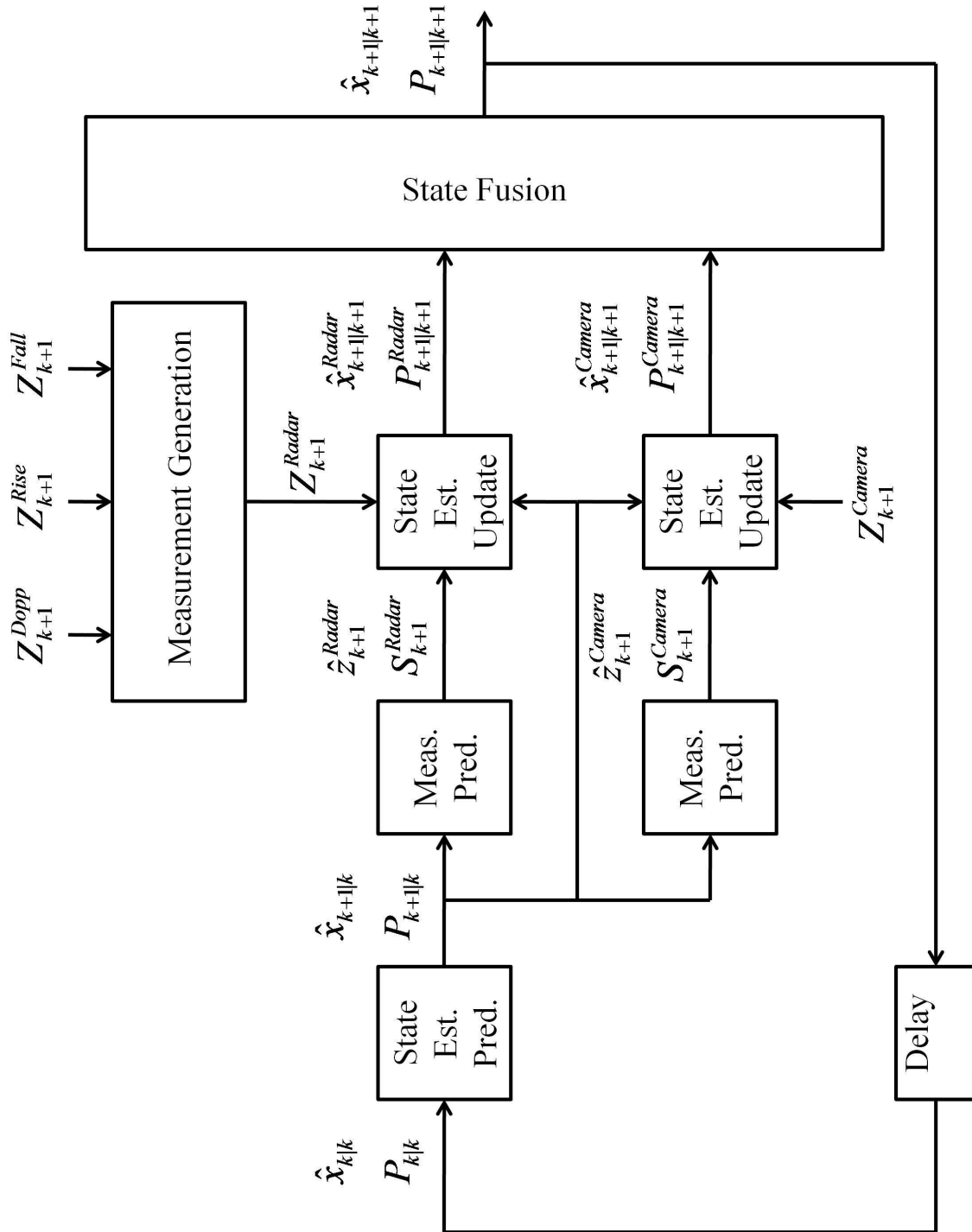
Figure 4.1: Distributed fusion with global feedback model using camera and coupled mixed measurement information.

neighbor or probabilistic data association approaches using the set of camera measurements (Z_{k+1}^{Camera}) at time $k+1$.

The estimate updates from both sensors can then be fused to form the global state estimate update (4.7) and the global state covariance estimate update (4.8).

$$P_{k+1|k+1}^{-1} = (P_{k+1|k+1}^{Camera})^{-1} + (P_{k+1|k+1}^{Radar})^{-1} - (P_{k+1|k})^{-1} \tag{4.7}$$

$$P_{k+1|k+1}^{-1}\hat{x}_{k+1|k+1} = (P_{k+1|k+1}^{Camera})^{-1}\hat{x}_{k+1|k+1}^{Camera} + (P_{k+1|k+1}^{Radar})^{-1}\hat{x}_{k+1|k+1}^{Radar} - (P_{k+1|k})^{-1}\hat{x}_{k+1|k}$$
$$\tag{4.8}$$

This process can then be repeated each time a new set of measurements arrive from the camera.

Although the state estimates for the fused system should be more accurate in most instances, the problem with missed associations in forming the standard polar domain measurements still exist. Those missing associations lead to missing measurements which could cause the track to diverge.

4.3 Complete Distributed Data Fusion with Global Feedback

To help improve on the problem of missing measurements from the polar measurement formation, the camera sensor can simply be added into the distributed data fusion model with global feedback (described in Section 3.3) as an additional sensor. A diagram of the overall process can be seen in Figure 4.2.

Like the other radar/camera fusion model the state and state covariance estimates are predicted globally $(\hat{x}_{k+1|k}, P_{k+1|k})$. Each of the waveform sections from the radar provide updates based on their models discussed in Section 3.3 $(\hat{x}_{k+1|k+1}^{Dopp}, P_{k+1|k+1}^{Dopp}, \hat{x}_{k+1|k+1}^{Rise},$
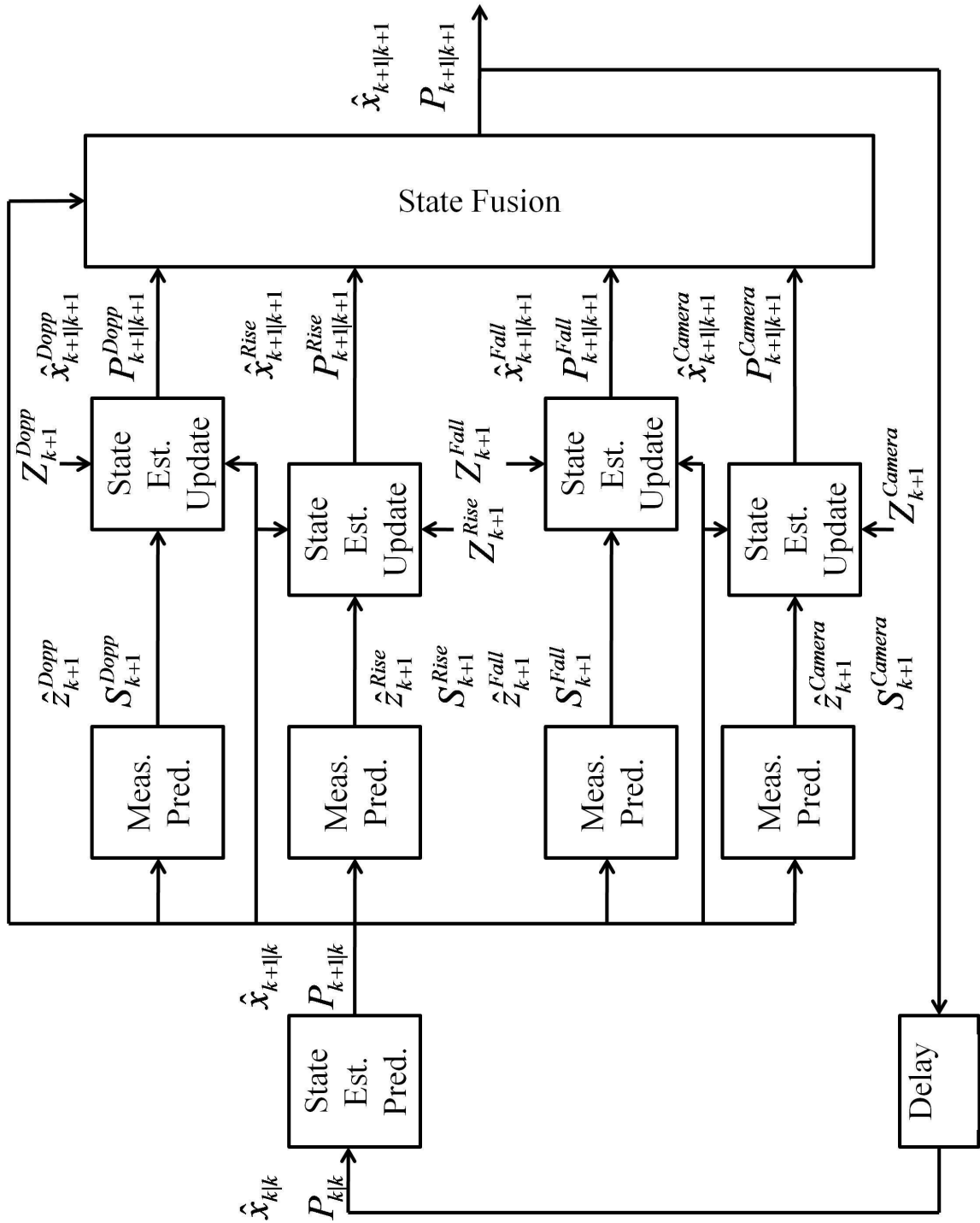
Figure 4.2: Complete distributed fusion with global feedback model.

$P_{k+1|k+1}^{Rise}$, $\hat{x}_{k+1|k+1}^{Fall}$, $P_{k+1|k+1}^{Fall}$), while the camera can provide an estimate update based on the process defined in the in the prior fusion method ($\hat{x}_{k+1|k+1}^{Camera}$, $P_{k+1|k+1}^{Camera}$). These estimates are then fused to form the global estimates (4.9 and 4.10).

$$P_{k+1|k+1}^{-1} = (P_{k+1|k+1}^{Dopp})^{-1} + (P_{k+1|k+1}^{Rise})^{-1} + (P_{k+1|k+1}^{Fall})^{-1} + (P_{k+1|k+1}^{Camera})^{-1} - 3(P_{k+1|k})^{-1}$$

(4.9)

$$\begin{aligned}
P_{k+1|k+1}^{-1}\hat{x}_{k+1|k+1} = {} & (P_{k+1|k+1}^{Dopp})^{-1}\hat{x}_{k+1|k+1}^{Dopp} + (P_{k+1|k+1}^{Rise})^{-1}\hat{x}_{k+1|k+1}^{Rise} \\
& + (P_{k+1|k+1}^{Fall})^{-1}\hat{x}_{k+1|k+1}^{Fall} + (P_{k+1|k+1}^{Camera})^{-1}\hat{x}_{k+1|k+1}^{Camera} \\
& - 3(P_{k+1|k})^{-1}\hat{x}_{k+1|k}
\end{aligned}$$

(4.10)

If there are no new camera measurements in the next time instant, then the tracker can go back to the radar only framework until another set of camera measurements arrives.

Chapter 5

Polar Measurement Validation and Application

In this section the polar measurement generation algorithm is tested using simulated data in order to validate the method. Then an algorithm is discussed which uses a set of these polar measurements over a calibration period to provide a robust road model.

5.1 Polar Measurement Generation Validation

Polar measurement generation for small radar systems, such as the one described in this paper, are of particular interest because they are the most commonly used measurements in the literature and in most tracking systems. That is why it is important to test the reliability of an algorithm which generates these measurements through the use of combining independent but related parts. In order to test the algorithm proposed in Chapter 3.1 (Gale 2011) a simulation was performed. Results of the proposed algorithm are compared to two variations of the algorithm proposed in [44]. The first variation (Hyun 2009(1)) allows measurements from the up-chirp and down-chirp regions to be used multiple times to form a set of measurements. The second variation (Hyun 2009(1)) allows each up-chirp and down-chirp measurement to be used only once in the formation of the set of polar

61

measurements.

To simulate the system scenario, the sampling frequency is partitioned into discrete pieces based on the size of the discrete Fourier transform. Two vehicles are separated by a significant distance in position with three speeds which become progressively closer (5m/s, 1m/s, and 0.5m/s differences). Frequency and angle measurements are generated from the targets using the stochastic models defined in the background material. Since the frequencies are discrete, the frequency measurement generated is reset to the closest discrete frequency value. Because the angle measurements are continuous in both the system and in the simulation, no nearest neighbor fit must be performed. Each of the remaining frequency bins has a set probability of generating a false alarm. If there is a false detection in that bin, for a given run, that frequency is added to the set of frequency measurements for that particular waveform. A random angle within the angle bounds of the system is added to complete the frequency measurement. Monte Carlo simulations were run for each scenario with varying probabilities of gating (P_G) and probabilities of false alarms (P_{FA}).

To compare performance between the proposed algorithm and variations of the traditional approach five thousand runs were performed for each combination of probability of false alarms and gating probabilities. For each simulation, the frequency and angle measurements are run through each of the measurement matching algorithms. For each algorithm, the probability of proper frequency and angle measurement association is measured. The average number of false measurements generated from the false alarms in the data are also compared using the simulation. These runs are performed for each of the differences in target speeds.

Table 5.1 represents the results for two targets separated well in position and speed (5 m/s difference in speed). This scenario is representative of data that is well separated in the Doppler measurements, as well as, well separated in the up-chirp and down-chirp measurements. As expected, with no possibility of false alarms, all three algorithms have a comparable ability to match the correct waveform segments. With the highest probability

of false alarms ($P_{FA} = 5e - 2$), the second variation of the Hyun algorithm finally starts to fail with a twenty-five percent less chance to match the correct measurements from the waveform segments over the proposed algorithm.

Method	P_G	P_{FA} 0	P_{FA} $1e - 3$	P_{FA} $5e - 3$	P_{FA} $1e - 2$	P_{FA} $5e - 2$
Gale 2011	0.90	0.882	0.874	0.859	0.845	0.709
Gale 2011	0.95	0.926	0.911	0.899	0.898	0.714
Gale 2011	0.99	0.979	0.976	0.964	0.942	0.722
Hyun 2009(1)	0.90	0.911	0.896	0.877	0.857	0.687
Hyun 2009(1)	0.95	0.934	0.933	0.904	0.885	0.698
Hyun 2009(1)	0.99	0.980	0.973	0.946	0.918	0.712
Hyun 2009(2)	0.90	0.911	0.886	0.855	0.785	0.465
Hyun 2009(2)	0.95	0.934	0.921	0.863	0.806	0.468
Hyun 2009(2)	0.99	0.980	0.964	0.911	0.837	0.475

Table 5.1: Probability of Correct Measurement Association (5m/s Speed Difference)

The next test was to leave the vehicle positions in the same place as the last set, but to decrease the absolute difference between the two vehicles' speeds. Table 5.2 shows the probabilities of correct association generated by the three algorithms when the difference between the vehicles' speeds is only 1 m/s. This scenario implies that the true measurements from the up-chirp and down-chirp regions are still well separated, but the frequencies of the true Doppler measurements are getting closer. Regardless of the probability of false alarms or the probability of gating, the algorithm proposed in the research provides better performance over the Hyun variations. In the case of the highest probability of false alarms ($P_{FA} = 5e - 2$), Hyun 2009(1) algorithm is around six to nine percent less likely, and the Hyun 2009(2) is between twenty to twenty-five percent less likely to form the proper association over the algorithm proposed by this research.

Finally, in the last scenario, the target positions are still fixed in the same locations as in the last two scenarios, but the difference in the target speeds is reduced to only 0.5 m/s. This reduction in the difference in vehicles' speeds further reduces the difference between their frequencies in the true Doppler region measurements. Table 5.3 provides the proba-

Method	P_G	P_{FA} 0	P_{FA} 1e−3	P_{FA} 5e−3	P_{FA} 1e−2	P_{FA} 5e−2
Gale 2011	0.90	0.720	0.718	0.716	0.706	0.591
Gale 2011	0.95	0.757	0.758	0.753	0.727	0.613
Gale 2011	0.99	0.795	0.788	0.779	0.767	0.630
Hyun 2009(1)	0.90	0.673	0.665	0.661	0.642	0.539
Hyun 2009(1)	0.95	0.689	0.696	0.669	0.652	0.540
Hyun 2009(1)	0.99	0.717	0.713	0.692	0.672	0.565
Hyun 2009(2)	0.90	0.673	0.661	0.644	0.607	0.387
Hyun 2009(2)	0.95	0.689	0.692	0.652	0.615	0.388
Hyun 2009(2)	0.99	0.717	0.708	0.668	0.632	0.397

Table 5.2: Probability of Correct Measurement Association (1m/s Speed Difference)

bility of proper matching for the combinations of gating probabilities and false alarm rates. The proposed algorithm still has better performance over the traditional methods. When the probability of false alarms is the greatest ($P_{FA} = 5e-2$) the proposed algorithm has between ten and twenty percent greater probability of correctly associating the measurements from the waveform segments.

Method	P_G	P_{FA} 0	P_{FA} 1e−3	P_{FA} 5e−3	P_{FA} 1e−2	P_{FA} 5e−2
Gale 2011	0.90	0.686	0.682	0.683	0.671	0.562
Gale 2011	0.95	0.708	0.724	0.714	0.705	0.583
Gale 2011	0.99	0.759	0.749	0.741	0.740	0.589
Hyun 2009(1)	0.90	0.591	0.587	0.581	0.557	0.476
Hyun 2009(1)	0.95	0.600	0.600	0.592	0.576	0.479
Hyun 2009(1)	0.99	0.631	0.614	0.613	0.585	0.490
Hyun 2009(2)	0.90	0.591	0.584	0.569	0.529	0.351
Hyun 2009(2)	0.95	0.600	0.597	0.579	0.543	0.355
Hyun 2009(2)	0.99	0.631	0.611	0.595	0.553	0.359

Table 5.3: Probability of Correct Measurement Association (0.5m/s Speed Difference)

The mean number of erroneous polar measurements formed by each method with respect to the simulation parameters can be seen in Table 5.4. As expected, when the probability of false alarms increases, the average number of false measurements each algorithm

generates increases. This observation can be accounted for by the increased number of false detections from the individual waveform segments. The method proposed by this research provides two to twenty times fewer erroneous measurements over the traditional approaches. The first variation of the Hun method provides many more false measurements due to the ability to use each measurement more than once. Using the second variation of the Hyun method provides a significant reduction in the number of false measurements (two to three times less), but sacrifices the probability of correctly associating the true waveform section measurements.

Method	P_G	P_{FA} 0	P_{FA} $1e-3$	P_{FA} $5e-3$	P_{FA} $1e-2$	P_{FA} $5e-2$
Gale 2011	0.90	0.327	0.334	0.349	0.396	2.527
Gale 2011	0.95	0.363	0.352	0.375	0.419	3.021
Gale 2011	0.99	0.389	0.409	0.437	0.487	3.924
Hyun 2009(1)	0.90	0.709	0.770	1.216	2.594	72.594
Hyun 2009(1)	0.95	0.726	0.770	1.308	2.768	77.663
Hyun 2009(1)	0.99	0.725	0.821	1.484	3.356	89.783
Hyun 2009(2)	0.90	0.817	0.995	2.543	4.748	24.012
Hyun 2009(2)	0.95	0.801	0.968	2.494	4.748	24.077
Hyun 2009(2)	0.99	0.739	0.947	2.512	4.734	24.031

Table 5.4: Mean False Measurements Generated

In general, the trends in the table reveal some encouraging results. First, for the proposed algorithm, the probability of properly matching the measurements from the individual waveform segments is directly related to the probability of gating. The proposed algorithm is also more robust to the number of false alarms over the variations on the traditional approach. For the two variations of the algorithm proposed by Hyun et al., as the number of possible false alarms increases, the probability of matching the measurements from the individual waveform segments decreases. In the case of the second variation, the probability significantly decreases with the number of possible false alarms. Second, in the proposed algorithm, there is a significant decrease in the number of false polar measurements generated over the two variations of the Hyun algorithm.

These results show that even in the presence of many false alarms, the algorithm defined by this research is still able to successfully match measurements from the separate waveform segments more robustly over the current method, which can then in turn be used to generate polar coordinate measurements. Because of the angular discrimination, the proposed algorithm generates fewer erroneous polar measurements in the presence of many false detections in the individual waveform sections. Unfortunately, the algorithm still cannot handle situations where there is a missing detection from one of the waveform sections.

5.2   Road Modeling With Polar Measurements

The polar measurements from this radar can also be used for road modeling which can aid in error analysis and target initialization. Based on the system constraints defined in the problem formulation, the road can be modeled as a set of parallel lanes which can be seen in Figure 5.1.

Over a calibration period, the range and angle portion of the polar radar measurements can be projected onto the X-Y plane. As long as vehicles have traveled in all lanes that need to be modeled there should be projected detections on all of the lanes on the X-Y plane. An example of this can be seen in Figure 5.2.

In this projection of the range and angle information onto the X-Y plane the three distinct lanes that define this example road can be seen. Since the lanes can be defined as a lines that run perpendicular to a range and an angle, a Hough transform [49] can be applied using the X-Y projections. The Hough transform of the projected points can be seen in Figure 5.3.

The lane most traveled during the calibration should be represented as the peak of the Hough accumulator, and since the road lanes are all parallel they will fall at some range along the same angle as the strongest peak. The magnitude of the accumulator along the
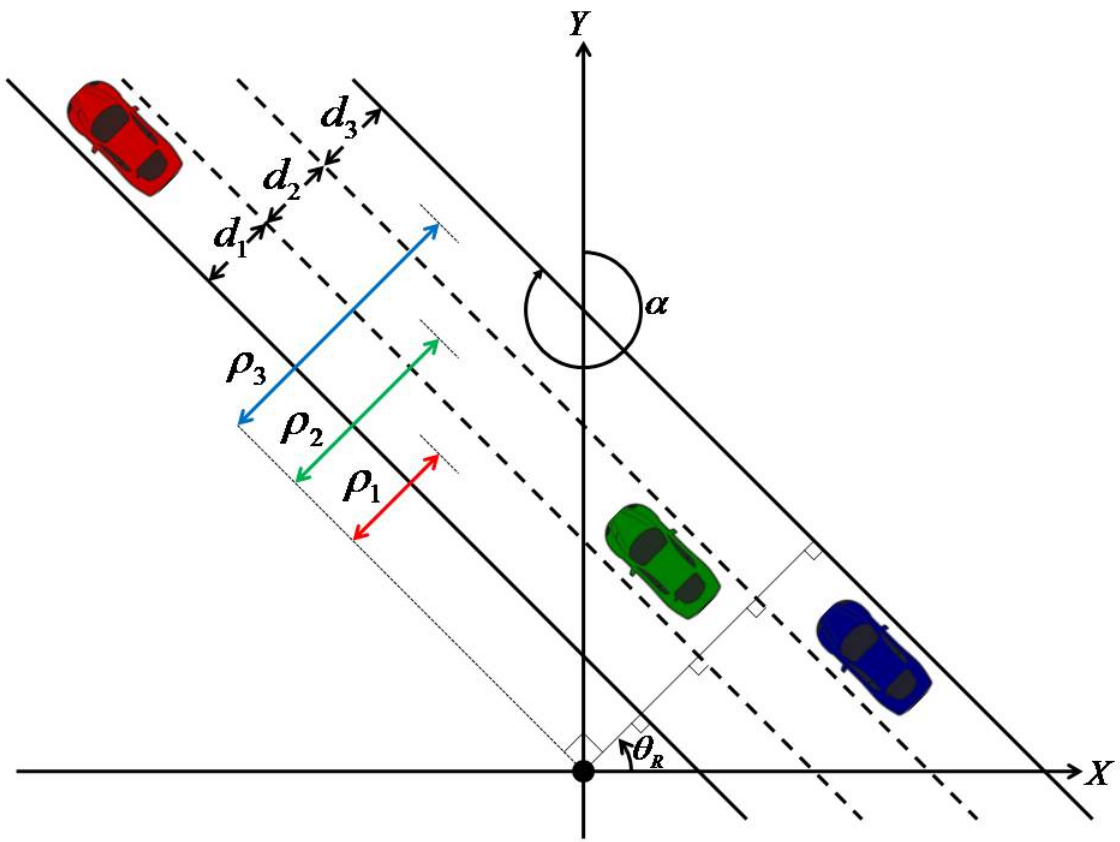
Figure 5.1: Parallel lane road model.
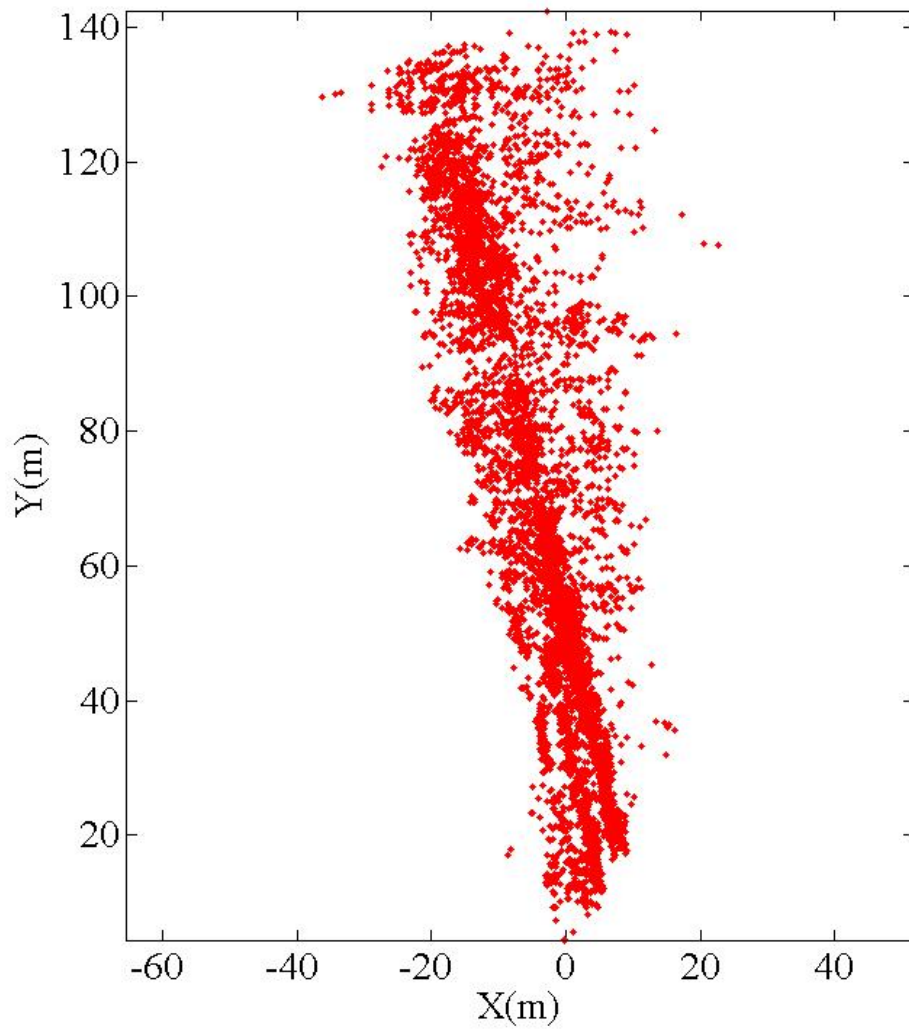
Figure 5.2: Projection of the range/angle measurements onto the X-Y plane.
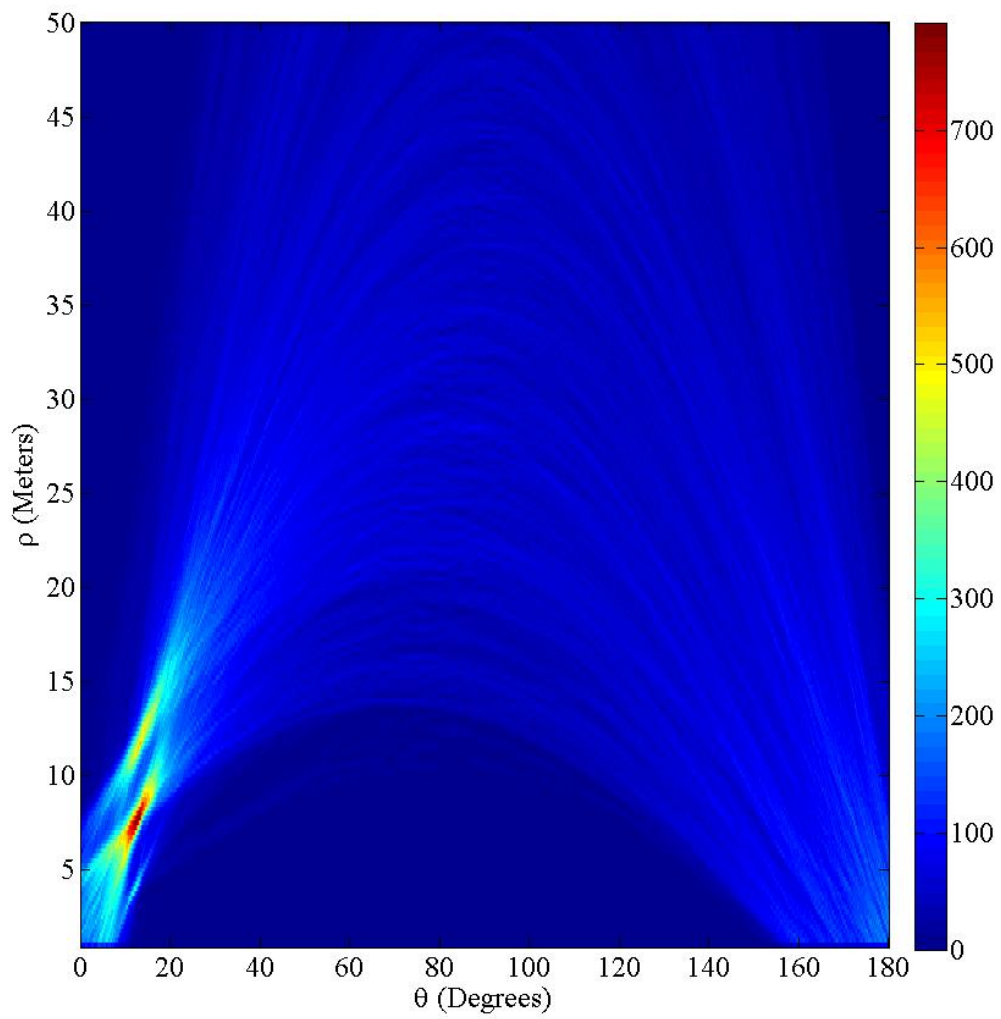
Figure 5.3: Hough accumulator array.

angle which contains the peak in the transform can be seen in Figure 5.4.
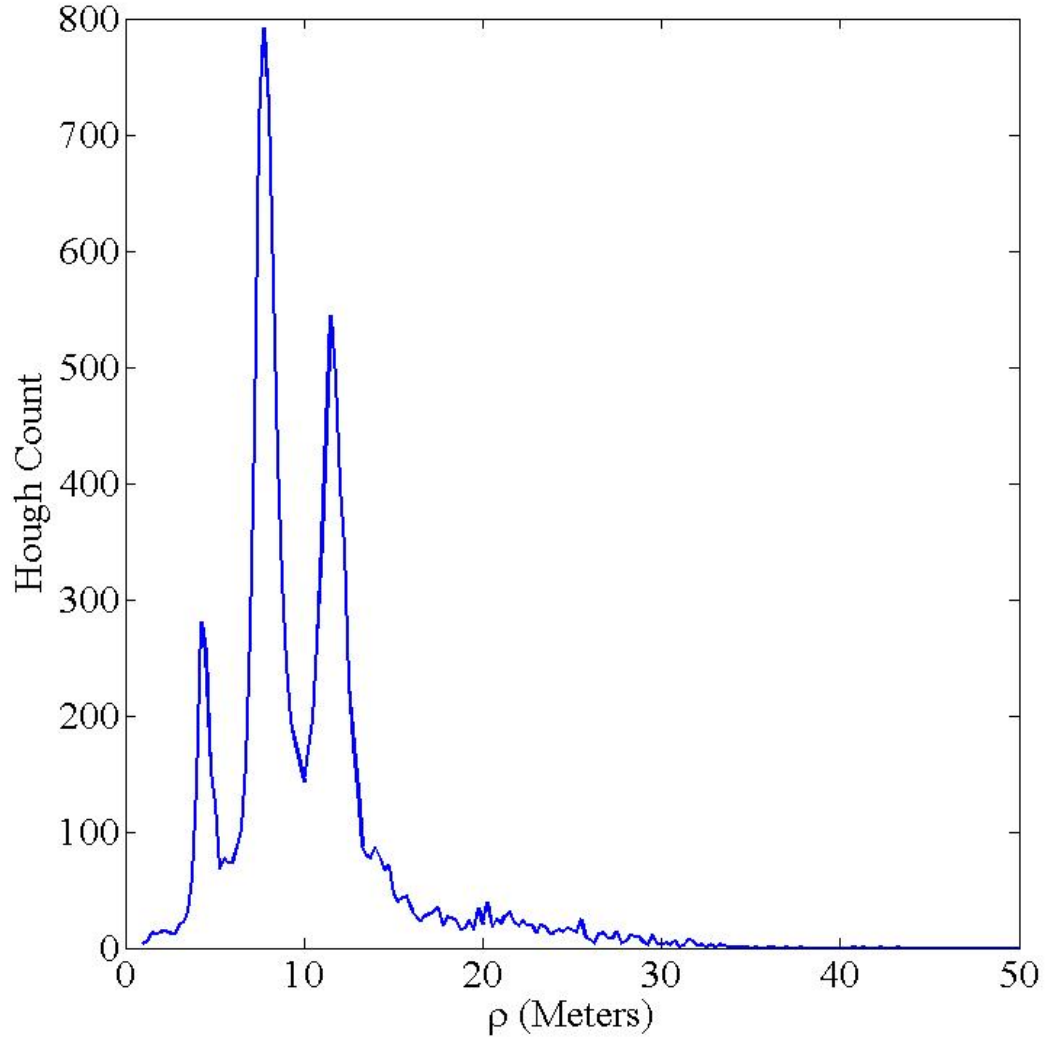
Figure 5.4: Single theta slice corresponding of peak of Hough accumulator.

It is fairly obvious from this slice of the Hough accumulator array that there are three distinct lanes from the projected data. After isolating the peaks, the angle and range parameter that defines the line are known for each lane (5.1).

$$L_1^{Pol} = [\rho_1, \theta_1] \qquad L_2^{Pol} = [\rho_2, \theta_2] \qquad L_3^{Pol} = [\rho_3, \theta_3] \qquad (5.1)$$

These polar road parameters can easily be transformed into a linear function with re-

spect to the X-Y coordinate space through equation (5.2).

$$L_x^{Cart} = [m_x, b_x] = [-\frac{cos(\theta_x)}{sin(\theta_x)}, \frac{\rho_x}{sin(\theta_x)}] \qquad (5.2)$$

where m_x and b_x are the coefficients for a linear function with respect to the x position. An overlay of the lane models onto the point projections can be seen in Figure 5.5.
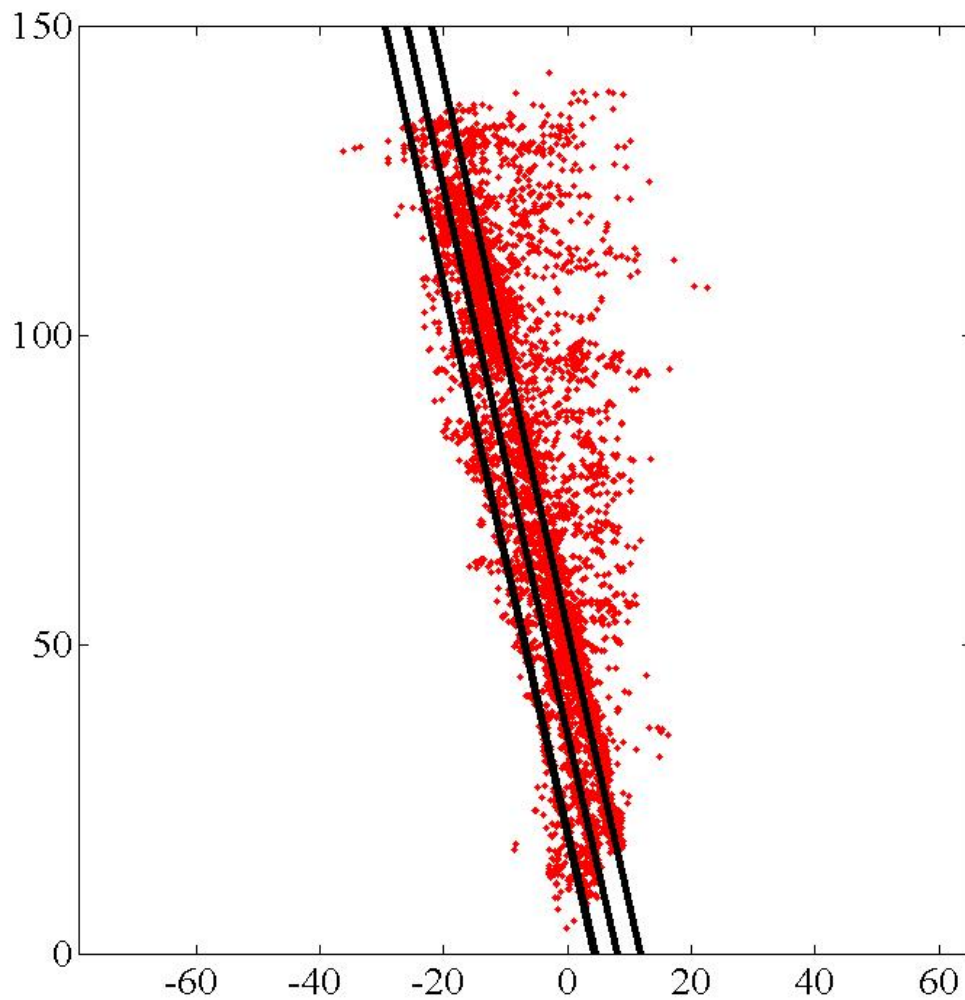
Figure 5.5: Hough accumulator array.

Visually, these models seem to accurately model the lanes of this highway scenario. Since the model fits the road well, an analytic function that define the road is in hand which

can be used as a makeshift metric for comparing tracking results.

Chapter 6

Tracking Results

6.1 Simulation Results

In order to test the performance of the system architectures, Monte-Carlo simulations were performed. Measurements generated for each period were fed into each of the tracking methods using both the nearest neighbor and probabilistic data association approaches. False detections were added, along with the true measurements ,in order to simulate scenarios with varying clutter densities. The state estimates from each set of simulations were compared against the ground truth to form RMS position and velocity errors, while the state covariance estimates along with the ground truth and state estimates were used to generate the normalized state error. The mean of these errors over the fifty Monte-Carlo runs for the various densities of false alarms and tracking structures can then be compared to get a feel for the overall performance of the individual systems. For this experiment a base case with no possible false alarms is used as a control, while the possible number false alarms per waveform segment is increased.

6.1.1 Position Errors

Mean position errors were calculated by taking the mean euclidean distance in position between the state updates and the ground truth over the fifty Monte-Carlo runs at a given scan index. The control plot which has no false detection can be seen in Figure 6.1 while the results from the simulations where there is a possibility of ten, twenty, or forty additional false measurements can be seen in Figures 6.2-6.4 respectively. A table of the mean steady state error (mean of the last 50 scans) for the various combinations can be seen in Table 6.1.

Tracker	Data Assoc.	FA_{Max} 0	FA_{Max} 10	FA_{Max} 20	FA_{Max} 40
POL	NN	0.434	0.546	0.576	0.504
WOF	NN	0.456	0.894	0.764	1.164
WIF	NN	0.220	0.367	0.299	0.600
POL+CAM	NN	0.305	0.326	0.406	0.378
WIF+CAM	NN	0.151	0.341	0.378	0.461
POL	PDA	0.437	0.548	0.568	0.506
WOF	PDA	0.216	0.213	0.244	0.268
WIF	PDA	0.217	0.214	0.239	0.270
POL+CAM	PDA	0.291	0.323	0.361	0.359
WIF+CAM	PDA	0.150	0.165	0.179	0.168

- POL = Polar Tracker

- WOF = Distributed Fusion without Global Feedback

- WIF = Distributed Fusion with Global Feedback

- POL+CAM = Polar Radar-Camera Tracker

- WIF+CAM = Distributed Radar-Camera Fusion with Global Feedback

Table 6.1: Mean Steady-State RMS Position Errors (m)

Several observations can be made about the mean position errors. First, for the control case where there are no false alarms, the PDA and NN approaches have nearly identical results with the exception of the distributed data fusion without feedback. The distributed

data fusion with feedback approach in this control case was similar to the polar measurement tracker using nearest neighbor association and is nearly identical to the distributed data fusion with feedback for the case where PDA was utilized. In all cases, systems that used the camera measurements as part of their update strategy had smaller mean RMS position errors in their estimates. As expected, as the number of possible false alarms increases, the mean errors increase significantly in arrangements that used the nearest neighbor approach. Although a small increase in the overall error is observable in the configurations with the PDA method used, the errors remain fairly equal regardless of the clutter density. For most of the scenarios, the systems using the distributed fusion with feedback model had the smallest mean errors, with the system also using the camera measurements having the lowest mean position error in most cases. The performance of the distributed fusion without feedback degrades significantly as the clutter density increases when using the NN association.

Table 6.1 provides some additional insight on trends in the system performance. In general, the probabilistic data association approach provides a mean steady state RMS position error that is two to three times less than the counterparts using nearest neighbor data association. The radar-camera tracking systems have between a twenty and thirty percent decrease in steady state RMS position error over the radar-only counterparts. Last, the distributed fusion radar-camera tracking with global feedback provides the best overall performance with approximately a twenty percent decrease in the error over the closest competing configuration.

(a) Nearest Neighbor Data Association

(b) Probabilistic Data Association

Polar Coordinate EKF		Polar Coordinate EKF + Camera	
Distributed Data Fusion wo/ Feedback		Distributed Data Fusion w/ Feedback + Camera	
Distributed Data Fusion w/ Feedback			
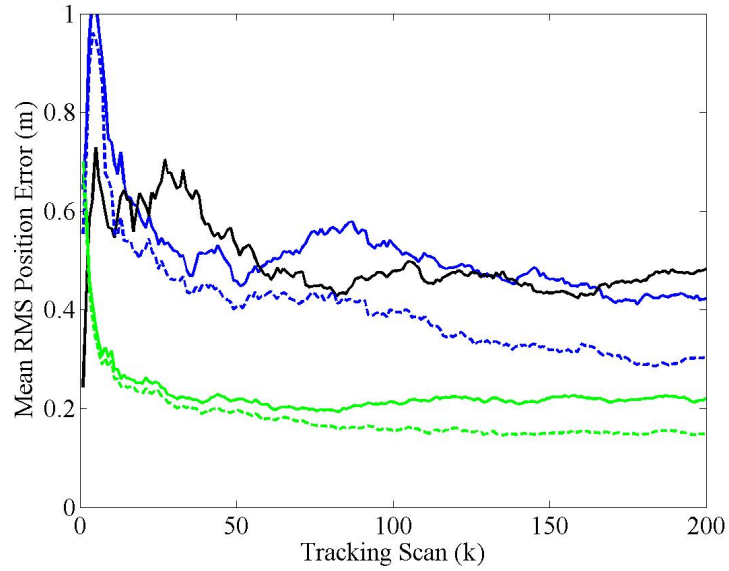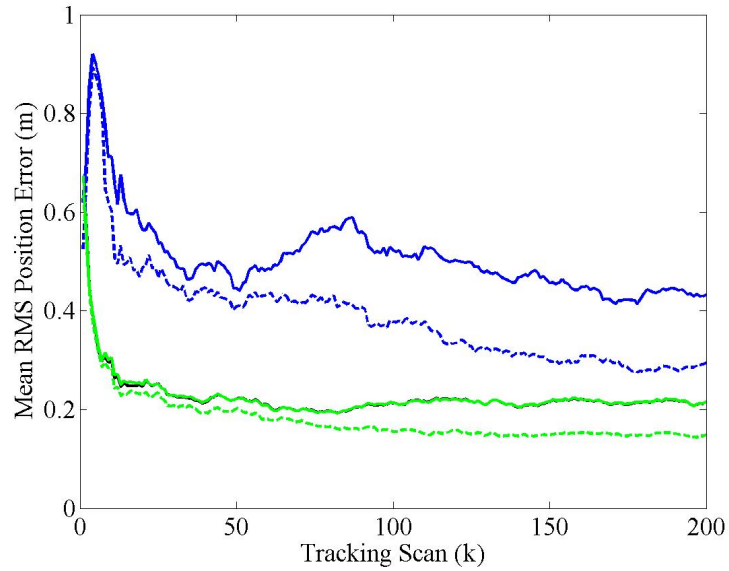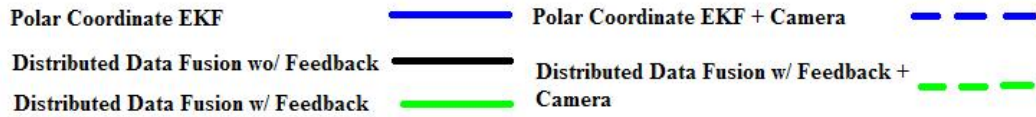
Figure 6.1: Mean RMS position error over 50 Monte Carlo simulations (NFA=0).

(a) Nearest Neighbor Data Association
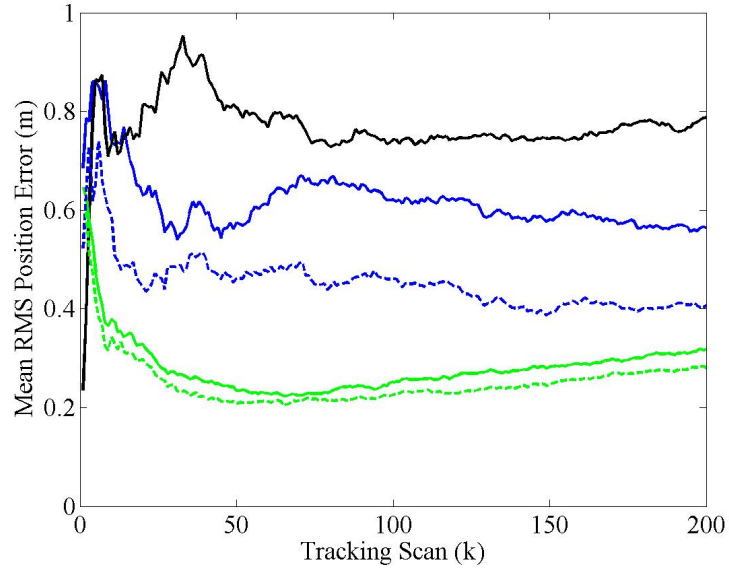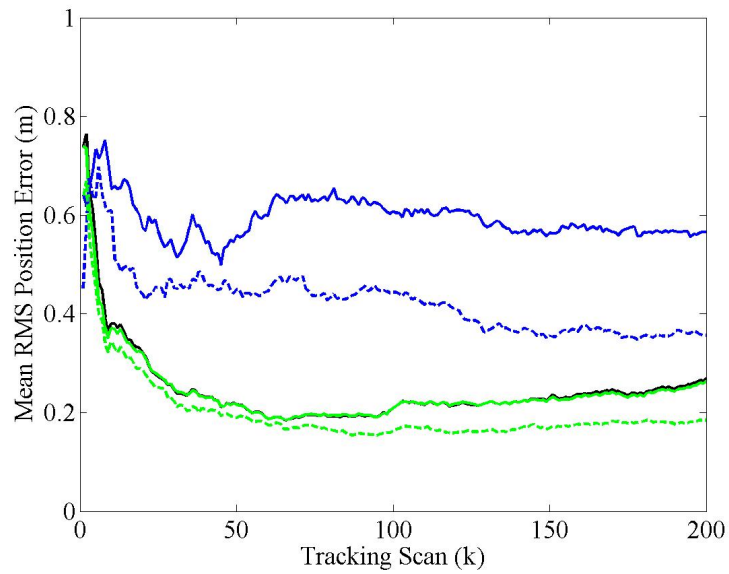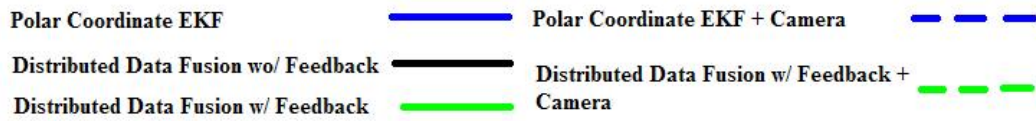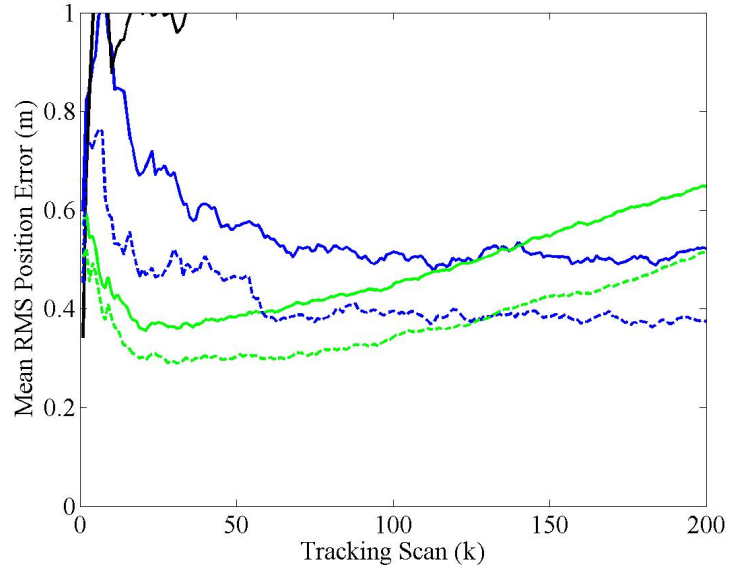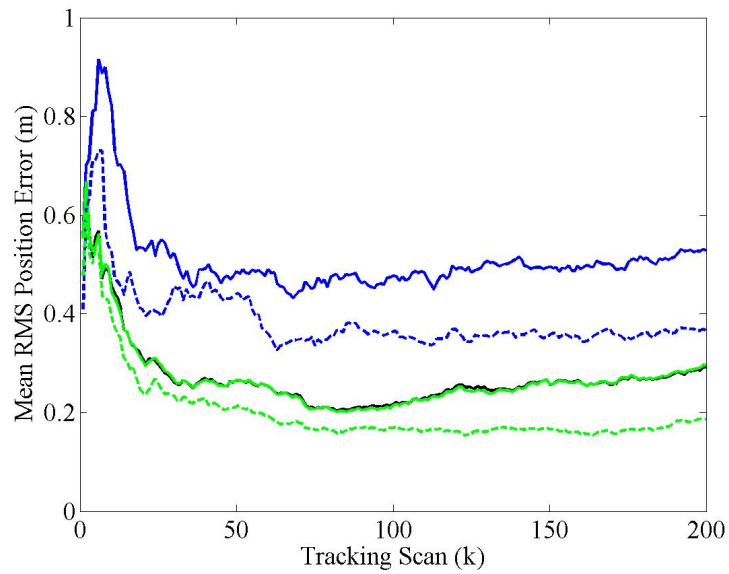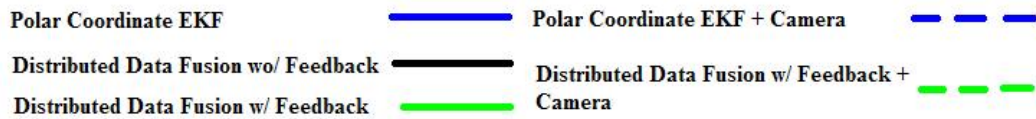

(b) Probabilistic Data Association

Polar Coordinate EKF

Distributed Data Fusion wo/ Feedback

Distributed Data Fusion w/ Feedback

Polar Coordinate EKF + Camera

Distributed Data Fusion w/ Feedback + Camera
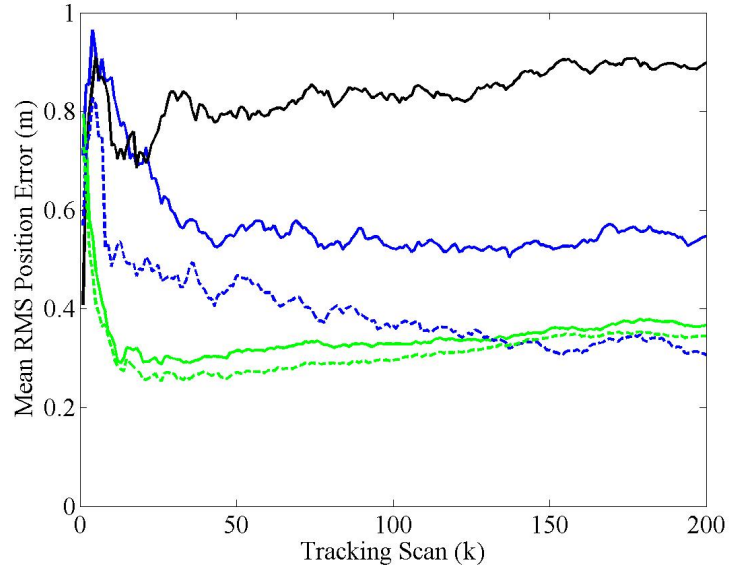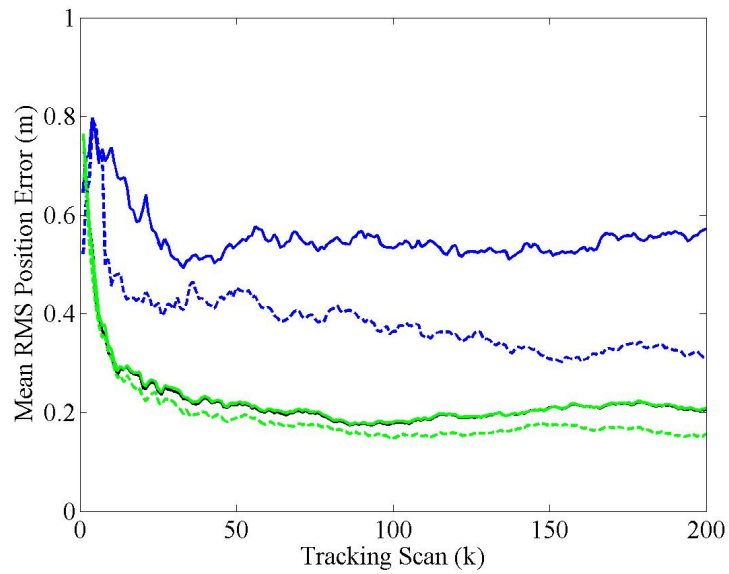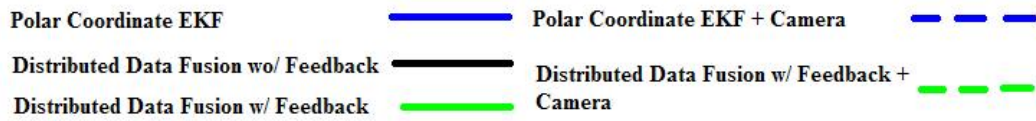
Figure 6.2: Mean RMS position error over 50 Monte Carlo simulations (NFA=10).

(a) Nearest Neighbor Data Association

(b) Probabilistic Data Association

Polar Coordinate EKF ——— **Polar Coordinate EKF + Camera** – – –

Distributed Data Fusion wo/ Feedback ——— **Distributed Data Fusion w/ Feedback + Camera** – – –

Distributed Data Fusion w/ Feedback ———

Figure 6.3: Mean RMS position error over 50 Monte Carlo simulations (NFA=20).

(a) Nearest Neighbor Data Association

(b) Probabilistic Data Association

Polar Coordinate EKF ————

Polar Coordinate EKF + Camera — — —

Distributed Data Fusion wo/ Feedback ————

Distributed Data Fusion w/ Feedback + Camera — — —

Distributed Data Fusion w/ Feedback ————

Figure 6.4: Mean RMS position error over 50 Monte Carlo simulations (NFA=40).

6.1.2 Velocity Errors

Similarly to the mean position error, the mean velocity error was calculated by taking the mean euclidean distance in velocity between the state updates and the ground truth over the fifty Monte-Carlo runs at a given scan index. The control plot which has no false detection can be seen in Figure 6.5 while the results from the simulations where there is a possibility of ten, twenty, or forty additional false measurements can be seen in Figures 6.6-6.8, respectively. A table of the mean steady state RMS velocity errors (mean of the last 50 scans) for the various tracking models and false alarm rates can be seen in Table 6.2.

Tracker	Data Assoc.	FA_{Max} 0	FA_{Max} 10	FA_{Max} 20	FA_{Max} 40
POL	NN	0.134	0.162	0.152	0.150
WOF	NN	0.101	0.231	0.153	0.225
WIF	NN	0.063	0.132	0.089	0.203
POL+CAM	NN	0.097	0.099	0.108	0.098
WIF+CAM	NN	0.045	0.136	0.091	0.165
POL	PDA	0.135	0.159	0.157	0.145
WOF	PDA	0.062	0.069	0.073	0.084
WIF	PDA	0.063	0.070	0.070	0.085
POL+CAM	PDA	0.095	0.099	0.098	0.093
WIF+CAM	PDA	0.046	0.055	0.056	0.055

- POL = Polar Tracker

- WOF = Distributed Fusion without Global Feedback

- WIF = Distributed Fusion with Global Feedback

- POL+CAM = Polar Radar-Camera Tracker

- WIF+CAM = Distributed Radar-Camera Fusion with Global Feedback

Table 6.2: Mean Steady-State RMS Velocity Errors (m/s)

In the case of velocity errors, the number of possible false alarms seems to have little effect on the overall mean error. The nearest neighbor data association approach errors

move around a little bit as the number of possible false alarms increases, but not significantly. There is very little difference in the velocity errors as the number of possible false alarms increases for the PDA cases. In general, systems that utilize the PDA approach have a steady state RMS velocity error of two to three times less than the NN counterparts. This velocity stability can be attributed the higher accuracy range-rate measurements that come from the Doppler region of the multi-waveform signal. Like the position error, the distributed fusion radar-camera tracking system with global feedback seems to have consistently lower mean RMS error with respect to velocity. Another interesting phenomenon is that the data association approach has little effect on the performance of the polar measurement based trackers.

(a) Nearest Neighbor Data Association

(b) Probabilistic Data Association

Polar Coordinate EKF ——————

Polar Coordinate EKF + Camera – – –

Distributed Data Fusion wo/ Feedback ——————

Distributed Data Fusion w/ Feedback + Camera – – –
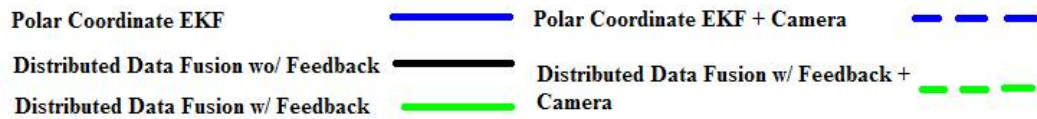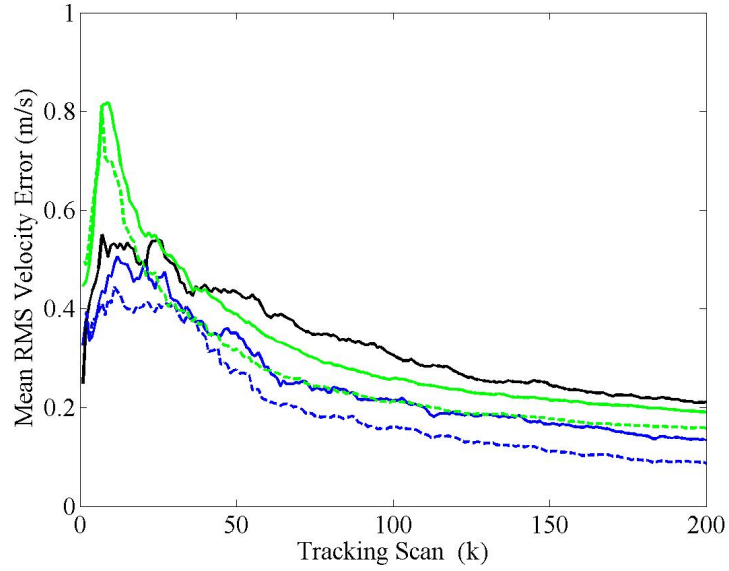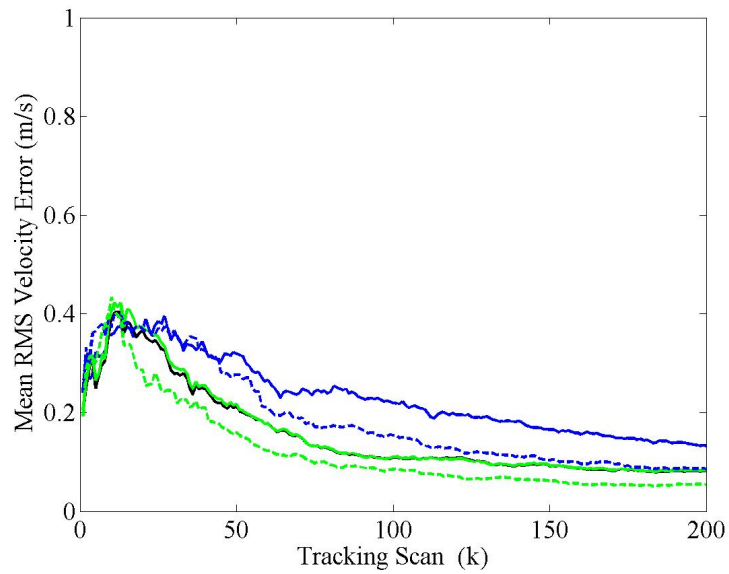
Distributed Data Fusion w/ Feedback ——————
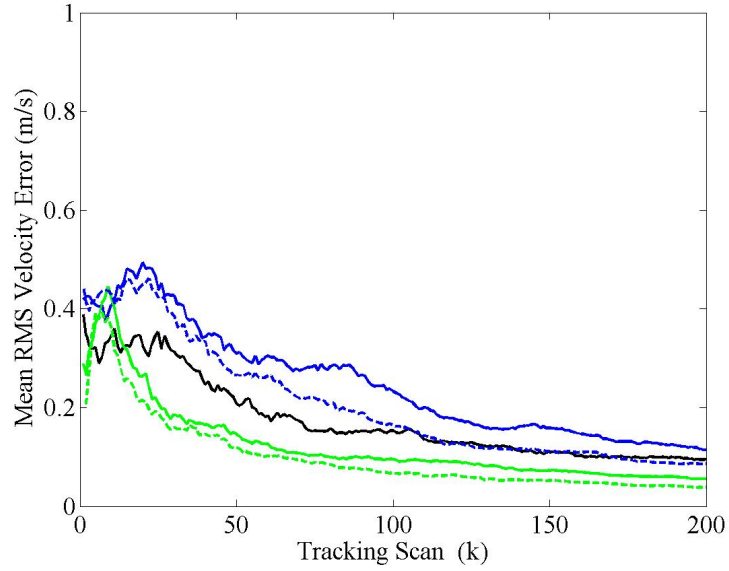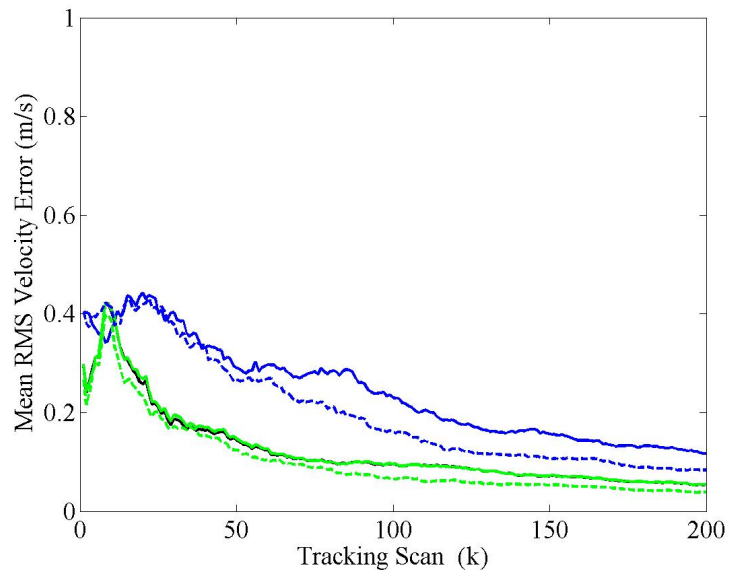
Figure 6.5: Mean RMS velocity error over 50 Monte Carlo simulations (NFA=0).

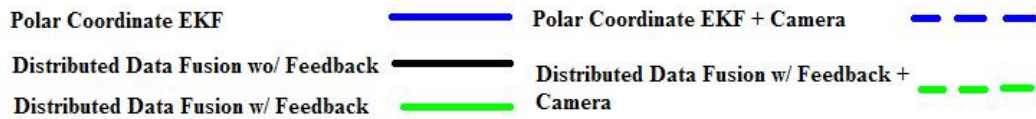(a) Nearest Neighbor Data Association

(b) Probabilistic Data Association

Polar Coordinate EKF ━━━   **Polar Coordinate EKF + Camera** ━ ━ ━

Distributed Data Fusion wo/ Feedback ━━━   **Distributed Data Fusion w/ Feedback +**

Distributed Data Fusion w/ Feedback   **Camera** ━ ━ ━
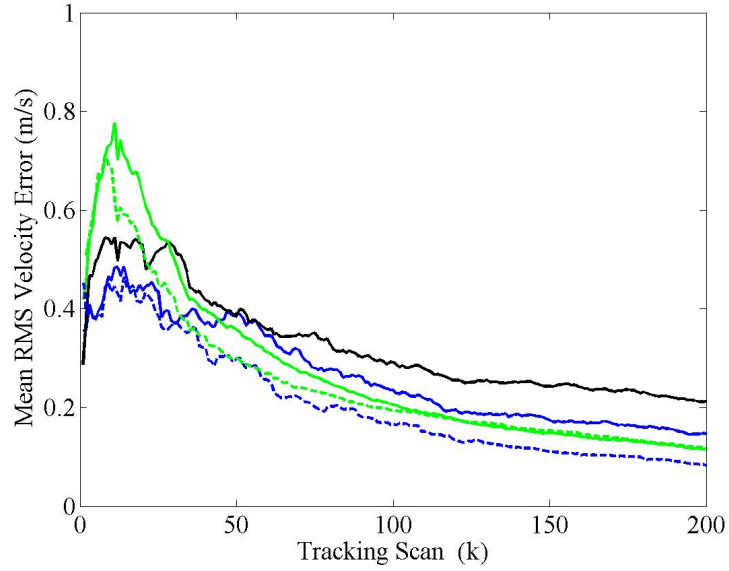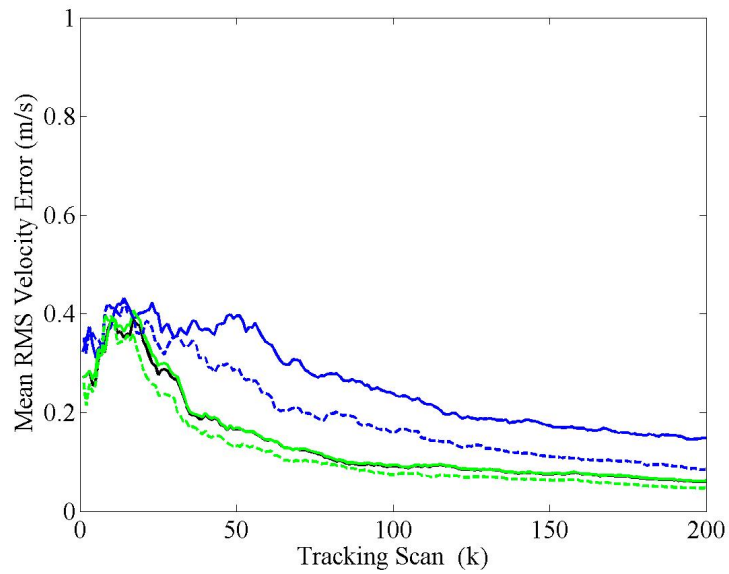
Figure 6.6: Mean RMS velocity error over 50 Monte Carlo simulations (NFA=10).

(a) Nearest Neighbor Data Association

(b) Probabilistic Data Association

Polar Coordinate EKF

Distributed Data Fusion wo/ Feedback

Distributed Data Fusion w/ Feedback

Polar Coordinate EKF + Camera

Distributed Data Fusion w/ Feedback + Camera
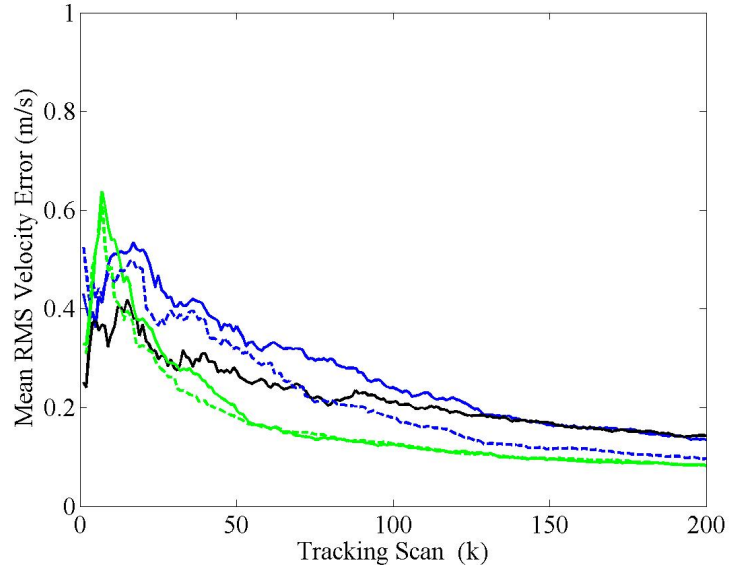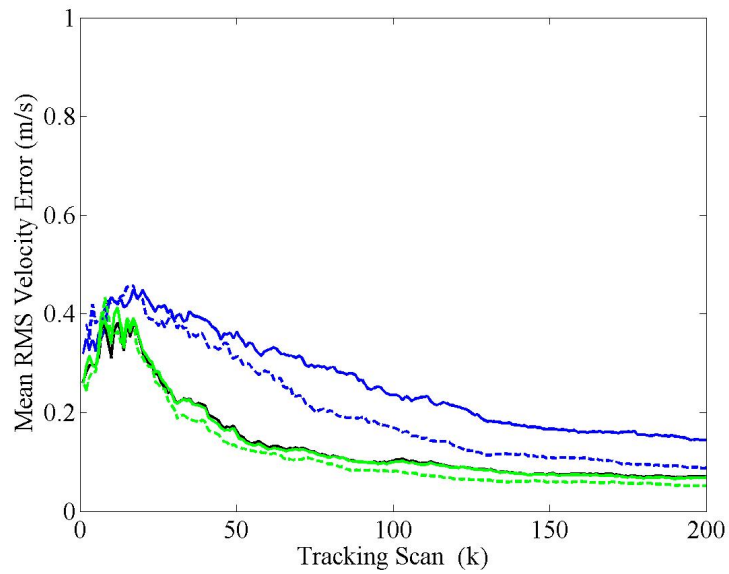
Figure 6.7: Mean RMS velocity error over 50 Monte Carlo simulations (NFA=20).

(a) Nearest Neighbor Data Association

(b) Probabilistic Data Association

Polar Coordinate EKF ▬▬▬ **Polar Coordinate EKF + Camera** ▬ ▬ ▬

Distributed Data Fusion wo/ Feedback ▬▬▬ **Distributed Data Fusion w/ Feedback + Camera** ▬ ▬ ▬

Distributed Data Fusion w/ Feedback ▬▬▬

Figure 6.8: Mean RMS velocity error over 50 Monte Carlo simulations (NFA=40).

6.1.3 Normalized Error And Consistency Test

Normalized error can be used to determine how well the covariance estimates model the true distribution of the state estimates. For a given estimate $\hat{x}_k^n$ at time k of simulation run n, the normalized error is defined as (6.1).

$$d^2(\hat{x}_k^n) = [x_k^n - \hat{x}_k^n]^T (P_k^n)^{-1} [x_k^n - \hat{x}_k^n] \tag{6.1}$$

where x_k^n is the ground truth for that time step and simulation run. If the covariance of this measure is matched properly it should have a chi-squared distribution with n_x degrees of freedom, where n_x is the number of elements in the state vector. Because of this distribution, the normalized error, if representing a chi-squared random variable, should fall between the chi squared bounds which can be found in a chi squared lookup table. Since a single run cannot provide an accurate depiction of the performance, multiple Monte-Carlo runs are performed and their results are averaged over those runs at a given time step to get a better picture of the performance (6.2).

$$\hat{d}^2(\hat{x}_k) = \frac{\sum_{n=1}^{N_{MC}} d^2(\hat{x}_k^n)}{N_{MC}} \tag{6.2}$$

Since the mean normalized error is being taken, if the normalized error of for each run is chi-squared distributed, and they are being summed over N_{MC} Monte-Carlo runs, the result should be chi-squared distributed with $n_x \times N_{MC}$ degrees of freedom. With this knowledge and a desired confidence bound, the bounds the sum of those normalized values over the simulation can be found using a chi - squared table. The bound can also be scaled based on whether or not the normalized distances are just summed or the mean was taken. If the sum (or mean) at a given scan across the various simulations is outside of those bounds then there is a good possibility that the state covariance estimate is artificially high or low, which means the covariance updates are not accurate. Unfortunately, this process requires some ground truth, so it is traditionally used in validating models in simulations.

Looking at the simulated data, the the systems using the PDA approach almost always fell within the consistency bounds (with 95% confidence) regardless of the density of false alarms. This means that for these systems using PDA, the covariance estimates did a good job of estimating the true state estimate error distribution. As for the nearest neighbor approach, with only the possibility of ten false alarms, the distributed with and without feedback systems quickly moved well outside the bounds. Because these values were way above the upper bound, the covariance estimates were artificially smaller than the true covariance of the state estimate error. The standard polar coordinate framework with and without the camera measurements, however, remained partially consistant as the number of possible false alarms increased, with the least consistant results occuring with the greatest number of possible false alarms.

(a) Nearest Neighbor Data Association

(b) Probabilistic Data Association

Polar Coordinate EKF ────── **Polar Coordinate EKF + Camera** ─ ─ ─

Distributed Data Fusion wo/ Feedback ────── **Distributed Data Fusion w/ Feedback + Camera** ─ ─ ─
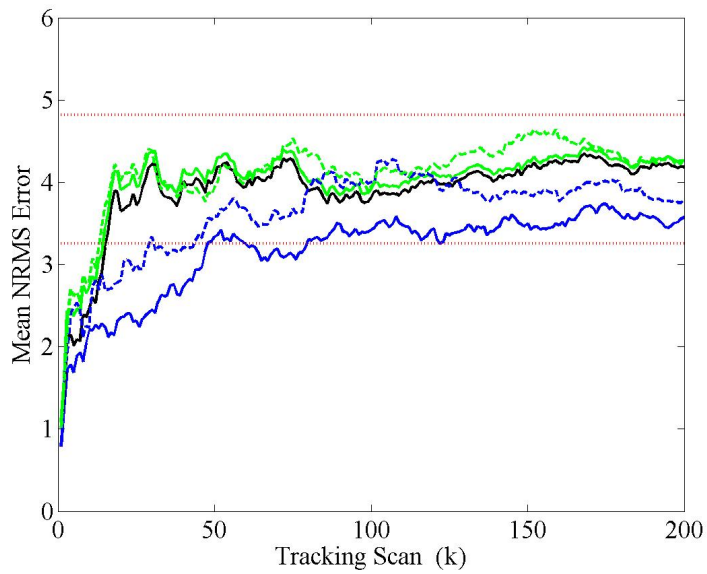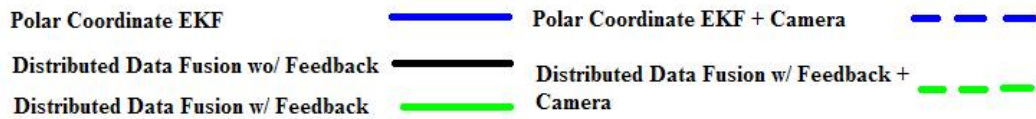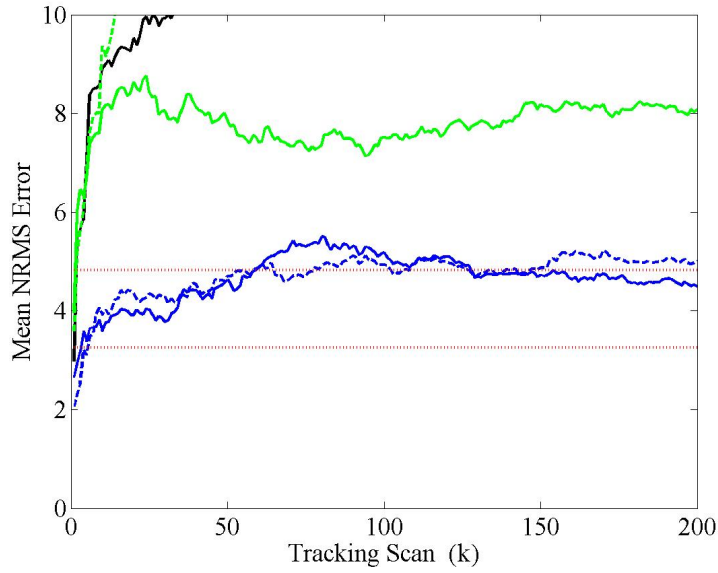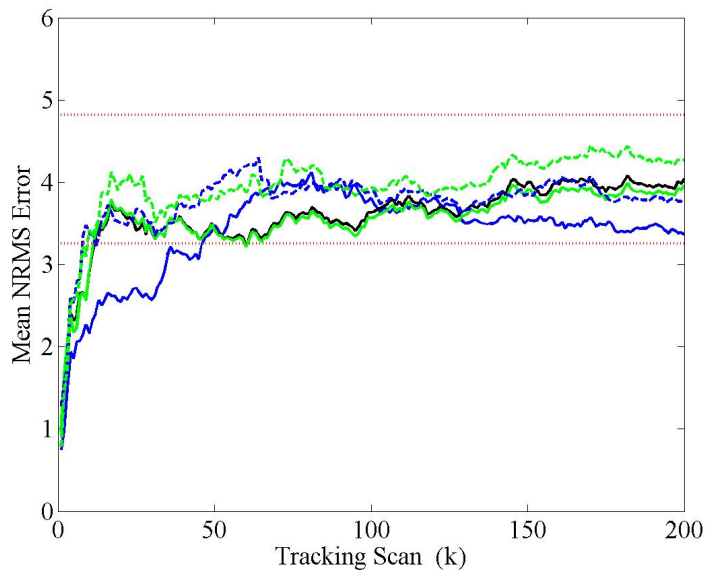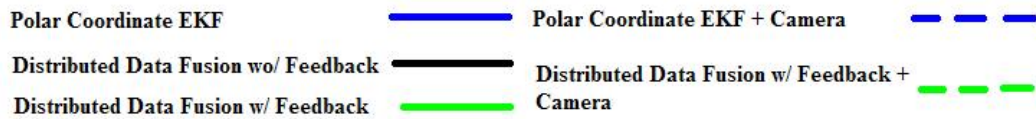
Distributed Data Fusion w/ Feedback ──────
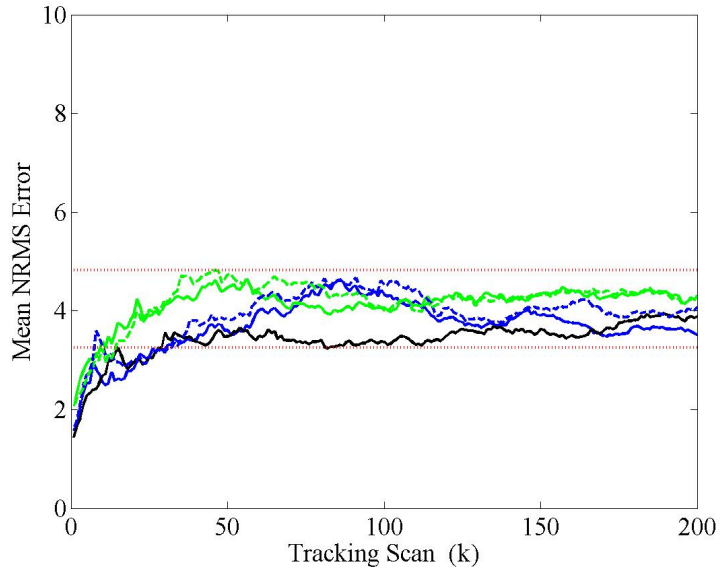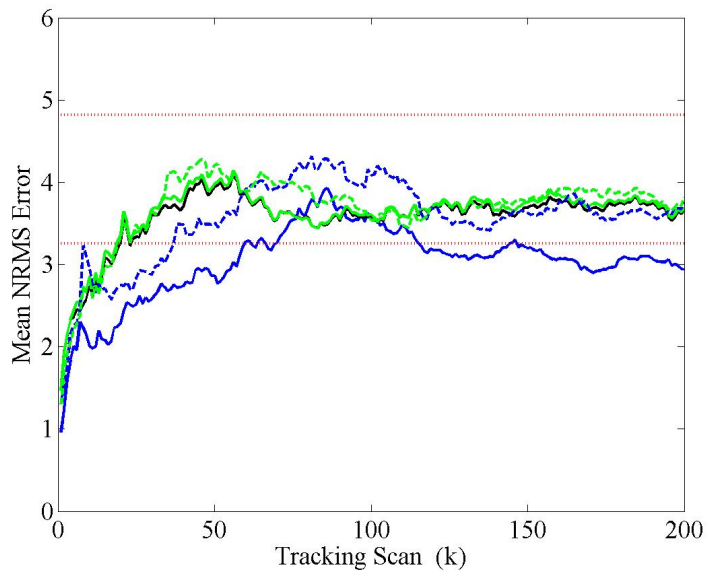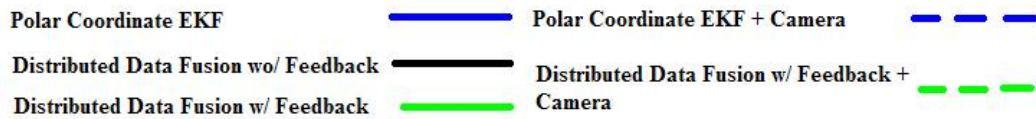
Figure 6.9: Mean NRMS error over 50 Monte Carlo simulations (NFA=0).

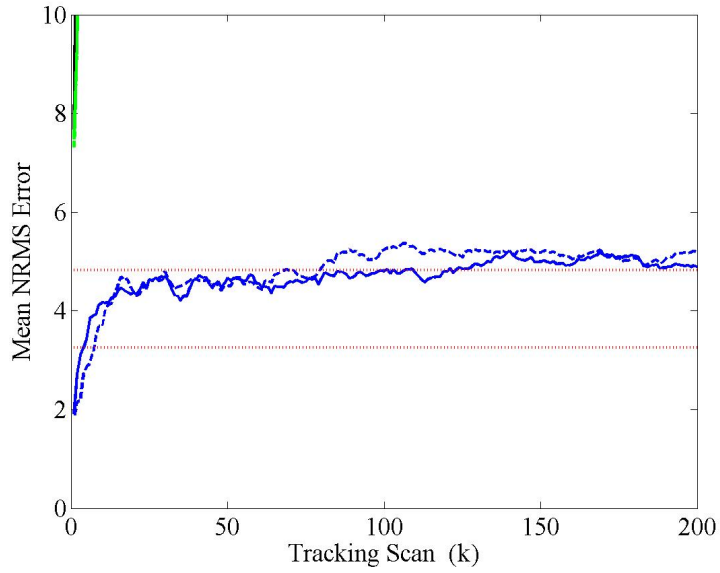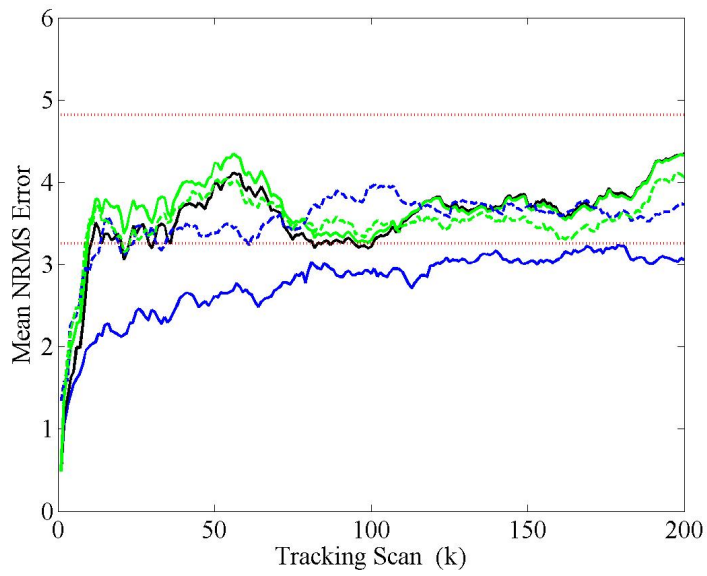(a) Nearest Neighbor Data Association

(b) Probabilistic Data Association

Polar Coordinate EKF ——— Polar Coordinate EKF + Camera – – –

Distributed Data Fusion wo/ Feedback ——— Distributed Data Fusion w/ Feedback + Camera – – –

Distributed Data Fusion w/ Feedback ———
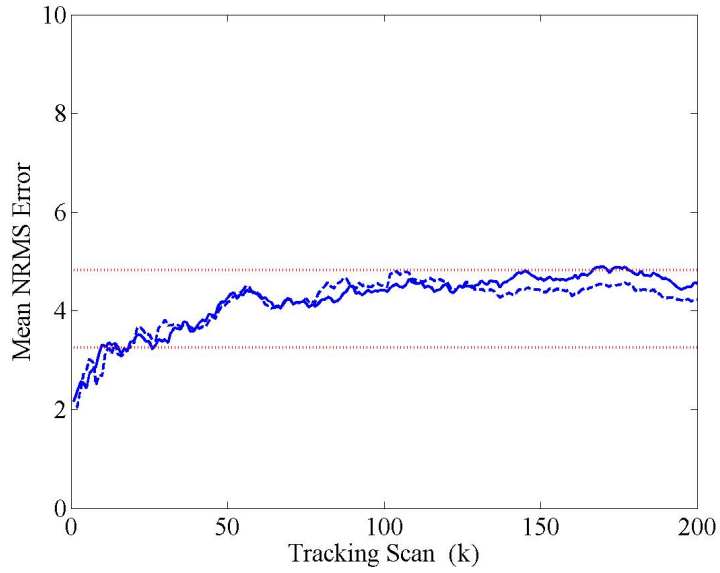
Figure 6.10: Mean NRMS error over 50 Monte Carlo simulations (NFA=10).

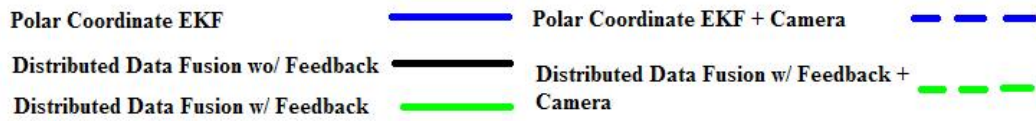(a) Nearest Neighbor Data Association

(b) Probabilistic Data Association

Polar Coordinate EKF

Distributed Data Fusion wo/ Feedback

Distributed Data Fusion w/ Feedback

Polar Coordinate EKF + Camera

Distributed Data Fusion w/ Feedback + Camera

Figure 6.11: Mean NRMS error over 50 Monte Carlo simulations (NFA=20).

(a) Nearest Neighbor Data Association

(b) Probabilistic Data Association

Polar Coordinate EKF ————
Polar Coordinate EKF + Camera ─ ─ ─

Distributed Data Fusion wo/ Feedback ————
Distributed Data Fusion w/ Feedback + Camera ─ ─ ─

Distributed Data Fusion w/ Feedback ————

Figure 6.12: Mean NRMS error over 50 Monte Carlo simulations (NFA=40).

6.2 Experimental Results

To test the effectiveness of the the system, a prototype was developed to collect data. The data consists of a a set of five vehicles traveling down a three lane highway. The first target is isolated while the remaining four have periods of overlap which represents a multi target scenario. The spectrograms and the resulting detections from the a CACFAR detector can be be seen for the Doppler, Up-Chirp, and Down-Chirp regions in Figures 6.13-6.15 respectively.

Track initialization is performed manually. Starting points for each target (i) are chosen from the three waveform spectrograms, which provided three frequency measures and three angles, one set from each waveform. An initial range was extracted by using the up-chirp and down-chirp frequency measures (6.3), while the mean of the angle measurements were taken to form an angle (6.4).

$$r_o(i) = \frac{c_o T}{4\beta}(f_o^{Rise}(i) + f_o^{Fall}(i)) \qquad T = T^{Rise} = T^{Fall} \tag{6.3}$$

$$\theta_o(i) = \frac{\theta_o^{Dopp}(i) + \theta_o^{Rise}(i) + \theta_o^{Fall}(i)}{3} \tag{6.4}$$

Although the Doppler region frequency and the combined angle can be used directly to form an estimate of the speed, due to the possibility of error in angle and the effect of the speed projection onto the range as the vehicles enter the scene, it is easier to initialize the velocity using the posted road speed limit, s_P (in this case 65 mph or 29 m/s) and the road angle from the road model, (α). Using the range, angle, speed, and direction information and a polar to Cartesian conversion an initial vehicle state and state covariance are formed in the Cartesian space to seed the tracking systems (6.5-6.6).

$$\hat{x}_{0|0}(i) = \begin{bmatrix} r_o(i)sin(\theta_o(i)) \\ s_P sin(\alpha) \\ r_o(i)cos(\theta_o(i)) \\ s_P cos(\alpha) \end{bmatrix} \tag{6.5}$$

$$P_{0|0}(i) = \begin{bmatrix} 25 & 0 & 00 & 0 \\ 00 & 1 & 00 & 0 \\ 00 & 0 & 25 & 0 \\ 00 & 0 & 00 & 1 \end{bmatrix} \tag{6.6}$$

The ending points are also chosen to let the tracking system know when the process is complete. In the following subsections, the cross-track error, speed errors, and angle errors are discussed for the tracking structures derived in this document.
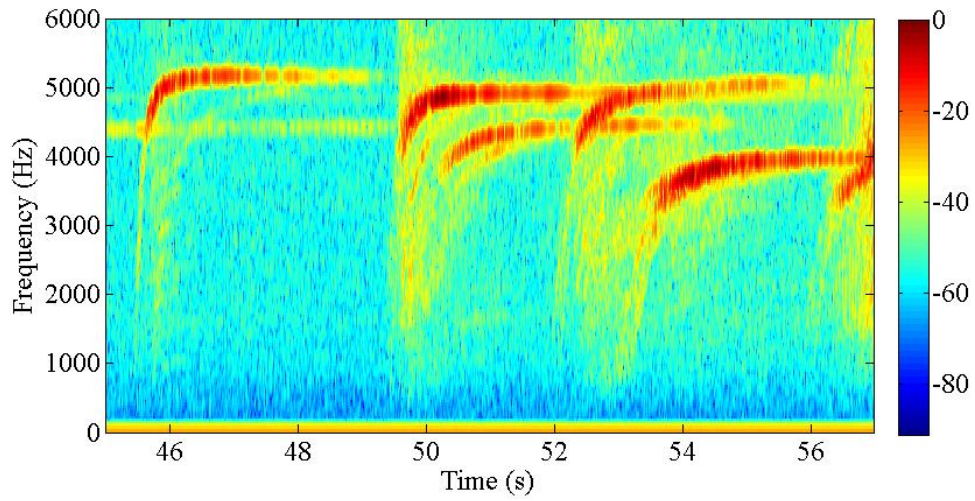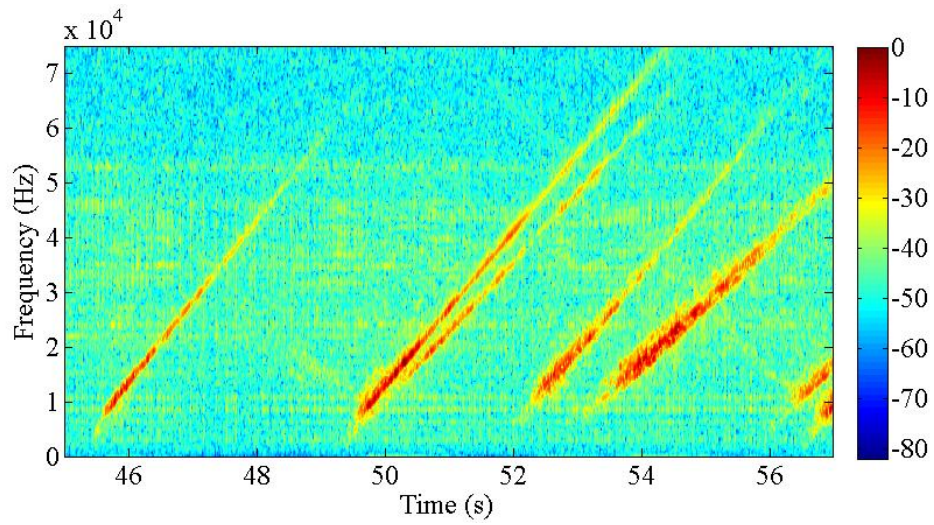
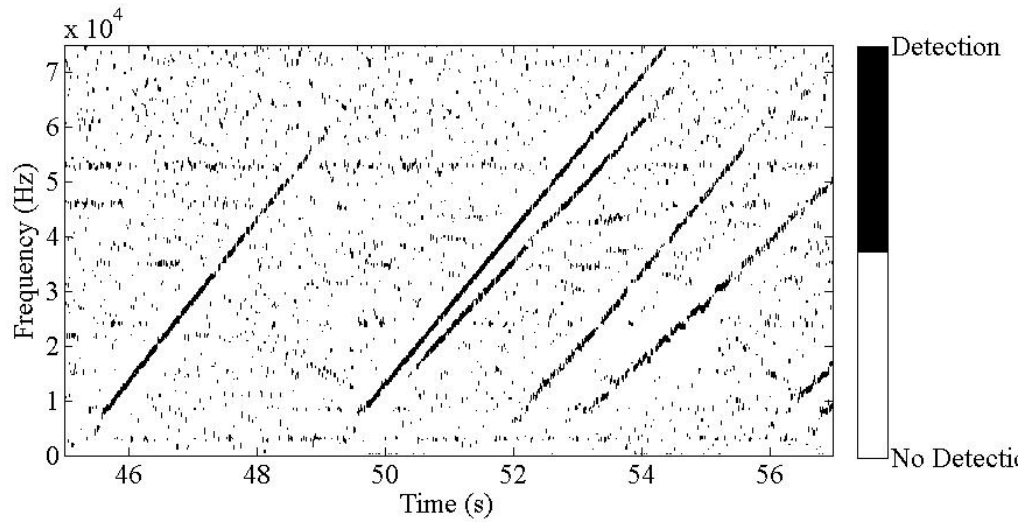(a) Doppler Magnitude Spectrogram (dB)
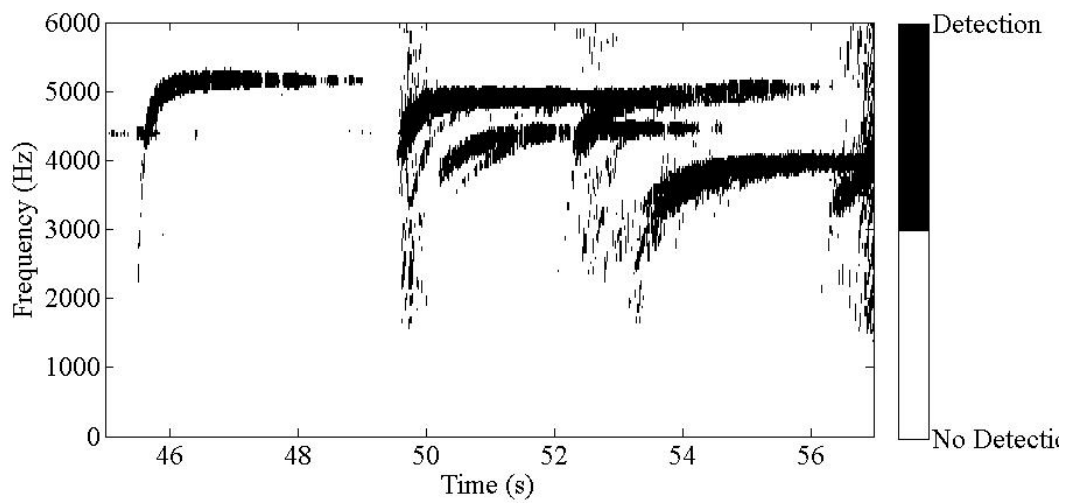
(b) Doppler Detections

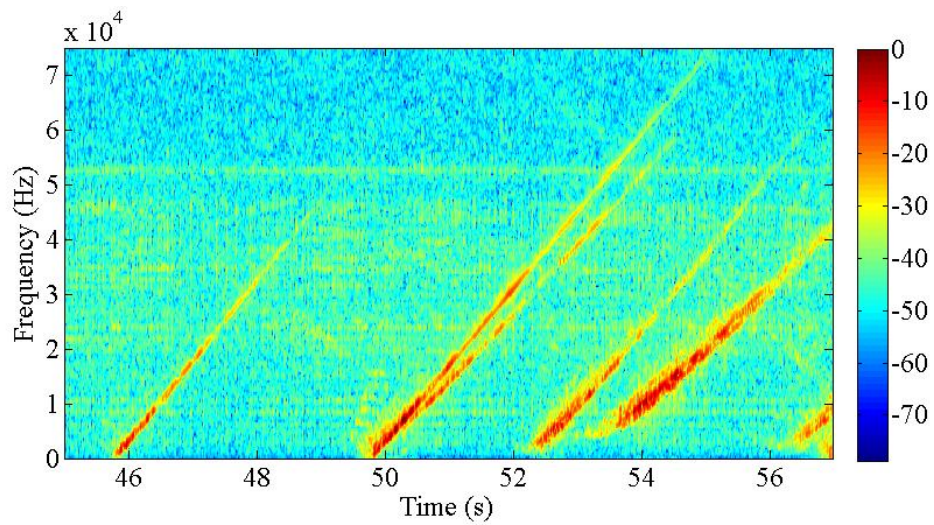Figure 6.13: Frequency domain data and detections for Doppler region.
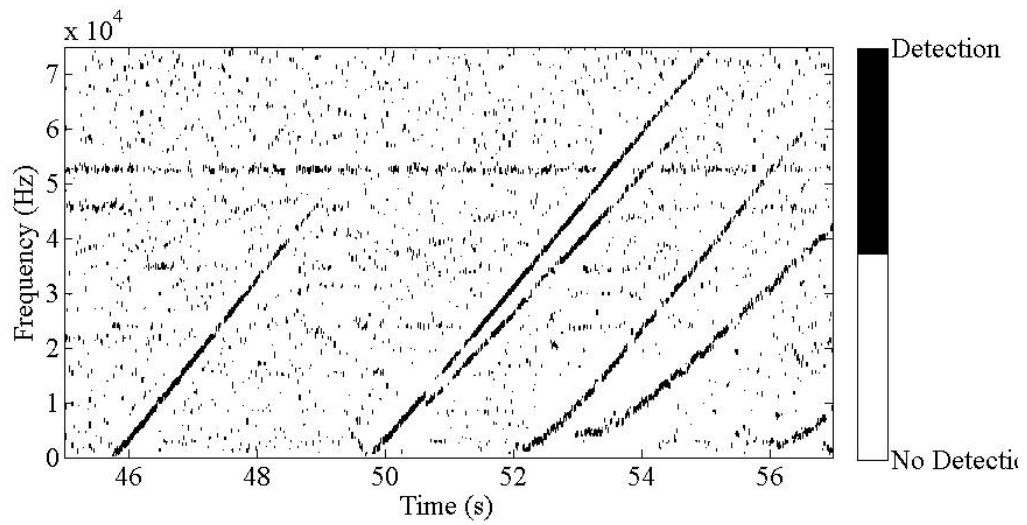
(a) Up-Chirp Magnitude Spectrogram (dB)

(b) Up-Chirp Detections

Figure 6.14: Frequency domain data and detections for up-chirp region.

(a) Down-Chirp Magnitude Spectrogram (dB)

(b) Down Chirp Detections

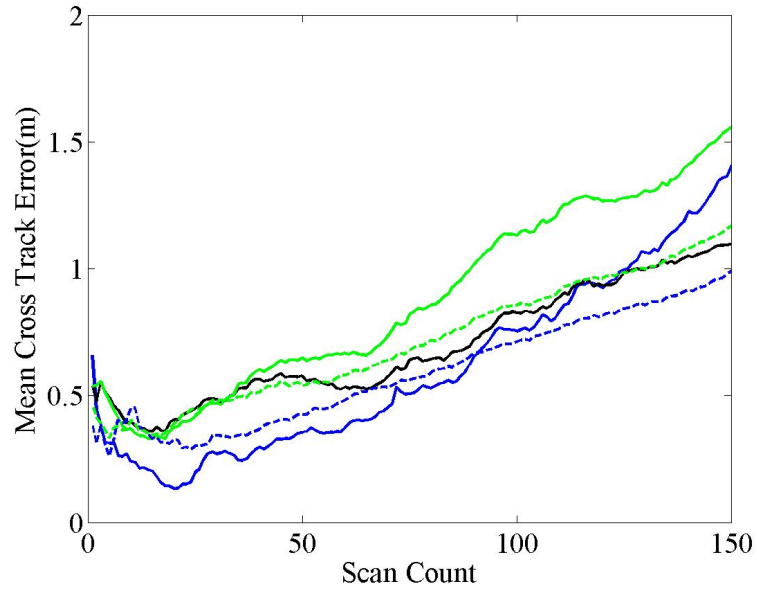Figure 6.15: Frequency domain data and detections for down-chirp region.

6.2.1 Cross Track Errors

Since ground truth data on position is hard to achieve for highway vehicles due to a lack of accurate reliable sensors and timing issues, the cross track error from the road model (the perpendicular distance the position estimate deviates from the road lane model) of the state estimates are measured as a metric. Although this is not an ideal metric, it will be able to determine if there is a significant deviation from the road model which could signify a possible problem in the system. The cross track error is measured for all targets versus their manually (correctly) assigned lanes for each of the tracking frameworks. The cross track errors are also measured for the systems with respect to the data association approach. The mean of these cross track errors can be seen in Figure 6.16 with 6.16a providing the mean cross track errors using the nearest neighbor approach and 6.16b providing the results from the probabilistic data association approach.
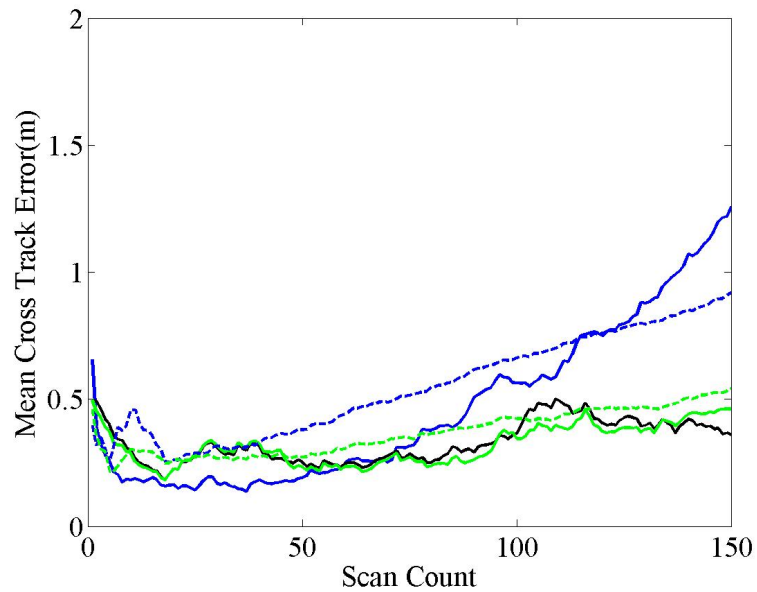
In these results, the first thing than can be seen is that over the 150 update tracking period (approximately three seconds), the cross track error does not exceed two meters which is about half of a lane width on a standard highway although in the case of the nearest neighbor data association the cross track error is increasing suggesting that the system is diverging. As the experimental results have shown, this observation represents the standard problem for the nearest neighbor association process in the presence of even modest amounts of false detections. It is important to see though that the rate of divergence is smaller for those systems where camera measurements were added with respect to the nearest neighbor association.

For the probabilistic data association method, both the radar only distributed fusion trackers and the distributed fusion with feedback and camera measurement tracker had comparable mean cross track errors which seemed to stay fairly consistent and does not seem to be diverging. There does not seem to be a significant improvement in the cross track error by adding the camera measurements to the distributed with feedback radar model. The polar measurement based trackers do seem to be diverging, but like the results seen in the

nearest neighbor association approach, the camera measurements seem to slow the rate of divergence.

(a) Nearest Neighbor Data Association
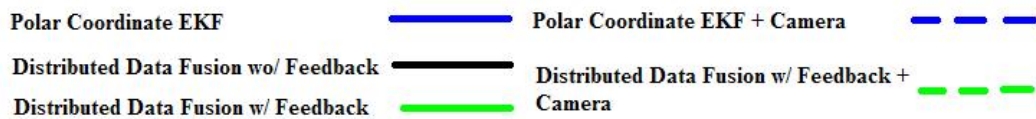

(b) Probabilistic Data Association

Polar Coordinate EKF ———————   Polar Coordinate EKF + Camera — — —

Distributed Data Fusion wo/ Feedback ———————   Distributed Data Fusion w/ Feedback + Camera — — —

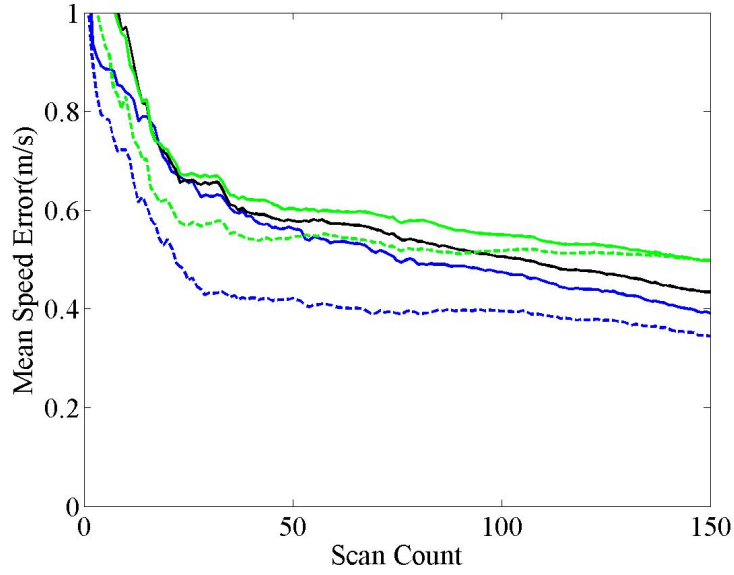Distributed Data Fusion w/ Feedback ———————

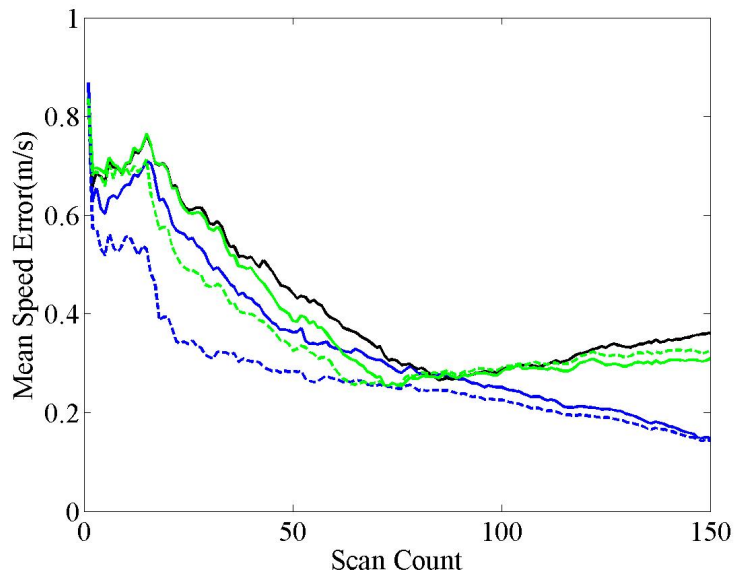Figure 6.16: Mean cross track error for experimental data.

6.2.2 Speed Errors

The mean speed errors are also measured with respect to the actual measured speeds for the five vehicles. The measured speed was a single snapshot of the speed with the equivalent of a K-band speed radar gun used by the police so it does not account for any accelerations that may have been experienced by the vehicles while in motion. A visual inspection of the Doppler data from Figure 6.13 provides some confidence that there is little acceleration in the vehicles which can be seen by the flat response as time progresses in the pure Doppler returns. Like the cross track errors, each tracking structure was used on each target with the two data association strategies. The mean error from the measured speed for this data set can be seen in Figure 6.17.

Two major trends can be seen in the speed error plots. The first is that speed error seems to be converging rather than diverging and the camera measurements do seem to provide a significant improvement in the convergence rate and in most cases provide a reduction in the speed error. For any given tracking method, the mean speed error using the PDA approach is smaller than that of its nearest neighbor counterpart which was one of the observations from the experimental data. Finally, for a given data association approach, the trackers not using camera measurements all had similar mean speed error with small variations as the tracking process progressed.

(a) Nearest Neighbor Data Association

(b) Probabilistic Data Association
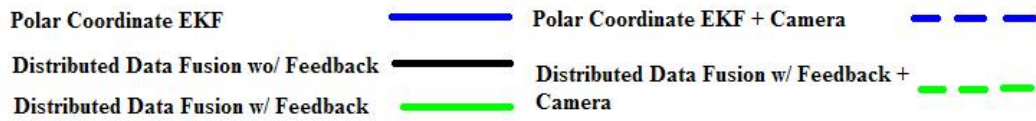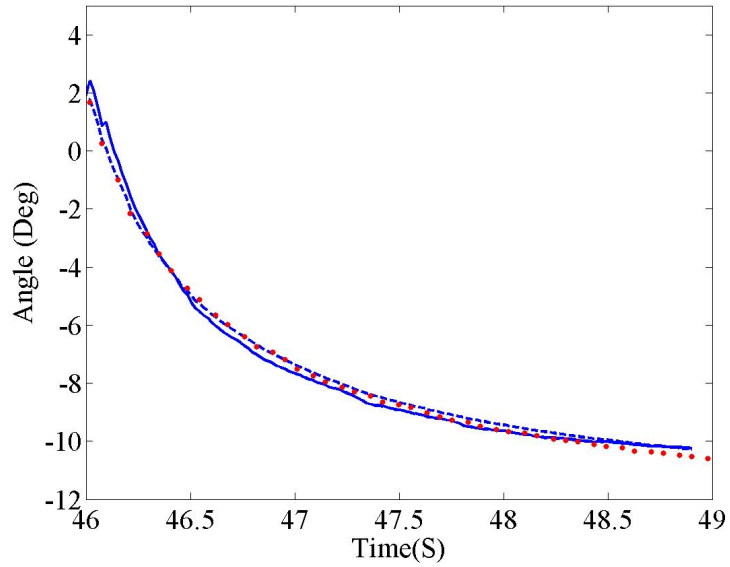
Polar Coordinate EKF   Polar Coordinate EKF + Camera

Distributed Data Fusion wo/ Feedback   Distributed Data Fusion w/ Feedback + Camera

Distributed Data Fusion w/ Feedback

Figure 6.17: Mean speed error for experimental data.

6.2.3 Angle Information

One of the keys to an effective traffic surveillance system is the ability to correctly associate the state updates from the tracker to the actual physical entity in the video stream for visual identification. Based on the tracking scenario, only one vehicle can occupy a given angle on the image plane (not counting occlusions), but there could be another vehicle close in angle. This fact is especially true as vehicles travel away from the sensor in a down the road type application. With these facts in mind, a comparison of the projected angle results from the state update to ground truth is shown for the systems with and without the camera measurements. Ground truth in this case is generated by manually choosing the target centers from the video stream for every frame and each vehicle within the tracking period. Figure 6.18 provides the results for the standard polar measurement approach with and without the camera measurements added and using the two data association methods. Figure 6.19 shows the results for the distributed data fusion with feedback with and without the camera measurements for both data association methods. For the sake of visual appeal, the angles from a single target are shown in these figures, but the results were similar for all targets in this scenario.

Scenarios where the camera measurements were used in all cases have projected angles that more closely match the ground truth over the methods that do not use the camera measurements. This result is an intuitive since the camera is measuring angle, one would hope that in the tracking framework it would improve the angle information embedded into the state estimate. In these scenarios, the projected angles for the systems can deviate from those systems that utilize the camera measurements by as much as a half a degree. In many cases, this level of error would be sufficient enough to make an association on a video stream without the need for the video based measurements into the system.

(a) Nearest Neighbor Data Association

(b) Probabilistic Data Association

Polar Coordinate EKF ————   Polar Coordinate EKF + Camera – – –
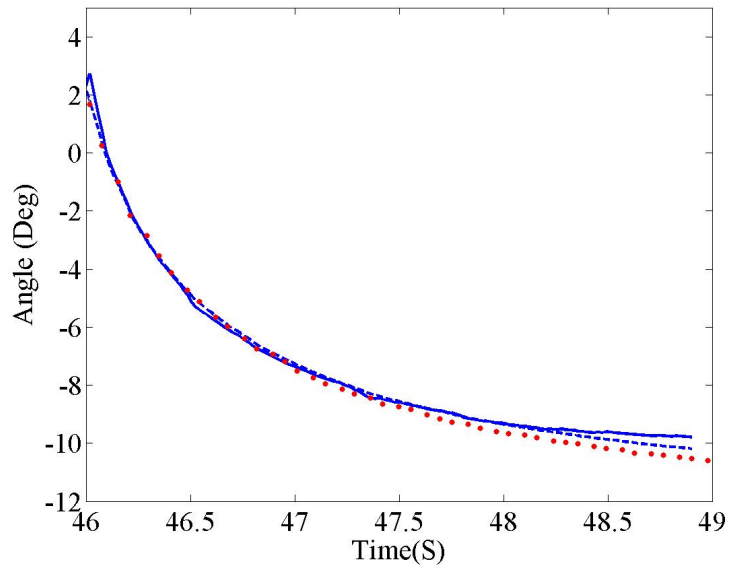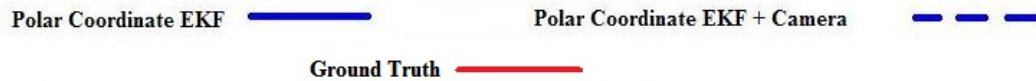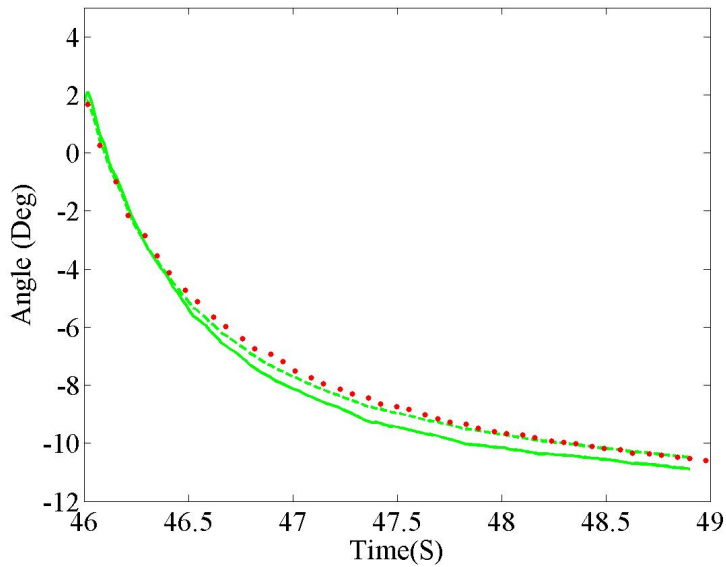
Ground Truth ————

Figure 6.18: Projected angle vs. ground truth comparison for polar measurements with and without camera measurement fusion.

(a) Nearest Neighbor Data Association

(b) Probabilistic Data Association

Distributed Data Fusion w/ Feedback

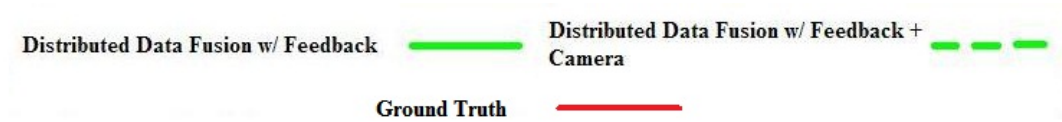Distributed Data Fusion w/ Feedback + Camera
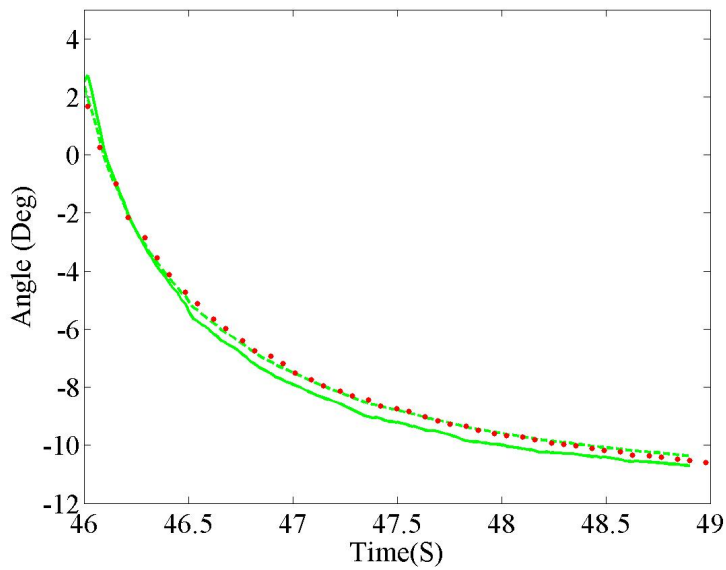
Ground Truth

Figure 6.19: Projected angle vs. ground truth comparison for distributed fusion with feedback models with and without camera measurement fusion.

A couple sample frames from the video sequence are also displayed with the angle overlaid onto the images for the systems with and without the camera measurement. These can be seen in Figures 6.20-6.23. One frame has results from a single target case while the other has the results from a two target section of the data. Images are magnified to enhance the region where the target is present and to give a better visual queue to the angle estimate performance.

In most of these scenarios, The addition of the camera measurements into the system provided an angle measure that was closer to that of the ground truth angle measure. This result is expected since these systems have an additional pure angle measurement added into the estimation process. For the systems using both polar measurements and camera information, there seems to be little difference between those systems which used nearest neighbor association versus those systems that used probabilistic data association. However, there is a small improvement in some cases for systems only using polar radar measurements when probabilistic data association is used over the nearest neighbor approach. In systems using the distributed fusion with camera measurements, in almost all cases, the angle measure was closer to ground truth over the systems using polar measurements. These systems where the distributed fusion model was used, the probabilistic data association approach provided an angle measure closer to that of the ground truth.

An additional observation can be made from these plots. All of the angle measures in these examples fell within the body of the vehicle being tracked. This observation provides some confidence that the system is working well. This result also shows the the system can provide a decent ability to discriminate targets in the video for identification purposes.

(a) Nearest Neighbor
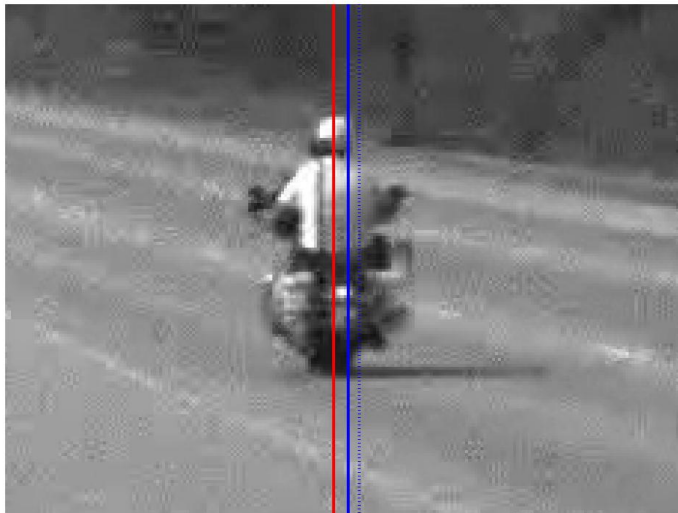
(b) Probabilistic Data Association

Polar Coordinate EKF ————   Polar Coordinate EKF + Camera — — —

Ground Truth ————

Figure 6.20: Portion of a sample frame with one target and angle overlaid for polar measurement tracker with and without camera measurement fusion.

(a) Nearest Neighbor

(b) Probabilistic Data Association

| Polar Coordinate EKF | ▬▬▬ | Polar Coordinate EKF + Camera | ▬ ▬ ▬ |
| Ground Truth | ▬▬▬ | | |

Figure 6.21: Portion of a sample frame with two targets and angle overlaid for polar measurement tracker with and without camera measurement fusion.

(a) Nearest Neighbor

(b) Probabilistic Data Association

| Distributed Data Fusion w/ Feedback | ———— | Distributed Data Fusion w/ Feedback + Camera | — — — |
| Ground Truth | ———— | | |
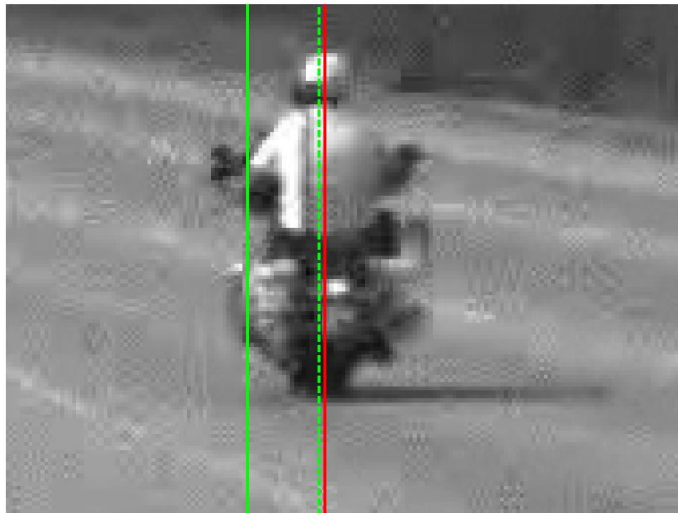
Figure 6.22: Portion of a sample frame with one target and angle overlaid for distributed data fusion tracker with and without camera measurement fusion.

(a) Nearest Neighbor

(b) Probabilistic Data Association

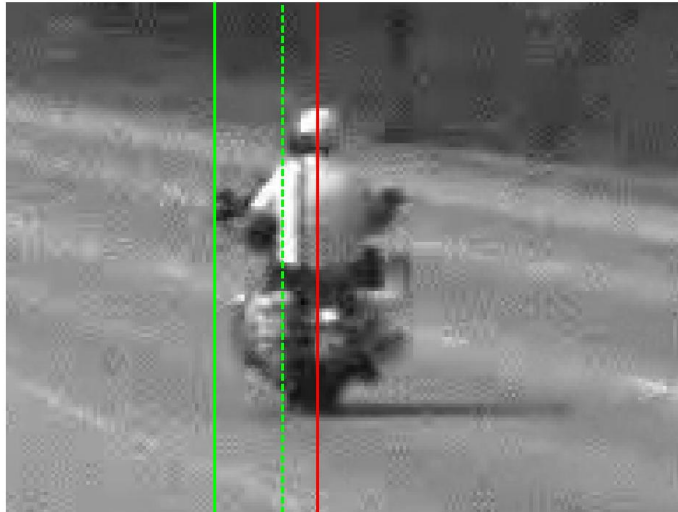Distributed Data Fusion w/ Feedback ———   Distributed Data Fusion w/ Feedback + Camera – – –
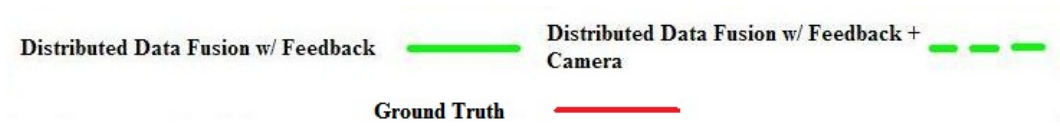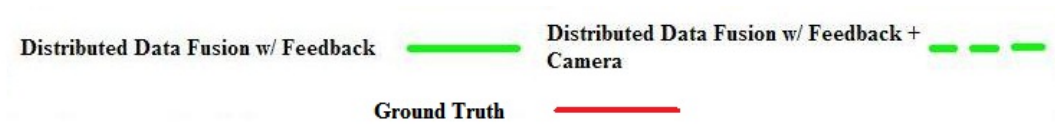
Ground Truth ———

Figure 6.23: Portion of a sample frame with two targets and angle overlaid for distributed data fusion tracker with and without camera measurement fusion.

Chapter 7

Conclusion

7.1　Summary

For this research, the limitations of traditional multi-waveform frequency modulated continuous wave (FMCW) radar were discussed and two methods were developed to address them. The first method improves on the traditional waveform segment matching and measurement formation approach by providing a weighing function to group measurements from the waveform segments effectively. The second method treats the multi-waveform radar as a distributed multi-sensor fusion problem where each waveform section is treated as an individual sensor, which is providing state estimates independently and the results fused. Distributed fusion with and without global feedback were explored.

　　Once the multi-waveform FMCW radar system models were developed, a fusion scheme was developed hat combines the state estimates from the radar trackers with measurements from a video sensor for additional angular information and identification purposes. Through the use of distributed data fusion, these camera measurements were added as an additional sensor into the original sensor models.

　　The polar measurement generation scheme was validated through a multiple run simulation model and an application for using these polar measurements to generate a road

model for initial state estimation were discussed. Simulations provided confidence in the polar measurement generation scheme, as well as, its robustness against false detections. In cases where the probability of false alarms is greatest and target speeds are close, the matching method provided in this research provides a ten to twenty percent increase in the probability of correct association over the traditional approaches.

Results from simulations and a real world scenario show that with proper data association techniques, many of these radar-only and radar-camera tracking systems provide accurate state information on targets of interest. These results in general showed that the probabilistic data association method provides a more consistent, and in many cases, a less erroneous state estimate in the presence of many false detections. Most scenarios provide a two to three times decrease in the steady state RMS errors in both position and velocity. In general, addition of camera measurements also improves system performance with around a twenty to thirty percent decrease in the steady state RMS errors when compared to the radar-only counterparts. Additionally, the camera measurements improve the discrimination ability on the video sequence for proper identification.

7.2   Contributions

This research provides the following contributions:

- A weighted matching algorithm was developed to associate the frequency and angle measurements from the sections of a three part waveform in order to generate traditional polar coordinate measurements.

- Two multi-sensor fusion approaches were developed to model a single sensor with multiple waveforms as a distributed sensor network (with and without global feedback).

- A distributed fusion strategy was developed to fuse a traditional polar coordinate

110

measurement based extended Kalman filter with video camera measurements.

- A distributed fusion strategy was also developed to fuse the distributed sensor fusion model for multi-waveform FMCW radar filtering with video camera measurements.

- A road modeling algorithm using the Hough transform on the polar coordinate radar data is introduced.

- An in depth comparison of the performance of the developed systems using nearest neighbor association and probabilistic data association for tracking in clutter was provided through the use of simulations and a real world example.

7.3   Future Research

There are several paths for additional research. Some significant effort can be directed towards automated track initialization, track scoring, and track deletion in order to automatically start and stop the tracking process. This track maintenance addition is essential to automating a tracking system. Another route for additional research is in reliable vehicle tracking in scenarios where there is inter-vehicle occlusion during part of the tracking period. During periods of dense traffic there is a high probability that vehicles will occlude one another during the tracking process.

Additionally, some work can be directed towards better detection strategies in the radar data. Although the CFAR detectors do a good job of detection in the data, they also suffer from a fair number of false detections. The detection scheme could relax the point target model, which in turn, could improve the robustness of the detection scheme while reducing the number of false alarms. Modifying the centroid measurement model for vehicles in the image plane might also be able to provide a better estimate, since the strongest reflector on the vehicle for the radar might not correspond to the centroid of the car model on the video.

The scenario explored by this document was the case of multi-lane traffic all traveling

in the same direction with light traffic flow. Because of these assumptions, the nearest neighbor and probabilistic data association approaches were able to be used directly without regard to overlap in measurements. In most cases, there are no crossings in the up-chirp and down-chirp spectrograms, and by the time the Doppler measurements cross, the measurement gating threshold prevents the tracks from associating with measurements from other tracks. In a scenario with higher traffic flow or multi-directional traffic flow, this situation may not be the case. In order to compensate for this fact, the use of a global nearest neighbor or joint probabilistic data association might be explored to compensate for the possible measurement interaction.

Bibliography

[1] Chong, C.-Y., Garren, D., and Grayson, T. P., 2000. "Ground target tracking: A histrocial prespective". In 2000 IEEE Aerospace Conference Proceedings, Vol. 3, pp. 433 – 448.

[2] Fisher, P. D., 1992. "Improving on police radar". *IEEE Spectrum,* **29**(7), pp. 38–43.

[3] Floudas, N., Polychronopoulos, A., and Amditis, A., 2005. "A survey of filtering techniques for vehicle tracking by radar equipped automotive platforms". In The 7th International Conference on Information Fusion, pp. 1436–1443.

[4] Gunnarsson, J., Svensson, L., Danielsson, L., and Bengtsson, F., 2007. "Tracking vehicles using radar detections". In 2007 IEEE Intelligent Vehicles Symposium, pp. 296–302.

[5] Lee, M. S., and Kim, Y. H., 2001. "New data association method for automotive radar tracking". *IEEE Proceedings on Radar, Sonar, and Navigation,* **148**, pp. 297 – 301.

[6] Zuther, S., Biggel, M., Muntzinger, M. M., and Dietmayer, K., 2009. "Multi-target tracking for merged measurements of automotive narrow-band radar sensors". In Proceedings of the 12 International IEEE Conference on Intelligent Transportation Systems, pp. 455 – 460.

[7] Kastrinaki, V., Zervakis, M., and Kalaitzakis, K., 2003. "A survey of video processing techniques for traffic applications". *Image and Vision Computing*(21), pp. 359–381.

[8] Buch, N., Velastin, S. A., and Orwell, J., 2011. "A review of computer vision techniques for the analysis of urban traffic". *IEEE Transactions on Intelligent Transportation Systems*, pp. 1 –20.

[9] Gern, A., Franke, U., and Levi, P., 2001. "Robust vehicle tracking fusing radar and vision". In 2001 IEEE Conference on Mutisensor Fusion and Integration for Intelligent Systems.

[10] Steux, B., Laurgeau, C., Salesse, L., and Wautier, D., 2002. "Fade: A vehicle detection and tracking system featuring monocular vision and radar data fusion". In IEEE Intelligent Vehicles Symposium, pp. 632–639.

[11] Kawasaki, N., and Kiencke, U., 2004. "Standard platform for sensor fusion on advanced driver assistance system using bayesian network". In IEEE Intelligent Vehicles Symposium, pp. 250–255.

[12] Sole, A., Mano, O., Stein, G., Lumon, H., Tamatsu, Y., and Shashua, A., 2004. "Fusion of doppler radar and video information for automatic traffic surveillance". In IEEE Intelligent Vehicles Symposium, pp. 819–824.

[13] Roy, A., Gale, N., and Hong, L., 2009. "Fusion of doppler radar and video information for automatic traffic surveillance". In 2009 International Conference On Information Fusion, pp. 1989 – 1996.

[14] Roy, A., Gale, N., and Hong, L., 2011. "Automated traffic surveillance using fusion of doppler radar and video information". *Mathematical and Computer Modeling,* **54**, pp. 531–543.

[15] Wu, S., Decker, S., Chang, P., Camus, T., and Eledath, J., 2009. "Collision sensing by stereo vision and radar sensor fusion". *IEEE Transactions on Intelligent Transportation Systems,* **10**, pp. 606 – 614.

[16] Jankiraman, M., 2007. *Design of multi-frequency CW radars*. SciTech Pub.

[17] Pace, P., 2009. *Detecting and classifying low probability of intercept radar*, 2nd ed. Artech House Radar Library. Artech House, Boston, Massachusetts.

[18] Skolnik, M., 2001. *Introduction to radar systems*, 3 ed. McGraw-Hill.

[19] Mahafza, B., and Elsherbeni, A., 2004. *MATLAB simulations for radar systems design*. CRC Press/Chapman & Hall, Boca Raton, Florida.

[20] Skolnik, M., 2007. *Radar handbook*, 3 ed. Electronics electrical engineering. McGraw-Hill.

[21] Mahafza, B., 2000. *Radar systems analysis and design using MATLAB*. Chapman & Hall/CRC.

[22] Chen, V., and Ling, H., 2002. *Time-frequency transforms for radar imaging and signal analysis*. Artech House radar library. Artech House.

[23] Minkler, G., and Minkler, J., 1990. *CFAR: the principles of automatic radar detection in clutter*. Magellan Book Co., Baltimore, Maryland.

[24] Forsythe, D., and Ponce, J., 2002. *Computer vision: a modern approach*. Prentice Hall, New Jersey.

[25] Hartley, R., and Zimmerman, A., 2004. *Multiple View Geometry in Computer Vision*, 2 ed. Cambridge University Press, Cambridge, UK.

[26] Ma, Y., Soatto, S., Kosecka, J., and Sastry, A. A., 2005. *An invitation to 3D vision: from images to geometric models*. Springer, New York.

[27] Zhang, Z., 2000. "A flexible new technique for camera calibration". *IEEE Trans. Pattern Anal. Mach. Intell.,* **22**, November, pp. 1330–1334.

[28] Bradski, G., 2000. "The opencv library". *Dr. Dobb's Journal of Software Tools*.

[29] Yilmaz, A., Javed, O., and Shah, M., 2006. "Object tracking: A survey". *ACM Comput. Surv.,* **38**.

[30] Karaman, M., Goldmann, L., Yu, D., and Sikora, T., 2005. "Comparison of static background segmentation methods". In Proceedings of SPIE Visual Communications and Image Processing, Vol. 5960, pp. 2040–2051.

[31] Piccardi, M., 2004. "Background subtraction techniques: a review". In IEEE International Conference on Systems, Man and Cybernetics, Vol. 4, IEEE, pp. 3099–3104.

[32] Bradski, G., and Kaehler, A., 2008. *Learning OpenCV: Computer Vision with the OpenCV Library*. O'Reilly.

[33] Kalman, R. E., 1960. "A new approach to linear filtering and prediction problems". *Transactions of the ASME–Journal of Basic Engineering,* **82**(Series D), pp. 35–45.

[34] Blackman, S., and Popoli, R., 1999. *Design and analysis of modern tracking systems*. Artech House, Boston, Massachusetts.

[35] Blackman, S., 1986. *Multiple-target tracking with radar application*. Artech House, Norwood, Massachusetts.

[36] Bar-Shalom, Y., and Li, X., 1995. *Multitarget-multisensor tracking: principles and techniques, 1995*. Yaakov Bar-Shalom.

[37] Bar-Shalom, Y., and University of California, L. A. U. E., 1992. *Multitarget-multisensor tracking: applications and advances*. Artech House.

[38] Bar-Shalom, Y., and Fortmann, T., 1988. *Tracking and data association*. Academic Press.

[39] Grewal, M., and Andrews, A., 2008. *Kalman filtering: theory and practice using MATLAB*, 3rd ed. Wiley.

[40] Bar-Shalom, Y., Daum, F., and Haung, J., 2009. "The probabilistic data association filter". *IEEE Control Systems Magazine,* **29**(6), pp. 82–100.

[41] Klotz, M., and Rohling, H., 2001. "A 24 ghz short range radar network for automotive applications". In Radar, 2001 CIE International Conference on, Proceedings, pp. 115 –119.

[42] Folster, F., Rohling, H., and Lubbert, U., 2005. "An automotive radar network based on 77 ghz fmcw sensors". In Radar Conference, 2005 IEEE International, pp. 871 – 876.

[43] Rohling, H., and Moller, C., 2008. "Radar waveform for automotive radar systems and applications". In 2008 IEEE Radar Conference, pp. 1–4.

[44] Hyun, E., and Lee, J.-H., 2009. "A method for multi-target range and velocity detection in automotive fmcw radar". In Proceedings of the 12th International Conference on Intelligent Traffic Systems, Vol. 2, pp. 7–11.

[45] Liggins, M., Hall, D., and Llinas, J., 2008. *Handbook of multisensor data fusion: theory and practice*, 2nd ed. CRC Press.

[46] Hall, D., and McMullen, S., 2004. *Mathematical techniques in multisensor data fusion*, 2nd ed. Artech House.

[47] Hong, L., 1991. "Centralized and distributed multisensor integration with uncertainties in communication networks". *Aerospace and Electronic Systems, IEEE Transactions on,* **27**(2), pp. 370 –379.

[48] Hong, L., 1992. "Distributed filtering using set models". *Aerospace and Electronic Systems, IEEE Transactions on,* **28**(4), oct, pp. 1144 –1153.

[49] Duda, R. O., and Hart, P. E., 1972. "Use of the hough transformation to detect lines and curves in pictures". *Commun. ACM,* **15**, pp. 11–15.